Ab-initio Raman spectra of anharmonic and disordered systems

Anna Putrino

Max-Planck-Institut für Festkörperforschung

Stuttgart, 2000

Ab-initio Raman spectra anharmonic and disordered systems

Von der Fakultät Physik der Universität Stuttgart zur Erlangung
der Würde eines Doktors der Naturwissenschaften
(Dr. rer. nat.)
genehmigte Abhandlung

vorgelegt von
Anna Putrino
aus Monza (Italien)

Hauptberichter:	Prof. Dr. M. Parrinello
Mitberichter:	Prof. Dr. A. Muramatzu
Tag der Einreichung:	7 November 2000
Tag der mündlichen Prüfung:	15 Dezember 2000

Max-Planck-Institut für Festkörperforschung
Stuttgart, 2000

Contents

List of Figures

List of Tables

Chapter 1

Zusammenfassung

Über die letzten Jahrzehnte haben Raman Streuexperimente wertvolle Informationen über die Dynamik der Kerne und ihrer Wechselwirkungen mit dem elektronischen Zustand geliefert.
In der Tat stellen sie (zusammen mit infrarot (IR) optischen Experimenten) eines der wichtigsten experimentellen Instrumente der Festkörperforschung dar.
Viele Forschungsgruppen haben Zugang zu geeigneter experimenteller Ausstattung und die theoretische Interpretation der Daten bereitet ausserdem keine größeren Schwierigkeiten. Dies trifft insbesondere auf periodische Festkörper zu, in denen nur sehr wenige Moden aufgrund von Symmetrie optisch aktiv sind.

In ungeordneten System oder Systemen, die durch starke anharmonische Effekte gekennzeichnet sind, sind solcherlei theoretische Überlegungen nur bedingt anwendbar. Unordnung relaxiert die symmetrie bedingten Auswahlregeln und führt zu breiten, komplizierten Spektren mit schwieriger Interpretation. Dies ist einer der Gründe, weshalb IR und Raman Spektroskopie an ungeordneten Systemen bisher noch nicht die Bedeutung erlangt hat, die sie für geordnete Kristalle haben.

Viele Versuche, diese Situation zu verbessern, sind bereits unternommen worden.

Die meisten basieren auf molekulardynamischen Simulationsmethoden (beschrieben in Kapitel 3). Effektive Potentiale für die Beschreibung der Wechselwirkung zwischen Teilchen ermöglichen es, die Zeitentwicklung des Systems in adäquater Weise zu simulieren. Allerdings beruhen Eigenschaften wie IR und Raman Aktivität sowohl auf der Ionenstruktur als auch auf elektronischen Eigenschaften wie elektronischer Dipole und Polarisierbarkeit. Diese Eigenschaften sind nicht enthalten in den standard molekulardynamischen Modellen; zusätzliche Parametrisierung ist daher notwendig, um IR und Raman Aktivität zu beschreiben. Entsprechend kommt zu der Unsicherheit bei der Beschreibung der interatomaren Kräfte die der Bewertung der optischen Aktivität und der Anwendbarkeitsgrenzen dieses Ansatzes hinzu.

Die Einführung von ab-initio Molekulardynamik im Jahre 1985 [3] hat diese Situation grundlegend geändert (Sec.3.3.2). Im Rahmen eines solchen Schemas ist es heute möglich, die Methoden der selbstkonsistenten Felder auf Systeme sich bewegender Atome auszuweiten. In diesem Ansatz werden die interatomaren Kräfte mit neuesten elektronischen Strukturrechnungen gewonnen, die aus der Dichtefunktionaltheorie (DFT) abgeleitet werden (Sec.3.2.1): auf diese Weise sind sie parameterfrei.

Dank dieser Innovation, die eine zunehmend wichtige Rolle in mehreren Studien verschiedener Materialsysteme gespielt hat, steht jetzt ein Werkzeug zur Verfügung für die Interpretation von Raman und IR Daten auch von flüssigen und ungeordneten Systemen. Es liefert nicht nur eine sehr akkurate Beschreibung der interatomaren Kräfte und mithin ein verlässliches Bild der Struktur von flüssigen und ungeordneten Systemen, sondern es liefert auch alle notwendigen Informationen zum elektronischen Zustand, um IR und Raman Aktivitäten zu interpretieren.

Dies führt zu einer einzigen, vollstndig konsistenten Prozedur, die keinerlei neue Näherungen benötigt. Die einzigen notwendigen Näherungen betreffen die simulierte Systemgröße, Zeitraum und die Qualität der elektronischen Strukturrechnungen.

Allerdings – selbst wenn mit ab-initio Molekulardynamik eine Basis für die Simulation von Raman Spektren von ungeordneten und anharmonischen Systemen geschaffen wurde – sollten auch weiterhin die theoretischen Methoden verbessert werden, um solche Rechnungen durchzuführen.

Insbesondere sind wir interessiert an der Beschreibung der Polarisierbarkeit, das heißt, derjenigen Größe, die für die Ramanstreuung verantwortlich ist. Sie kann als zweite Ableitung der Energie nach dem äusseren elektrischen Feld beschrieben werden. Der einfachste Weg, solch eine Antwortfunktion auszuwerten, ist die Berechnung der Energie für verschiedene Werte des elektrischen Feldes, gefolgt von einer numerischen Differenzierung. Diese Prozedur funktioniert leidlich gut, benötigt aber mehrere Auswertungen der Gesamtenergie und die numerische Ableitung enthält Fehler.

Ein befriedigenderer Ansatz, angewandt bei harmonischen Systemen, ist die direkte Auswertung der Antwortfunktion mit Hilfe der Störungsrechnung. Dies führt im statischen Falle zu einem bekannten Ausdruck für die Antwortfunktion in Form einer Doppelsumme über die besetzten und unbesetzten elektronischen Zustände. Dieser Ansatz wurde umformuliert im Kontext der DFT von Baroni et al.[4] und erfolgreich in vielen Problemen angewandt. Essentiell für den Erfolg war dabei die Sternheimer Methode [5], welche eine explizite Berechnung der nur langsam konvergierenden Summe vermeidet und zusammen mit einem guten Präkonditionierer einen effizienten Algorithmus darstellt.

Trotzdem ist auch diese Simulation sehr rechenintensiv und der Erfolg solch eines Ansatzes ist in der Vereinfachung, die durch Symmetrieeigenschaften harmonischer Kristalle gegeben ist (Sec.6.3).

In einem ungeordneten System, wo solche Eigenschaften fehlen, wird dieser Ansatz zu rechenintensiv. Für eine erste-Prinzipien Simulation von Raman Spektren in

ungeordneten und anharmonischen Systemen benutzt man daher besser eine andere Beschreibung der Polarisierbarkeit.

Zwei wichtige Innovationen können gewinnbringend für unsere Aufgabe eingesetzt werden: die von Gonze et al. [6] eingeführte "variational density functional perturbation theory" (beschrieben in Kap.5), und die "modern theory of polarization" (beschrieben in Kap.4) [7–19].
Entsprechend der ersteren kann man einen Hamiltonian mit einem äusseren Feld stören und die Störungsterme sämtlicher Ordnungen mit einem Variationsansatz berechnen. Unter Benutzung des 2n+1 Theorems [20] kann dann die Änderung der Energie und somit die Energieableitung berechnet werden. Zum Beispiel können die zweiten Ableitungen der Energie berechnet werden, sobald die Störungstherme erster Ordnung für die Kohn-Sham Orbitale bekannt sind.

Die zweite Idee löst das Problem einer angemessenen Beschreibung der Polarisation (und demnach auch der Polarisierbarkeit) in einem periodischen System. Tatsächlich ist eine Beschreibung im Sinne von Clausius-Mossotti, wie sie in Lehrbüchern [21–23] zu finden ist, die auf einem Modell diskreter und gut separierter Dipole basiert, unzureichend: die elektronische Verteilung ist in einem realen Dielektrikum kontinuierlich und oft delokalisiert, wodurch das Dipolmoment einer Einheitszelle von der Wahl der Zelle abhängt. Ausserdem ist der quantenmechanische Ortsoperator für ein periodisches System nicht definiert.

Aus diesen Gründen war die Behandlung der makroskopischen Polarisation für viele Jahre ein große Herausforderung. Im Jahre 1992 gelang dann der Durchbruch. Die makroskopische Polarisation wurde nicht in Abhängigkeit von der Ladung, sondern in Abhängigkeit von der Wellenfunktion definiert. Diese Definition hat einen eindeutigen thermodynamischen Grenzwert, so daß periodische Randbedingungen verwendet werden können. In den folgenden Monaten wurde dank der Arbeit von R. D. King-Smith und D. Vanderbilt [9] eine moderne Theorie der makroskopischen

Polarisation in einem kristallinen Dielektrikum formuliert, die die Polarisation mit Hilfe der Berry-Phase [24] definiert.

Die Kombination dieser beiden neuen Ansätze scheint ein guter Startpunkt für den Aufbau einer neuen effizienten Methode zur Berechnung von ab-initio Ramanspektren zu sein. Nichtsdestotrotz sind einige Probleme noch zu lösen. Der Ansatz von Gonze basiert ebenso wie alle störungstheoretischen Ansätze auf einer geeigneten Definition des Hamiltonoperators. Die Besonderheit der modernen Theorie der Polarisation ist aber, dass die Polarisation ein beobachtbarer Effekt von ganz anderer Art ist als wir es sonst gewöhnt sind: eine Berry-Phase kann nicht in Abhängigkeit von den Eigenwerten irgendeines Operators ausgedrückt werden, also auch nicht in Abhängigkeit vom Hamiltonoperator.

Der Hauptzweck der vorliegenden Arbeit ist, den variationalen Ansatz von Gonze für den Fall eines elektrischen Feldes, das mit der elektrischen Polarisation koppelt, zu verallgemeinern, wenn die Störung nicht mit Hilfe des Hamiltonoperators beschrieben werden kann. Die Verallgemeinerung der variationalen Dichtefunktionalstörungstheorie für ein solches Problem dient nicht nur dem Zweck Ramanspektren von anharmonischen und ungeordneten Systemen zu berechnen, sondern hat auch viele andere Vorteile. Während die konventionelle Dichtefunktionalstörungstheorie in Abhängigkeit der Kohn-Sham-Eigenzustände formuliert werden muss, können in der verallgemeinerten Version auch andere Orbitale verwendet werden. Ein Beispiel hierfür ist die Berechnung von NMR-Verschiebungen [25,26], wofür die Verwendung von maximal lokalisierten Orbitalen vorteilhaft ist.

Weiterhin ist die Ableitung in dieser Arbeit im Geist der DFT erfolgt und unserer Meinung nach etwas transparenter als die von Gonze[6]. Natürlich reduzieren sich unsere Ausdrücke für den Fall einer Störung des Hamiltonoperators auf die Ausdrücke von Gonze. Nach der Durchführung einiger Tests (Schwingungsfrequenzen, molekulare Polarisierbarkeiten, Raman-Intensitäten) zeigt diese Ar-

beit die Leistungfähigkeit der neuen Methode anhand eines interessanten Systems: Hochdruck-Eis.

Der allgemeine Beweggrund zu solch einer Wahl ist die in einer der wichtigsten Abhängigkeit in der Natur nachzuforschende Möglichkeit, die Wasserstoffbrückenbindung. Das letzte ist verantwortlich von einigen Phänomenen, die in vielen Bereichen der Wissenschaft interessant sind und reicht von der Biologie bis zu planetarischer Physik. Insbesondere ist diese Bindung der Grund des sehr schwierigen Zustandsdiagramms des Wassers, das das häufigsten Molekül auf der Erdoberfläche ist und über 70% des menschlichen Körpers darstellt.

Gewöhnliches Eis (Eis Ih), das bei Atmosphärendruck stabil ist, ist nur eine der vielen Phasen von Eis. Das Druck-Temperatur-Diagramm von Eis gliedert sich in mindestens 14 unterschiedliche Bereiche mit entsprechend vielen Arten von Eis, die sich alle bestimmten amorphen oder kristallinen Netzwerken von H_2O-Molekülen zuordnen lassen.

Die Hochdruckregion des Zustandsdiagramms ist für Festköperforshung, planetarische Physik[27] und Biologie sehr wichtig. Tatsächlich werden die betroffenen Phase übergänge durch die sehr interessanten Phänomene der Protonenübertragung gekennzeichnet. Ähnliche Phänomene geschehen im Kern einiger Planeten, wie Saturn-, Uranus- und Neptun[27]. Ausserdem ist die Studie des Eises eine drastische Vereinfachung verglichen mit Körpern mit Wasserstoffbrückenbinden am umgebenden Druck, an den Systemen in den Gas- oder Flüssigkeitphasen oder sogar an den 'biomoleküle'. So ist Eis an der hohen Komprimierung ein ideale Substanz zum Durchführen von Experimenten und von Simulationen, in denen das Protonenübergangspotential als Funktion des angewandten externen Drucks justiert werden kann, d.h. ohne den chemischen Aufbau des Körpers zu ändern. Die Studie des Verhaltens dieses vereinfachten Systems darf in den ähnlichen Phänomenen, die in den viel komplizierteren biologischen Systemen geschehen, wie zum Beispiel dem

HIV-Enzym[28].

Insbesondere in den letzten 25 Jahren, wurden die Studien des Phase Überganges von Eis VIII zum Eis X[29] stark forciert.
Jedoch erst seit kurzem hat die Entwicklung der neuen experimentellen Techniken, die am Hochdruck arbeiten dürfen, und der leistungsfähigen Simulation Hilfsmittel gegeben die Möglichkeit einer tiefen Untersuchung solcher phenomena.

Eis VIII hat die einfachste Struktur von allen Eisphasen. Sie besteht aus zwei sich durchdringenden Schichten von H-verbrückten Wassermolekülen, die aber nicht miteinander verbunden sind, wobei die Sauerstoffatome eine leicht tetragonal verzerrte kubisch innenzentrierte Struktur (tetragonale antiferroelektrische Phase) bilden [30].
Wenn der Druck erhöht wird, entsteht eine neue Phase, Eis VII. Dieser Phasenübergang hat einen klaren experimentellen Fingerabdruck, das Verschwinden der tetragonal Verzerrung. Es gibt Protonstörung und das Proton besetzt mit gleiche symmetrischen Positionen der Wahrscheinlichkeit zwei entlang der O-O Bindung und gibt eine abschließende Struktur, die ungeordnet und paraelektrisch ist [31, 32]. In der Unterdruckregion und bei hoher Temperaturen, wird die Störung dieser Struktur angenommen, durch die Rotationen der Moleküle verursacht werden, die Defekte Bejerrum erstellt, während unter Hochdruck, die dominierende Einheit thermisches Hopfen und/oder Einen Tunneln des Protons entlang der Wasserstoffbrückenbindung ist.

Bei noch größeren Drücken wird über eine weitere Phase, Eis X, spekuliert, deren molekulare Struktur völlig zusammengebrochen und in eine nicht molekulare Struktur (Cuprit-Typ), verknüpft durch druckinduzierte, symmetrische Wassertstoffbrückenbindungen, übergegangen ist [33–36].

Die Phasengrenzen zwischen Eis VIII und VII sind genau bestimmt und durch den

Verlust der tetragonalen Verzerrung in Phase VII gekennzeichnet. Hingegen sind die Grenzregionen von Eis X nicht genau bekannt [37], da eine eindeutige Identifikation der H-Brückenbindungssymmetrie strukturelle Hilfsmittel benötigt, die das Wasserstoffteilgitter auflösen können. Diese fehlen bis heute. Röntgenstreudaten wurden bis zu 128 GPa erhalten, lieferten jedoch keine Informationen über das Protonenteilgitter, während Studien mit Hilfe von Neutronenbeugung, die in der Lage ist, die Positionen der Protonen zu lokalisieren, nur bis zu 20 GPa durchgeführt wurden. Dies liegt daran, daß die Probengrößen, die bei höheren Drücken hergestellt werden können, viel zu klein sind, um diese Technik anzuwenden. Experimente, *ab initio* molekular dynamische Simulationen [44] und Berechnungen von Infrarotspektren [43] zeigen, daß Eis VIII nicht direkt in Eis X übergeht, sondern daß sich der Phasenübergang vielmehr zwischen Eis VII und Eis X ereignet. Die Grenzregionen dieses Phasenübergangs sind immer noch nicht völlig aufgeklärt. Es wird vermutet [37], daß bei steigendem Druck das rotationsgestörte Eis VII in das translationsgestörte Eis VII übergeht. Diese Phase wandelt sich dann in protonenungeordnetes Eis X um, welches bei weiterer Kompression in protonengeordnetes Eis X übergeht.

Die Experimente unter Hochdruck sind sehr schwierig. Die Einführung der Diamantamboß-Zell Technike hat die Möglichkeit eröffnet, optische Messungen durchzuführen. Die Resultate dieser Experimente sind umstritten, weil das durch die Probe erhaltene Signal verglichen mit dem Signal der Diamantamboßzelle sehr kleines ist und weil sogar die genaue Ermittlung des Druckes der Probe schwierig ist. Außerdem wird Unsicherheit auch durch die Notwendigkeit verursacht, mit unterschiedlichen Spectrometern die unterschiedlichen Regionen des Frequenzgebietes zu untersuchen.

Des weiteren erfordert die ungeordnete Natur von Eis VII die Verwendung von *ab initio* Simulationen.

Nach Bestätigung der experimentellen IR-Spektren von A. F. Goncharov et al. [40,

41] durch *ab initio* Simulationen von M. Bernasconi et al. [43] führte die gleiche experimentelle Gruppe ebenfalls Raman Messungen [42] durch. Letztere vervollständigen das Bild, das sich aus den IR-Spektren ergibt und scheinen die Existenz von Eis X bei sehr hohen Drücken zu bestätigen. Die Messung dieser Spektren gestaltet sich aufgrund des geringen Streuquerschnittes der Materialien bei diesen Drücken als sehr schwierig. Um die Gültigkeit der experimentellen Daten zu zeigen und diesen sehr bedeutenden Phasenübergang weiter zu erforschen, habe ich in der vorliegenden Doktorarbeit eine Methode entwickelt, mit der wir *ab initio* Simulationen von Raman Spektren nichtgeordneter und anharmonischer Systeme durchführen konnten.

Die simulierten Spektren stimmen gut mit den von A.F. Goncharov et al. durchgeführten Experimenten überein, wie in den Abbildungen 7.7.6 und 7.7.7 zu erkennen. Bei niedrigen Drücken ist das Spektrum des Eis VIII von den hochfrequenten O-H Valenzschwingungen dominiert: sie bilden ein Triplett (ein Dublett und eine schmale Schulter), welches den Moden $\nu_1(A_{1g})$, $\nu_3(E_g)$, und $\nu_1(B_{1g})$ in der Reihenfolge steigender Frequenz und niedrigen Druckes zugeordnet werden kann. Das Hochfrequenzband $\nu_1(A_{1g})$ zeigt die größte Verschiebung bei Druckanwendung. Während sich diese Mode zu niedrigeren Frequenzen verschiebt, vergrößern sich die Intensitäten der anderen Banden nacheinander von der hohen zur niedrigen Frequenz, um bedeutende Resonanzen zu erzeugen, die abhängig vom Druck erscheinen oder verschwinden. Bemerkenswert ist die Resonanz bei 38 GPa, die in einem Bereich (1650 cm^{-1}) liegt, in dem die experimentellen Ergebnisse aufgrund der Anwesenheit des Signals der Diamantamboßzelle eine größere Unsicherheit haben. In unseren Simulationen ist die ausgesprochene Resonanz nicht sichtbar, jedoch einige kleinere Strukturen dieser Frequenzregion, die sich klar im experimentellen Spektrum wiederfinden. Im niedrigen Frequenzbereich und bei tiefer Temperatur ist das Spektrum von den scharfen Translationsbanden $\nu_{T_z}(A_{1g}) + \nu_{T_{xy}}(E_g)$ und

$\nu_{T_z}(B_{1g})+\nu_{T_{xy}}(E_g)$, die den Anregungen von Eis VIII bei 400 und 500 cm^{-1} zuzuordnen sind, dominiert. Sie zeigen nur eine geringfügige Verschiebung der Frequenz bei 45-60 GPa, die über 60 GPa vermindert und verbreitert ist und dann eine mit dem Druck ansteigende Frequenz zeigt. Bei hoher Temperatur zeigt sich in unserer Simulation nur eine breite Translationsbande $\nu_{T_z}(B_{1g}) + \nu_{T_{xy}}(E_g)$, von der auch in den Experimenten berichtet wurde [42]. Mit steigendem Druck erscheint eine neue Bande, während alle anderen Anregungen sich nur schwach zeigen. Diese neue Bande kann der T_{2g} O-O Schwingung zugeordnet werden, wie für die C_2O Cuprit-Sruktur zu erwarten.

Zusammenfassend läßt sich sagen, daß unsere *ab initio* Simulation der Raman Spektren eine weitere Bestätigung für die nichtmolekulare Struktur von Eis unter Hochdruck ist. Des weiteren bestätigt sie die experimentellen Daten, welche andernfalls aufgrund der technischen Probleme, die mit diesen Messungen verbunden sind, kontrovers wären. Mit großer Wahrscheinlichkeit besitzt diese nichtmolekulare Hochdurckphase von Eis, Eis X, die Cupritstruktur. Eine Gewißheit über diese Phase kann nur durch Neutronenstreuexperimente erhalten werden, die es vermögen, die einzelnen Positionen der Protonen zu lokalisieren. Letztlich allerdings scheinen dies alle IR-,Ramanexperimente und Simulationen zu bestätigen.

Chapter 2

Introduction

Over the years Raman scattering experiments have provided precious information on the dynamics of nuclei and their interaction with the electronic state [1].
In fact, they are (together with infrared (IR) optical experiments) one of the main experimental tools with which condensed matter properties are investigated.
Not only do many laboratories have access to the appropriate experimental facilities, but also the theoretical interpretation of the experimental data is often straightforward. This is especially true in periodically ordered solids, where symmetry restricts the number of optically active modes.
However, in disordered systems or in systems where strong anharmonic effects are present, these theoretical tools are of limited use: disorder relaxes all selection rules leading to broad and complex spectra which are difficult to interpret. This is one of the reasons why IR and Raman scattering have not had quite the same impact in disordered systems as in ordered crystals.

Much effort [2] has been devoted to remedy this situation, mostly based on molecular dynamics simulation methods (described in Chap.3), a tool of choice when dealing with disordered systems.

Using effective potentials that are constructed to describe the interatomic interaction between the particles, it is possible to simulate the time evolution of the system and generate appropriate models for the disordered structures. However, properties like IR and Raman activities depend on the ion structure and dynamics as well as on electronic properties like the electronic dipole moment and polarizability. These properties are not included in the standard molecular dynamics models and additional parametrisation is needed to describe the IR and Raman activity. Thus, the uncertainty on the interatomic forces is compounded with that of the evaluation of the optical activity and limits the usefulness of this approach.

The introduction in 1985 of *ab initio* molecular dynamics [3] has changed this situation substantially (Sec.3.3.2). Within such a scheme, it is now possible to apply *ab initio* methods to systems of atoms in motion. In such an approach the interatomic forces are evaluated using state-of-the art electronic structure calculations based on density functional theory (DFT) (Sec.3.2.1): in this way they are parameter-free and derived from first-principles, with no experimental input.

Thanks to this innovation, which has played an increasingly important role in several kinds of studies of materials, there is now a tool available for interpreting Raman and IR data in liquids and disordered systems. In fact, not only does this provide a rather accurate description of the interatomic forces and therefore a reliable description of the structure of liquids and disordered systems, but it also provides informations on the electronic structure. This information can be used in principle to evaluate IR and Raman activities. In such a way one follows a fully consistent procedure that does not involve any new approximations. The approximations only are those contained in the *ab initio* molecular dynamics run and are related to the system size, the time length of the simulation and the quality of the electronic structure theory used.

However, even if *ab initio* molecular dynamics constitutes the theoretical basis for

the construction of first-principles simulations of Raman spectra of disordered and anharmonic systems, still a lot of additional theoretical tools need to be developed in order to perform such a calculation.

In particular, the Raman cross section, for the case in which the incident light has a frequency much smaller than that of electronic excitations, can be related to the polarizability-polarizability correlation function. For this reason, we shall first address the issue of calculating the polarizability.

This can be expressed as the second derivative of the energy with respect to the external electric field. The simplest way to evaluate such a response function is to calculate the energy for various values of the applied field and numerically extract the energy derivatives. This procedure can work reasonably well, but it requires several evaluations of the total energy and the numerical derivative introduces errors.
A more satisfactory approach is to evaluate the response functions directly, making use of perturbation theory. For the static response functions this leads to a familiar expression of the response function in terms of a double sum over the occupied and empty electronic states. This approach has been reformulated in the context of DFT by Baroni et al.[4] and successfully applied to many problems. An essential ingredient for the success of this approach has been the use of the Sternheimer method [5] which avoids the explicit evaluation of the poorly convergent double sum and together with a good preconditioner leads to an efficient algorithm.
However, the cost of the simulation is still very high and the success of such an approach is based on the fact that symmetry properties of crystals, where the harmonic approximation holds, reduce the complexity of the problem: in fact, in this case it is possible to approximate the polarizability by its expansion up to first order terms in normal modes, as we explain in detail in Sec.6.3; in this way, one should evaluate only zero order coefficients and first order derivatives of the polarizability

at the equilibrium and phonons.
In a disordered system, where one cannot use this approximation, this approach becomes computationally too expensive. In order to achieve the goal of a first-principles Raman spectrum simulation for disordered and anharmonic systems it is better to use a different description of the polarizability.
Recently two important innovations were introduced, which will be useful to our purpose: variational density functional perturbation theory (described in Chap.5), introduced by Gonze et al. [6] and the modern theory of polarization (described in Chap.4) [7–19].

The first has shown that if one perturbs the Hamiltonian with an external field, the induced variation in the Kohn-Sham orbitals can be obtained to all perturbative orders from a variational formulation. Use of the $2n+1$ theorem[20] then allows the calculation of the change in energy and the corresponding energy derivatives. For instance the second order energy derivatives can be calculated once the first order variation in the Kohn-Sham orbitals is known.

The second, finally, solves the problem of an appropriate definition of the macroscopic polarization (and consequently of the polarizability) in a periodic system. In fact, a description, as is found in all textbooks [21–23], à la Clausius-Mossotti, i.e. in terms of a model of discrete and well separated dipoles is inadequate: the electronic distribution of a real dielectric is continuous and often delocalized and the resulting dipole moment of a unit cell depends on the choice of the cell. Furthermore, the quantum-mechanical position operator is ill-defined in a periodic system.

For these reasons, macroscopic polarization remained a major challenge for many years. In 1992 there was a breakthrough. Macroscopic polarization was defined in terms of the wavefunction phases, not of the charge. This definition has an unambiguous thermodynamic limit, such that periodic boundary conditions can be used. In the following years a modern theory of macroscopic polarization in

crystalline dielectrics has been completely established, thanks to the work of R.D. King-Smith and D. Vanderbilt [9], who expressed polarization in terms of a Berry phase [24].

The combination of these two recent developments promises a good starting point for constructing a new efficient method that allows the calculation of first-principles Raman spectra. However, still more effort is required. In fact, Gonze's approach as well as the more standard perturbation theory is based on a Hamiltonian formulation. Instead, a particular feature of the modern theory of polarization is that the latter is an observable effect of a completely different nature from what we are usually familiar with: a Berry phase is something that cannot be expressed in terms of eigenvalues of any operator, in other words in terms of a Hamiltonian.

The main purpose of this thesis is to generalize the Gonze variational approach to the case in which the perturbation cannot be expressed in a Hamiltonian form, in order to be able to treat an electric field which couples with the electric polarization. The effort to generalize variational density functional perturbation theory to such a problem addresses not the only issue of calculating Raman spectra of anharmonic and disordered systems, but also has other advantages. In fact, while conventional perturbation theory must be formulated in terms of Kohn-Sham eigenstates, in this generalized version one can work also with other orbitals. A case in point is for instance the calculation of NMR chemical shifts which can profit from the use of maximally localized orbitals[25,26].

Furthermore, the derivation of this thesis is very close to the spirit of DFT and in our opinion slightly more transparent than that of Gonze[6]. Of course the formulae reduce to those of Gonze in the case of Hamiltonian perturbations.

After preliminary tests (vibrational frequencies, polarizability of molecules, Raman intensities), this thesis shows the power of the new method in the case of an inter-

esting system: high pressure ice.

The principal motivation for such a choice is the possibility of investigating one of the most important interactions in nature, the hydrogen bond. The latter is responsible for several phenomena, which are of interest in many areas of science, ranging from biology to planetary physics. In particular, this bond is the reason for the very complicated phase diagram of water, which is the most common molecule on the earth's surface and constitutes about 70% of the human body. Ordinary ice (ice Ih), which is stable at atmospheric pressure, is only one of many phases of ice: in fact, at least 14 varieties of solid ice have been observed in various domains of the pressure-temperature plane, which correspond to different amorphous or crystalline networks of the H_2O molecule.

The high pressure region of the phase diagram is very important for condensed matter, planetary physics [27] and biology. In fact, the phase transitions involved are characterized by the very interesting phenomenon of proton transfer. Similar phenomena happen in the heart of some planets, like Saturn, Uranus and Neptune [27]. Furthermore, the study of ice is much simpler than the study of hydrogen-bonded solids at ambient pressure, systems in the gas or liquid phases, or even 'biomolecules'. Thus, ice at high pressure is an ideal candidate for performing experiments and simulations, in which the proton transfer potential can be tuned as a function of the applied external pressure, i.e. without changing the chemical composition of the solid. The study of the behavior of this simplified system allows us to investigate the basis of a phenomenon, which is common in many biological systems, for example the HIV protease [28], which is the enzyme responsible for this disease .

In particular, in the last 25 years, a lot of effort has been dedicated to the study of the phase transition from ice VIII to ice X[29]. However, only very recently has the development of new experimental techniques, which permit to work at very high pressures, and of powerful simulation tools open up the possibility of a deeper

investigation of such phenomena.

Ice VIII has one of the simplest structures of any of the phases of ice. It is composed of two interpenetrating but not interconnected sublattices of hydrogen bonded water molecules, where the oxygen atoms form a slightly tetragonally distorted body-centered-cubic structure (tetragonal antiferroelectric phase) [30]. As the pressure increases a new phase appears, ice VII. This phase transition has a clear experimental fingerprint, the disappearance of the tetragonal distortion. Proton disorder sets in and the proton occupies with equal probability two symmetric positions along the O-O bond, giving a final structure which is disordered and paraelectric [31,32]. In the low-pressure region and at high temperature, the disorder of this structure is believed to be induced by the rotations of molecules, which creates Bejerrum defects, whereas at high pressures, the dominant mechanism is thermal hopping and/or tunneling of the proton along the hydrogen bond.

At even higher pressures it is speculated that another phase exists, ice X[33–36], where the molecular-crystal structure breaks down completely and transforms into a non-molecular structure (Cu_2O type) connected by hydrogen bond symmetrization induced by the pressure.

The boundaries between ice VIII and VII in the phase diagram are well defined and identified by the loss in phase VII of the tetragonal distortion. However, the boundary regions of ice X are still not well defined [37], because a definite identification of the H-bond symmetrization requires structural tools able to probe the H sublattice. These are still lacking. X-ray diffraction data were obtained up to 128 GPa [38] but provided no information about the proton sublattice, while neutron diffraction studies, which are able to locate the H positions, have been reported only up to 20 GPa [39], because the only samples which can be brought to higher pressure are too small to apply this technique. The experimental information is somewhat indirect and relies heavily on IR measurements [40,41] and, more recently, on Raman scat-

tering[42]. For this reason, numerical simulations can be extremely useful in helping to really understand the nature of the transition. So far only the IR spectrum has been simulated [43]. This, together with first-principles path integral molecular dynamics [44], has led to a scenario in which ice VIII does not transform directly into ice X, but the phase transition happens between ice VII and X. However, the boundaries of this phase transition are still not completely clear. It is supposed [37] that, with increasing pressure, rotational-disordered ice VII, transforms into translational-disordered ice VII. This phase then transforms into proton-disordered ice X, which under further compression transforms into proton-ordered ice X.

The more recent Raman scattering experiments, performed by A.F. Goncharov et al.[42], have, however, not been interpreted. This experiment is particularly difficult, because the signal obtained by the sample is very small compared with the signal of the diamond anvils cell and because even the exact determination of the pressure of the sample is difficult. Furthermore, some uncertainty is also introduced by the need to use different spectroscopes in different regions of the frequency domain.
Our calculations show good agreement between experiment and theory. This agreement gives support both to theory and experiment. The analysis of the spectrum based on the molecular dynamics trajectories allow us to attribute unambiguously many of the relevant experimental peaks. Our results further strengthen our understand of this important and complex phase transition.

Chapter 3

Ab initio theories

The exact quantum mechanical treatment of systems consisting of nuclei and electrons is not possible at present. Fortunately physical and chemical intuition suggest the use of several well obeyed approximations, which may render numerical calculations affordable.

The first approximation is the Born-Oppenheimer approximation, which allows the separation of the nuclear degrees of freedom from the electronic ones. This separation allows a transformation of a very complicated many-electron problem in a set of single particle equations, using density functional theory. This single particle transformation is probably the most critical approximation. Finally, the core states are eliminated using the pseudopotential approximation.
The single particle transformation is probably the most critical one.

3.1 The Born Oppenheimer approximation

The Schrödinger equation for a system containing n electrons and N nuclei is given by

$$H\Psi(\mathbf{r}_1,..,\mathbf{r}_n,\mathbf{R}_1,..\mathbf{R}_N) = E\Psi(\mathbf{r}_1,..,\mathbf{r}_n,\mathbf{R}_1,..\mathbf{R}_N)\,, \tag{3.1.1}$$

with

$$\begin{aligned} H = &\sum_i -\frac{1}{2}\nabla_i^2 + \sum_I -\frac{1}{2M_I}\nabla_I^2 + \frac{1}{2}\sum_{i\neq j}\frac{1}{|\mathbf{r}_i-\mathbf{r}_j|} + \\ &\frac{1}{2}\sum_{I\neq J}\frac{Q_IQ_J}{|\mathbf{R}_I-\mathbf{R}_J|} - \sum_{iI}\frac{Q_I}{|\mathbf{r}_i-\mathbf{R}_I|}\,, \end{aligned} \tag{3.1.2}$$

where $\{\mathbf{r}\}$ are the electronic coordinates, $\{\mathbf{R}\}$ the ionic coordinates, M_I and Q_I are the masses and charges of the nuclei in atomic units. The Born Oppenheimer (BO) [45] approximation is based on the fact the mass of the electrons is much smaller than the mass of the ions. This implies that the typical electronic velocities are much greater than the typical ionic velocities. So one assumes that because ions move so slowly compared to the velocity scale of the electrons, that at any instant the electrons will be in their ground state configuration for that particular instantaneous configuration. This allows Eq.(3.1.1) to be decoupled into two separate equations, the time-independent Schrödinger equation of the electrons moving in the field of the nuclei fixed in the positions $\mathbf{R}_I$:

$$\begin{aligned} \left[\sum_i -\frac{1}{2}\nabla_i^2 + \frac{1}{2}\sum_{i\neq j}\frac{1}{|\mathbf{r}_i-\mathbf{r}_j|} - \sum_{iI}\frac{Q_I}{|\mathbf{r}_i-\mathbf{R}_I|}\right]\Psi^{el}_{\mathbf{R}_1,..\mathbf{R}_N}(\mathbf{r}_1,..,\mathbf{r}_n) \\ = E_n^{el}(\mathbf{R}_1,..\mathbf{R}_N)\Psi^{el}_{\mathbf{R}_1,..\mathbf{R}_N}(\mathbf{r}_1,..,\mathbf{r}_n)\,, \end{aligned} \tag{3.1.3}$$

and the nuclear wave equation:

$$\begin{aligned} \left[\sum_I -\frac{1}{2M_I}\nabla_I^2 + \frac{1}{2}\sum_{I\neq J}\frac{Q_IQ_J}{|\mathbf{R}_I-\mathbf{R}_J|} + E_n^{el}(\mathbf{R}_1,..\mathbf{R}_N)\right]\Psi^{nc}(\mathbf{R}_1,..\mathbf{R}_N) = \\ E_n^{nc}(\mathbf{R}_1,..\mathbf{R}_N)\,\Psi^{nc}(\mathbf{R}_1,..\mathbf{R}_N)\,. \end{aligned} \tag{3.1.4}$$

The total wavefunction is then given by the product of the nuclear and electronic part

$$\Psi(\mathbf{r}_1,..,\mathbf{r}_n,\mathbf{R}_1,..\mathbf{R}_N) = \Psi^{el}_{\mathbf{R}_1,..\mathbf{R}_N}(\mathbf{r}_1,..,\mathbf{r}_n)\Psi^{nc}(\mathbf{R}_1,..\mathbf{R}_N)\,,$$

and the total energy by

$$E^{tot}_n(\mathbf{R}_1,..\mathbf{R}_N) = E^{nc}_n(\mathbf{R}_1,..\mathbf{R}_N)\,.$$

Since the mass of the nuclei is very large, they behave nearly like classical particles. The total energy for stationary atoms is given in this classical approximation by

$$E^{tot}_n(\mathbf{R}_1,..\mathbf{R}_N) = E^{el}_n(\mathbf{R}_1,..\mathbf{R}_N) + \frac{1}{2}\sum_{I\neq J}\frac{Q_I Q_J}{|\mathbf{R}_I-\mathbf{R}_J|}\,. \tag{3.1.5}$$

The function $E^{tot}_n(\mathbf{R}_1,..\mathbf{R}_N)$ is called the Born Oppenheimer or potential energy surface. There are several branches of this surface corresponding to different electronic eigenvalues. The equilibrium configuration of a system is given by the global minimum of the lowest branch of this function ($n=0$). In the following discussion, we assume to be at the minimum and thus we can suppress the index n.

The same classical approximation can be applied for slowly moving atoms which leads to the expression

$$E_{tot} = E^{el}(\mathbf{R}_1,...,\mathbf{R}_N) + \sum_{I\neq J}\frac{Q_I Q_J}{|\mathbf{R}_I-\mathbf{R}_J|} + \sum_I \frac{1}{2M_I}\dot{\mathbf{R}}_I^2\,.$$

The above expression is the starting point for *ab initio* molecular dynamics simulations.

3.2 Many-body electronic wave equation

After applying the BO approximation we are left with the many body electronic equation:

$$\left(-\frac{1}{2}\sum_i \nabla_i^2 + v_{ext}(\mathbf{r}_i) + \sum_{i\neq j}\frac{1}{|\mathbf{r}_i-\mathbf{r}_j|}\right)\Psi(\mathbf{r}_1,..,\mathbf{r}_n) = E^{el}\Psi(\mathbf{r}_1,..,\mathbf{r}_n)\,, \tag{3.2.1}$$

where $v_{ext}(\mathbf{r}_i)$ contains the electron ion potential and possibly other external potentials. Only for a few simple or simplified systems, an exact solution of Eq.(3.2.1) can be obtained [46]: the long range Coulombic interaction of the electrons couples all the degrees of freedom and it is hopeless any effort (not only analytic, but also numeric) to obtain the exact many body wavefunction in all the space. In order to overcome this difficulty, there are essentially three different approaches to the many-body Schrödinger equation:

- Quantum Monte Carlo methods :

  They all use the theory of the Monte Carlo integration [47] in order to calculate multidimensional integrals with a computational effort independent from the dimensionality.

  This method is a statistical method: the accuracy of result is proportional to $1/\sqrt{M}$, where M is the number of sampling points used in the calculation. This means that, in principle, one can reduce the error on the calculation to arbitrary precision, performing longer and longer runs.

  Furthermore, they are true many-body approaches. In practice , these methods suffer from four problems that make them still far away to be useful for the study of realistic systems: *i*) they are very expensive because they require an extensive sampling in order to achieve a reasonable accuracy, *ii*) atoms with high nuclear charge Z critically slow down the calculation, *iii*) the sign problem [48] for fermionic systems is still not solved, *iv*) and finally there is not at present a sufficiently accurate way to calculate the electronic forces [1].

  There are three mainstreams of Monte Carlo methods [50,51]: 1) the variational quantum Monte Carlo, which allows the calculation of the ground state properties of a many body system, of which one has a trial wavefunction

[1] Only very recently a promising method for an accurate evaluation of the forces was proposed by C. Filippi et al.[49]

physically reasonable, flexible and too complicated to be able to estimate the multidimensional integrals in a traditional way, 2) the diffusion and Green's function Monte Carlo [50,52,53], that map the Schrödinger equation onto a diffusion equation, and 3) the Monte Carlo using the Hubbard Stratonovitch transformation [54].

- Quantum chemistry methods such as Hartree-Fock, configuration interaction [55], multi configuration Hartree-Fock [56], multi reference configuration interaction methods [57] and, coupled clusters [58] are based on the fact that any antisymmetric many-electron wavefunction can be written as an infinite sum over Slater determinants.

  The Hartree-Fock theory is the oldest and best known mean field approximation. There the wavefunction is written as a single Slater determinant and the one-particle orbitals are varied to minimize the total energy.

  The configuration interaction method expands the wavefunction into many Slater determinants and the coefficients multiplying each determinant are varied to find the minimum of the total energy.

  In the multi configuration Hartree-Fock method both the coefficients of the determinants and the one-particle orbitals in each determinant are varied to find the minimum.

  The coupled cluster method improves the single Slater determinant approximation using cluster functions and the exponential Ansatz. At the present coupled cluster method is the most accurate method for the calculation of the electronic properties. Similar to the configuration interaction methods, it requires a high computational effort and can therefore only be applied to small systems.

- Density functional theory (DFT): in this method the many-body problem is substituted with a set of single-particle equations that are self-consistency con-

strainted. This transformation introduced 1964 by Hohenberg and Kohn[59] is in principle exact.

In the following we will describe the DFT, which is the electronic structure method used in this thesis.

3.2.1 Density Functional Theory

As discussed in the previous section, in order to study some important properties of the ground state of a many-electron system, it is possible to substitute Eq.(3.2.1) with a system of one-particle equations with self-consistency constraints. These single particle equations can be obtained through variational approximations, such as Hartree-Fock, but they may also be derived without approximations, from the Density Functional Theory (DFT), introduced by Hohenberg and Kohn [59], through their two theorems.

The first theorem of Hohenberg e Kohn legitimizes the use of the electron density $n(\mathbf{r})$ as basic variable. It states: "The external potential $v_{ext}(\mathbf{r})$ is determinated, within a trivial additive constant, by the electron density". Since $n(\mathbf{r})$ determines the number of electrons, it follows that $n(\mathbf{r})$ also determines the ground state wavefunction and all the other electronic properties. This means that the energy can be written as a unique functional of the density. We note also that $v_{ext}(\mathbf{r})$ is not restricted to Coulomb potentials.

The proof of this theorem is disarmingly simple: all that is employed is the minimum-energy principle for the ground state. Consider the electron density $n(\mathbf{r})$ for the nondegenerate ground state. If there were two external potentials v_{ext} and v'_{ext} differing by more than a constant, each giving the same $n(\mathbf{r})$ for its ground state, we would have two Hamiltonian H and H' whose ground-state densities were the same although the normalized wavefunctions Ψ and Ψ' would be different. Taking Ψ' as

a trial function for the H problem, we would then have:

$$E_0 \leq \langle \Psi' | H | \Psi' \rangle = \langle \Psi' | H' | \Psi' \rangle + \langle \Psi' | H - H' | \Psi' \rangle$$
$$= E_0' + \int d^3r \; n(\mathbf{r})[v_{ext}(\mathbf{r}) - v_{ext}'(\mathbf{r})], \tag{3.2.2}$$

where E_0 and E_0' are the ground state energies for H and H' respectively. Similarly taking Ψ as trial function for the H' problem,

$$E_0' \leq \langle \Psi | H' | \Psi \rangle = \langle \Psi | H | \Psi \rangle + \langle \Psi | H' - H | \Psi \rangle$$
$$= E_0 + \int d^3r \; n(\mathbf{r})[v_{ext}'(\mathbf{r}) - v_{ext}(\mathbf{r})]. \tag{3.2.3}$$

Adding Eqs.(3.2.2) and (3.2.3), we would obtain

$$E_0 + E_0' \leq E_0' + E_0,$$

a contradiction, and so there cannot be two different v_{ext} that give the same density for their ground state.

Thus, the electron density determines the number of electrons N and the potential v_{ext} and hence all the properties of the ground state, for example the kinetic energy $\mathcal{T}[n]$, the potential energy $\mathcal{V}[n]$ and the total energy $\mathcal{E}[n]$. We can write, making explicit the dependence on v_{ext}

$$\mathcal{E}_v[n] = \langle \Psi | T + V | \Psi \rangle$$
$$= \mathcal{F}[n] + \int d^3r \; v_{ext}(\mathbf{r}) n(\mathbf{r}), \tag{3.2.4}$$

where in $\mathcal{F}$ there is no explicit dependence from the external potential v_{ext}.

This means that the total energy $\mathcal{E}[n]$ is a functional of the electron density only.

The second theorem of Hohenberg and Kohn provides the energy variational principle. It reads: "For a trial density $\tilde{n}(\mathbf{r})$ such that $\tilde{n}(\mathbf{r}) \geq 0$ and $\int d^3r \, \tilde{n}(\mathbf{r}) = N$,

$$E_0 \leq \mathcal{E}_v[\tilde{n}], \tag{3.2.5}$$

where $\mathcal{E}_v[\tilde{n}]$ is the energy functional of Eq.(3.2.4)". To prove this theorem, we note that the previous theorem assures that $\tilde{n}$ determines each own $\tilde{v}_{ext}$, Hamiltonian H and wavefunction $\tilde{\Psi}$, which can be taken as a trial function for the problem of interest having the external potential v_{ext}. Thus,

$$\langle\tilde{\Psi}|H|\tilde{\Psi}\rangle = \int d^3r\ v_{ext}(\mathbf{r})\tilde{n}(\mathbf{r}) + \mathcal{F}[\tilde{n}] = \mathcal{E}_v[\tilde{n}] \geq \mathcal{E}_v[n]. \tag{3.2.6}$$

However, the explicit form of $\mathcal{F}[n]$ is not known.

In order to turn DFT into a practical tool for rigorous calculations, Kohn and Sham [60] invented an ingenious indirect approach to the functional $\mathcal{F}[n]$.

They have introduced a fictitious, non physical, system of independent electrons in an appropriated efficient potential $V_{eff}(\mathbf{r})$ chosen in a way that the density of such an auxiliary system is equal to the density of the physical system. The non-interacting system is described exactly from the one-particle spatial wavefunctions $|\psi\rangle$ and its electron density is for construction equal to the interacting system electron density and reads:

$$n(\mathbf{r}) = \sum_i f_i|\psi(\mathbf{r})|^2, \tag{3.2.7}$$

where f_i is the fermionic occupation number, varying between 0 and 2, in accordance to the Pauli exclusion principle. Once this fictitious system is introduced, one can subtract from $\mathcal{F}[n]$ other known functionals, like the classical coulombic energy of the charge distribution $n(\mathbf{r})$ (Hartree term):

$$\mathcal{E}_H[n] = \frac{1}{2}\int d^3r \int d^3r' \frac{n(\mathbf{r})n(\mathbf{r}')}{|\mathbf{r}-\mathbf{r}'|} \tag{3.2.8}$$

and the kinetic energy of the non-interacting electron gas:

$$\mathcal{T}_s[n] = -\frac{1}{2}\sum_i f_i\langle\psi|\nabla^2|\psi\rangle. \tag{3.2.9}$$

To show that $\mathcal{T}_s[n]$ is a unique functional of the only electron density is immediate: it is a particular case ($V = v_{ext}$) of the functional $\mathcal{E}[n]$.

If we subtract from $\mathcal{F}[n]$ (3.2.4) the terms (3.2.8) and (3.2.9), we obtain a new functional, where we have isolated all the many body quantum effects, which are not included in the classical electrostatics and in the non-interacting gas kinetic energy:

$$\mathcal{E}_{xc}[n] = \mathcal{F}[n] - \mathcal{E}_H[n] - \mathcal{T}_s[n]. \tag{3.2.10}$$

This functional is called exchange and correlation functional in analogy with the energetic terms that one obtains from the approximated Hartree-Fock theory. If the explicit form of this functional were known, we can calculate the ground state electron density for a fixed external potential minimizing the total energy (3.2.4) with respect to the electron density $n(\mathbf{r})$, with the constraint:

$$\int d^3r \; n(\mathbf{r}) = N. \tag{3.2.11}$$

This is equivalent to solve a set of single-particle differential equations for the $|\psi\rangle$ with the constraint of self-consistency:

$$(-\frac{1}{2}\nabla_i^2 + V_{eff})|\psi\rangle = \epsilon_{\ i}|\psi\rangle, \tag{3.2.12}$$

with

$$V_{eff}(\mathbf{r}) = v_{ext}(\mathbf{r}) + v_H(\mathbf{r}) + v_{xc}(\mathbf{r}), \tag{3.2.13}$$

where

$$v_H(\mathbf{r}) = \frac{\delta \; \mathcal{E}_H[n]}{\delta \; n(\mathbf{r})} \tag{3.2.14}$$

and

$$v_{xc}(\mathbf{r}) = \frac{\delta \; \mathcal{E}_{xc}[n]}{\delta \; n(\mathbf{r})}. \tag{3.2.15}$$

These equations, called *Kohn-Sham equations* (KS), are high non-linear equations, because the unknown quantities $|\psi\rangle$ appear also in the efficient potential, through the density, and they are solved iteratively. Different from other approaches (only

apparearing similar), they allow to reduce *exactly* a many-body problem to a one-particle problem [2], once known the exchange and correlation functional. In fact, apart from relativistic effects, the treatment followed up to now is in principle exact.

3.2.2 Local Density Approximation

Unfortunately, an explicit and general functional form for the exchange and correlation functional (3.2.10) is still unknown. In order to use the formalism developed up to now, one should formulate hypothesis and approximations on the term (3.2.10). The simplest approximation used is the Local Density Approximation (LDA), which describes adequately a large number of systems. The idea of LDA is to substitute the density of exchange and correlation energy of the real system (non uniform) with the one of an homogenous electron gas with the same density. In other words, we assume that in small enough spatial regions the charge distribution of a non-homogenous electron gas behaves like in the homogenous system:

$$\mathcal{E}_{xc}[n] = \int d^3r \; \varepsilon_{xc}[n(\mathbf{r})]n(\mathbf{r}) \tag{3.2.16}$$

where $\varepsilon_{xc}[n]$ is the exchange and correlation energy per particle of a homogenous electron gas of density n. The more accurate estimation of $\varepsilon_{xc}[n]$ was obtained in 1980 through a Monte Carlo simulation by Ceperley and Alder [50] and then interpolated by Perdew and Zunger [61].

The LDA is clearly exact in the case where the density is a constant and it should

[2] Even if the form of the energy functional and of the equations (3.2.12) suggests a natural interpretation of one electron immerged in the field generated by all the other electrons, DFT is not a *mean-field* treatment of a many-body problem, like Hartree-Fock, but an exact theory. $|\psi_i\rangle$ and ϵ_i have no physical meaning, if not the one of orbitals and energetic levels of a non-interacting fictitious system. The only physical observable of the theory are the density and the ground state energy.

be adequate for slowly varying densities. As a matter of fact, LDA gives surprisingly good results for real systems [62]. Especially the ground state geometries of molecules and solids are very accurately predicted. M. Levy [63] explained this as a particularity of the Coulomb potential.

3.2.3 Beyond LDA: Gradient Corrections

Despite the success of the LDA there are also some drawbacks which prevent the extension of many computations to certain systems. For instance, the cohesive energies of solids are systematically overestimated, while lattice constants are systematically underestimated. Errors in the structural properties are usually small for systems with covalent or metallic bonds, but it is well known that the hydrogen bond cannot be described accurately within LDA [64]. Various approximations have been introduced in the course of the years to improve LDA.
Here we consider one of these possibilities, that is the inclusion of Gradient Corrections (GC) in the exchange and correlation energy (3.2.16). In a GC scheme it is assumed that the exchange-correlation functional depends locally on the density and on the density gradient:

$$\mathcal{E}_{xc}[n, \nabla n] = \int d^3r \; \varepsilon_{xc}[n(\mathbf{r}), \nabla_{\mathbf{r}} n(\mathbf{r})] n(\mathbf{r}) \tag{3.2.17}$$

Whether such GC are definitely an improvement over LDA is still under debate. In the past the years several GC functional were introduced and their properties studied. In particular the description of the hydrogen bond, which plays a very important role in the success of the calculation presented in this thesis, is well achieved using the exchange functional of Becke [65] and the correlation functional of Lee, Yang, and Parr [66] (BLYP), as discussed in Ref.[67].

3.2.4 Pseudopotentials

We will expand the Kohn-Sham wavefunctions in plane waves. However, the description of a system can require a very high cutoff because of the presence of a large variety of length scales. For this reason, we introduce here a further approximation, the use of pseudopotentials instead of the real Coulomb potential, which allows at the same time to reduce the number of degrees of freedom and the plane waves cutoff.

The fundamental observation, that allows the development of pseudopotentials theories is that the *core* electrons, strongly condensed around the nucleus, do not participate directly in chemical bonding. The nature of the chemical bond, and consequently many physical properties, are determined basically by the external part of the atoms, where only the valence electrons contribute to the electron density. This is confirmed from the fact that elements of the same group of the Periodic Table (characterized by the same valence configuration) have several common properties, even if they have different atomic numbers and different numbers of core electrons. This observation justifies the idea of an atom model with only valence electrons, that emulates the real atom.

The procedure, however, is not trivial: atoms of the same group of the Periodic Table have similar properties, but not identical; differences essentially arise from the core orbitals, which modify the structure of the valence. Core electrons, in fact, partially screen the Coulombic potential of the nucleus and, because of the fermionic nature of the electrons, push the valence charge outside the core region. Phillips and Kleinman suggested long time ago [68] the idea that core electrons and Coulombic divergence of the nuclear potential can be eliminated at the same time and their total effect can be substituted with a weak efficient potential, that acts only on the valence electrons.

The goal of the pseudopotential theory is to construct such a potential, without

divergence and rapid spacial oscillations.

After the first empirical models, a significant progress was made with the introduction of *first-principles* pseudopotentials. This type of pseudopotentials substitutes the true atom with a pseudo-atom, that reproduces well the behavior in a variety of physical and chemical situations (molecule, solid, etc.). This important property is called *transferability* and is a characteristic of the *norm-conserving* pseudopotentials [69–71]: they are named in this way because the fundamental condition in order to achieve the transferability is the conservation of the norm of the wavefunctions going from the true atom to the pseudo-atom. These pseudopotentials are non-local (i.e. they contain the projectors of the angular momentum). In spite of the complications in their use caused from the non-locality and the fact that to eliminate the core means inevitably to consider it frozen, i.e. to exclude any possible relaxation of it after the change of chemical environment (*frozen core approximation*), these pseudopotentials, born at the end of the '70, are still one of the more efficient way to solve electronic structure problems. After the seminal work of Bachelet et al. [70], increasingly efficient and convenient norm-conserving pseudopotentials were produced by several groups [72–75]. In this thesis, we use non-local potentials of separable form [72], which are computationally very convenient. Their functional form is:

$$v = v_{loc} + \sum_{\ell=1}^{\ell_{max}} |p_\ell\rangle \omega_\ell \langle p_\ell|, \tag{3.2.18}$$

where v_{loc} is a local operator, p_ℓ the projector on the ℓ angular momentum and the ω_ℓ are appropriated weights.

3.3 Molecular Dynamics

In order to describe the dynamics of complex chemical systems, static electronic structure calculations should be combined with molecular dynamics methods. In the

last fifteen years molecular dynamics (MD) have played an increasingly important role in the study of materials, thanks to the introduction of the Car-Parrinello method [3]. Before the introduction of such an *ab initio* approach, MD simulations were performed using a functional form for the interatomic forces assumed on the basis of physical considerations. Potential parameters fitted to a given experimental and/or theoretical data base[76]. The predictive power of such potentials is limited when used in regions of configuration space included in the fitted data base. It is therefore highly desiderable to have an approach in which the interatomic forces are generated in a consistent and accurate way during the simulation. In the Car-Parrinello approach the forces are calculated using the state-of-the-art electronic structure calculations based on DFT: in this way the forces are parameter-free and derived from first-principles, with no experimental input. In the following, we will illustrate briefly the conventional idea of MD and then introduce the Car Parrinello Molecular Dynamics method.

3.3.1 Conventional Molecular Dynamics technique

The starting point for the solution of the classical equation of motion for a system of N particles interacting via a potential Φ is the Lagrangian equation of the motion[77]:

$$\frac{\mathrm{d}}{\mathrm{dt}}\frac{\partial\,\mathcal{L}}{\partial\,\dot{q}_k}-\frac{\partial\,\mathcal{L}}{\partial\,q_k}=0, \qquad (k=1,...,3N) \tag{3.3.1}$$

where the Lagrangian $\mathcal{L}(\mathbf{q},\dot{\mathbf{q}})$ is a function of the generalized coordinates q_k and their time derivatives $\dot{q}_k$. Such a Lagrangian is defined in terms of kinetic and potential energies:

$$\mathcal{L}=T-\Phi. \tag{3.3.2}$$

If we consider now a system of atoms, with Cartesian coordinates $\mathbf{R}_I$ and mass M_I, then the kinetic energy reads:

$$T = \sum_{I=1}^{N} \frac{1}{2} M_I \dot{\mathbf{R}}_I^2 \tag{3.3.3}$$

and the potential energy:

$$\Phi = V(\mathbf{R}_1, ..., \mathbf{R}_N). \tag{3.3.4}$$

Using these definitions, Eq.(3.3.1) becomes:

$$M_I \ddot{\mathbf{R}}_I = \mathbf{F}_I, \tag{3.3.5}$$

and

$$\mathbf{F}_I = -\nabla_{\mathbf{R}_I} V, \tag{3.3.6}$$

is the force on the atom I.

The equation of motion (3.3.5) can be integrated numerically. The simpler method of integration is the Verlet algorithm [78], which is a direct solution of Eq. (3.3.5). Following this algorithm:

$$q(t + \delta\ t) = 2q(t) - q(t - \delta\ t) + \frac{\delta\ t^2 \mathbf{F}_I(t)}{M_I}. \tag{3.3.7}$$

In this approach velocities do not appear at all. The velocities are not needed to compute the trajectories, but they are useful for estimating the kinetic energy. They may be obtained using finite differences:

$$\dot{q}(t + \delta\ t) = \frac{q(t + \delta\ t) - q(t - \delta\ t)}{2\delta\ t}. \tag{3.3.8}$$

Whereas Eq.(3.3.7) is correct to order $\delta\ t^4$ the velocities from Eq.(3.3.8) are subject to errors of order $\delta\ t^2$. In order to solve this problem several algorithm were introduced. The one used in the calculations presented in this thesis is called "velocity Verlet" [79] and reads:

$$q(t + \delta\ t) = q(t) + \delta\ t\dot{q}(t) + \frac{\delta\ t^2 \mathbf{F}_I(t)}{M_I}, \tag{3.3.9}$$

and

$$\dot{q}(t+\delta\ t) = \dot{q}(t) + \frac{1}{2M_I}\delta\ t[\mathbf{F}_I(t) + \mathbf{F}_I(t+\delta\ t)]. \tag{3.3.10}$$

The explicit treatment of the velocities not only gives a more accurate integration scheme, but also allows the integration time to be changed during the run and to control the temperature by simple velocity scaling [3,80].

3.3.2 Car Parrinello Molecular Dynamics

We consider systems for which the BO approximation holds. If this last condition is satisfied, the behavior of the coupled electron ion system can be regarded as adiabatic. As we have seen in Sec.3.1, we can assume that the motion of the atoms can be described by classical mechanics, which is justified under many circumstances.

The interaction potential among the ions is then given by:

$$\Phi(\mathbf{R}_1, ..., \mathbf{R}_N) = \langle \psi_0 | H | \psi_0 \rangle \tag{3.3.11}$$

where H is the Hamiltonian of the system for fixed ionic positions $\mathbf{R}_I$ and ψ_0 the corresponding ground state. In order to use Eq.(3.3.11) in a MD run, calculation of ψ_0 for a number of configuration of the order of 10^4 are needed. This is computationally very expensive.

In order to circumvent this problem, Car and Parrinello proposed a Lagrangian based on the KS scheme: such a Lagrangian is written down in which the electrons, represented by a set of orbitals $\{\psi_i(\mathbf{r})\}$, execute a fictitious dynamics which allows them to follow the motion of the ions, represented by a set of positions $\{\mathbf{R}_I\}$, while remaining on the instantaneous ground state BO surface. This is accomplished by keeping the fictitious kinetic energy of the ions. The interatomic forces are computed via the Hellmann-Feynman theorem from the instantaneous electronic structure corresponding to each ionic configuration.

The equation of motion for the full dynamical system, i.e. fictitious electron dynamics plus real ionic dynamics, are derived from the Lagrangian:

$$\mathcal{L} = 2\sum_{i=1}^{N_{\rm occ}} \mu \int d^3r \quad \mid \dot{\psi}_i(\mathbf{r},t) \mid^2 + \sum_{I=1}^{N} \frac{1}{2} M_I \ \dot{\mathbf{R}}_I^2 - \mathcal{E}[\{\psi_i\},\{\mathbf{R}_I\}]$$
$$+2\sum_{ij} \Lambda_{ij} \ \left[\int d^3r \ \ \psi_i^*(\mathbf{r},t) \ \psi_j(\mathbf{r},t) - \delta_{\ ij} \right] \tag{3.3.12}$$

where $\mathcal{E}[\{\psi_i\},\{\mathbf{R}_I\}]$ is the KS functional and Λ_{ij} is a set of Lagrange multipliers which ensure that the orthonormality constraints

$$\int d^3r \ \psi_i^*(\mathbf{r})\psi_j(\mathbf{r}) = \delta_{\ ij} \tag{3.3.13}$$

are satisfied. M_I are the physical ionic masses and μ is an arbitrary parameter of appropriate units. N_{occ} is the number of occupied electronic states and we assume that all of them are completely occupied ($f_i = 2$,$i = 1, N_{occ}$). In Eq. (3.3.12) we have two classical kinetic energy terms: $K_e = 2\sum_{i=1}^{N_{\rm occ}} \int d^3r \ \ \mu \mid \dot{\psi}_i(\mathbf{r},t) \mid^2$, associated with the electronic parameters $\psi$and $K_I = \sum_{I=1}^{N} \frac{1}{2} M_I \ \dot{\mathbf{R}}_I^2$ associated with the nuclear coordinates. K_e and K_I measure the rate of variation of the respective degrees of freedom in the coupled electron-ion parameter space. The Car-Parrinello Lagrangian generates a dynamics for the parameters ψ_i and $\mathbf{R}_I$ through the equations of motion:

$$\mu\ddot{\psi}_i(\mathbf{r},t) = -\frac{1}{2} \ \frac{\delta \ \mathcal{E}}{\delta \ \psi_i^*(\mathbf{r},t)} + \sum_j \Lambda_{ij}\psi_j(\mathbf{r},t) \tag{3.3.14}$$

$$M_I\ddot{\mathbf{R}}_I = -\frac{\partial \, \mathcal{E}}{\partial \, \mathbf{R}_I(t)} \, . \tag{3.3.15}$$

These equations allow the sampling of the complex parameter space of ψ_i and $\mathbf{R}_I$ with the MD techniques used in statistical mechanics simulations [76]. At the first glance there is no relation between the ionic dynamics generated with Eq. (3.3.15) and the correct classical dynamical equation for the nuclei given by

$$M_I\ddot{\mathbf{R}}_I = -\frac{\partial \, \Phi}{\partial \, \mathbf{R}_I(t)} \tag{3.3.16}$$

where

$$\Phi(\{\mathbf{R}_I\}) = \min_{\psi} \mathcal{E}[\{\psi\}, \{\mathbf{R}_I\}] \tag{3.3.17}$$

which implies:

$$\left.\frac{\delta\ \mathcal{E}}{\delta\ \psi_i^*(\mathbf{r}, t)}\right|_{E_o} = 0\ . \tag{3.3.18}$$

Indeed, the nuclear trajectories generated by Eq. (3.3.15) and those obtained by (3.3.16) generally do not coincide, unless $\mathcal{E}[\{\psi\}, \{\mathbf{R}_I\}]$ is at the instantaneous minimum. However, the parameter μ and the initial conditions $\{\psi(t = 0)\}$ and $\{\mathbf{R}_I(t = 0)\}$ can be chosen such that the time scale for the electronic degrees of freedom is much shorter than that of the nuclei. In this case the nuclear trajectories, initially lying on the BO surface, will deviate from it only after times that are significantly longer than the MD time step. In other words, the two sets of degrees of freedom, ions and electrons, are only weakly coupled, the transfer of energy between them is small enough to allow the electrons to follow adiabatically the ionic motion, remaining close to their instantaneous BO surface.

Chapter 4

Modern theory of Polarization

Raman scattering in the zero frequency limit, i.e. in the case in which the incoming radiation cannot induce a transition to excited electronic states, is related, as we will discuss in detail in Sec. 6.2, to the fluctuation of the polarizability tensor.
The approach used in this thesis to calculate the polarizability tensor is perturbation theory. In fact, the polarizability is simply related to the answer of the system to an electric field which couples with the polarization. Therefore, in this chapter we digress from our principal topic and discuss the modern theory of polarization.

4.1 Introduction

The dipole moment of any finite N-electron system in its ground state is a simple and well defined quantity. Given the many-body wavefunction Ψ and the corresponding single-particle electron density $n(\mathbf{r})$ the electronic contribution to the dipole is[19]:

$$\langle \sum_{i=1}^{N} \mathbf{r}_i \rangle = \int d^3r \;\; \mathbf{r}\; n(\mathbf{r}) = \langle \Psi | \sum_{i=1}^{N} \mathbf{r}_i | \Psi \rangle. \tag{4.1.1}$$

This looks trivial, but we are implicitly using an essential fact: the ground state wavefunction of any finite system is square-integrable and vanishes exponentially at

infinity; the density decays exponentially as well.
However, the microscopic definition of this same quantity is surprisingly difficult in the limit of an infinite system. In fact, in a macroscopic solid, the macroscopic polarization is ideally defined as the dipole of the macroscopic sample divided by its volume. The integral in Eq.(4.1.1) is then dominated by what happens at the surface of the sample. One can imagine overcoming this problem by evaluating the polarization for larger and larger volumes of the sample, until it converges to its bulk value. However, in practice, the procedure is computationally impossible to carry out.

The usual way to avoid these undesired surface effects is to adopt periodic boundary conditions. Unfortunately, this does not solve the polarization problem. In fact, a description, found in many textbooks [21–23], à la Clausius-Mossotti, in terms of a model consisting of discrete and well separated dipoles is inadequate because the electronic distribution of a real dielectric is continuous and often delocalized. So, in this model the dipole moment of a unit cell depends on the choice of the cell. Furthermore, the dipole of a periodic system cannot be evaluated via Eq.(4.1.1): the integrals are ill-defined due to the unbounded nature of the quantum-mechanical position operator.

For these reasons macroscopic polarization remained a major challenge for many years. In 1992 there was a breakthrough. Macroscopic polarization was defined in terms of wavefunction phases, instead of the charge. This definition has an unambiguous thermodynamic limit and therefore periodic boundary conditions can be used. In the following years a modern theory of macroscopic polarization in crystalline dielectrics was completely established, thanks to the work of R.D. King-Smith and D. Vanderbilt [9], who expressed polarization in terms of a Berry phase[24]. In the following sections, we will introduce the concept of Berry phase and provide a

short description of the modern theory of polarization.

4.2 Berry phase

The Berry phase is a very general concept, having observable manifestations in several different areas of physics[24]. One starts with the most generic quantum Hamiltonian having a parametric dependence:

$$H(\xi)|\psi(\xi)\rangle = E(\xi)|\psi(\xi)\rangle \tag{4.2.1}$$

where ξ is defined in a suitable domain. In the original Berry paper [24] $H(\xi)$ is the electronic Hamiltonian of a molecule within the BO approximation and ξ is a nuclear coordinate. However the theory is quite general and applies to the most disparate parametric dependence. We assume that $\psi(\xi)$ is the ground state, non-degenerate for any ξ. The phase difference $\Delta\phi_{12}$ between the ground states at two different ξ points is defined by:

$$\mathrm{e}^{-i\Delta\phi_{12}} = \frac{\langle\psi(\xi_1)|\psi(\xi_2)\rangle}{|\langle\psi(\xi_1)|\psi(\xi_2)\rangle|} \tag{4.2.2}$$

$$\Delta\phi_{12} = -\mathrm{Im}\log\langle\psi(\xi_1)|\psi(\xi_2)\rangle \tag{4.2.3}$$

This phase should not have any physical meaning. In fact, any quantum mechanical state vector is arbitrary by a constant phase factor (each phase defines a different gauge). Despite this, when one considers the total phase difference γ along a closed path:

$$\begin{aligned}\gamma = \Delta\phi_{12} + \Delta\phi_{23} + \Delta\phi_{34} + \Delta\phi_{41} = \\ -\mathrm{Im}\ \log\langle\psi(\xi_1)|\psi(\xi_2)\rangle\langle\psi(\xi_2)|\psi(\xi_3)\rangle\langle\psi(\xi_3)|\psi(\xi_4)\rangle\langle\psi(\xi_4)|\psi(\xi_1)\rangle\end{aligned} \tag{4.2.4}$$

one immediately realizes that the phase difference is gauge invariant, since all the gauge-arbitrary phases cancel in pairs. The above simple-minded algebra leads to

a result of physical importance: in fact, a gauge-invariant quantity is potentially a physical observable.

Traditionally, one is accustomed to regard any observable effect in quantum mechanics as the eigenvalue of some operator.

The main message of the paper of Berry [24] can be illustrated by saying that there are also observable effects of a completely different nature: γ cannot be expressed in term of the eigenvalues of any operator, i.e. in terms of a Hamiltonian. One of the innovations in this thesis, as it is described in the next chapter, is the extention of the variational perturbation theory, usually destinated to perturbations described in a Hamiltonian form, to non-Hamiltonian perturbations in order to be able to treat an electric field that couples with the polarization, expressed as a Berry phase.

4.3 One electron case

Now we can come back to the problem of the position operator by examining the one-dimensional case. Adopting a given choice for the boundary conditions is equivalent to defining the Hilbert space where our solutions of Schrödinger's equation live. For a single–particle wavefunction the periodic boundary condition reads $\psi(x + L) = \psi(x)$, where L is the imposed periodicity, chosen to be large with respect to atomic dimensions. Notice that lattice periodicity is not assumed, and the theory applies to disordered systems as well.

By definition, an operator maps any vector of the given Hilbert space into another vector belonging to the same space. Therefore, the multiplicative position operator x is not a legitimate operator when periodic boundary conditions are adopted for the state vectors, since $x\,\psi(x)$ is not a periodic function whenever $\psi(x)$ is. It is then obvious why Eq.(4.1.1) cannot be used in condensed matter theory. Of course, any periodic function of x is a legitimate multiplicative operator in the Hilbert space.

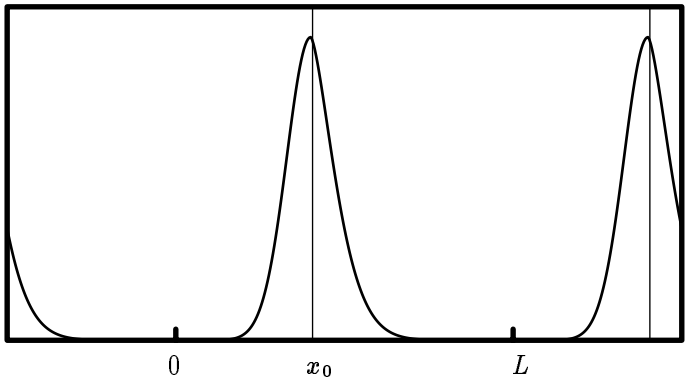

Figure 4.3.1: *The distribution $|\psi(x)|^2$ of a single–particle orbital within periodic Born-von-Kàrmàn boundary conditions. This picture is taken from Ref.[16].*

Before switching to the polarization problem, it is useful to discuss an important precursor study, apparently unrelated to the polarization problem, where however the expectation value of the position operator plays a key role.

Some years ago, A. Selloni et al. [81] addressed the properties of electrons dissolved in molten salts at high dilution. The physical problem was studied by means of a mixed quantum–classical simulation, where a lone electron was adiabatically moving in a molten salt at finite temperature. The simulation cell contained 32 cations, 31 anions, and a single electron. KCl was the original case study. The electronic wavefunction was chosen to obey periodic boundary conditions over the simulation cell, and therefore features periodic replicas as well. A plot of such an electronic distribution, in a schematic one–dimensional analogue, is given in Fig.4.3.1.

One of the main properties investigated in Ref. [81] was the electronic diffusion. In order to perform this study, one has to first identify where the "center" of the

electronic distribution is. Intuitively, the distribution in Fig.4.3.1 appears to have a "center", which however is defined only modulo the replica periodicity, and furthermore cannot be evaluated simply as in Eq.(4.1.1),i.e. $\langle x\rangle = \int dx\, x|\psi(x)|^2$. Selloni et al. solved the problem by means of a very elegant formula, presented below. In fact according to Refs. [14,17,81,82], the key quantity for dealing with the position operator within periodic boundary conditions is the dimensionless complex number $\mathfrak{z}$, defined as:

$$\mathfrak{z} = \langle\psi|e^{i\frac{2\pi}{L}x}|\psi\rangle = \int_0^L dx\, e^{i\frac{2\pi}{L}x}|\psi(x)|^2, \tag{4.3.1}$$

whose modulus is no larger than 1. The most general electron density, such as the one depicted in Fig. 4.3.1, can always be written as a superposition of a function $n_{\rm loc}(x)$, normalized over $(-\infty,\infty)$, and of its periodic replicas:

$$|\psi(x)|^2 = \sum_{m=-\infty}^{\infty} n_{\rm loc}(x - x_0 - mL). \tag{4.3.2}$$

Both x_0 and $n_{\rm loc}(x)$ have a large arbitrariness: we restrict it imposing that x_0 is the center of the distribution, in the sense that $\int_{-\infty}^{\infty} dx\, x\, n_{\rm loc}(x) = 0$. Using Eq. (4.3.2), $\mathfrak{z}$ can be expressed in terms of the Fourier transform of $n_{\rm loc}$ as:

$$\mathfrak{z} = e^{i\frac{2\pi}{L}x_0}\tilde{n}_{\rm loc}(-\frac{2\pi}{L}). \tag{4.3.3}$$

If the electron is localized in a region of space much smaller than L, its Fourier transform is smooth over reciprocal distances on the order of L^{-1} and can be expanded as:

$$\tilde{n}_{\rm loc}(-\frac{2\pi}{L}) = 1 - \frac{1}{2}\left(\frac{2\pi}{L}\right)^2 \int_{-\infty}^{\infty} dx\, x^2 n_{\rm loc}(x) + \mathcal{O}(L^{-3}). \tag{4.3.4}$$

A very natural definition of the center of a localized periodic distribution $|\psi(x)|^2$ is therefore provided by the phase of $\mathfrak{z}$ as:

$$\langle x\rangle = \frac{L}{2\pi}\text{Im log } \mathfrak{z} = \frac{L}{2\pi}\text{Im log } \langle\psi|e^{i\frac{2\pi}{L}x}|\psi\rangle, \tag{4.3.5}$$

which is in fact the formula first proposed by Selloni et al. [81,82]. The expectation value $\langle x\rangle$ is defined as modulo L, as expected since $|\psi(x)|^2$ is periodic.

The above expressions imply $\langle x \rangle \simeq x_0 \bmod L$; in the special case where $n_{\rm loc}(x)$ can be taken as an even function, its Fourier transform is real and Eq.(4.3.3) indeed yields $\langle x \rangle \equiv x_0 \bmod L$. In the case of extreme delocalization we have instead $|\psi(x)|^2 = 1/L$ and $\mathfrak{z} = 0$: hence the center of the distribution $\langle x \rangle$, according to Eq.(4.3.5), is ill–defined. For a more general delocalized state, we expect that $\mathfrak{z}$ goes to zero at large L [17].

We have therefore arrived at a definition of $\langle x \rangle$ within periodic boundary conditions which has many of the desirable features we were looking for: nonetheless, there is a property that is even more important and which we are going to demonstrate now. Suppose the potential which the electron moves in has a slow time dependence and we wish to follow the adiabatic evolution of the electronic state $|\psi\rangle$. If we call $|\psi_j\rangle$ the instantaneous eigenstates at time t, the lowest order adiabatic evolution of the ground–state density matrix is [83]:

$$|\psi\rangle\langle\psi| \simeq |\psi_0\rangle\langle\psi_0| + i \sum_{j \neq 0} \left(|\psi_j\rangle \frac{\langle \psi_j | \dot{\psi}_0 \rangle}{\epsilon_j - \epsilon_0} \langle \psi_0 | - \mathrm{Hc} \right) \quad , \tag{4.3.6}$$

where the phases have been chosen in order to make $|\psi_0\rangle$ orthogonal to its time derivative $|\dot{\psi}_0\rangle$. The macroscopic electrical current flowing through the system at time t is therefore:

$$\langle j \rangle = -\frac{1}{L} \langle \psi | p | \psi \rangle \simeq -\frac{i}{L} \sum_{j \neq 0} \frac{\langle \psi_0 | p | \psi_j \rangle \langle \psi_j | \dot{\psi}_0 \rangle}{\epsilon_j - \epsilon_0} + \mathrm{cc.} \tag{4.3.7}$$

It is then rather straightforward to prove that $\langle j \rangle$ to lowest order in $1/L$ equals $-(1/L)\, d\langle x \rangle / dt$, where $\langle x \rangle$ is evaluated using in Eq. (4.3.5) the instantaneous ground eigenstate:

$$\langle j \rangle \simeq -\frac{1}{2\pi} \mathrm{Im}\, \frac{d}{dt} \log \langle \psi_0 | e^{i \frac{2\pi}{L} x} | \psi_0 \rangle . \tag{4.3.8}$$

This finding proves the value of Eqs. (4.3.1) and (4.3.5) in studying electron transport [81,82].

4.4 Many electrons case

The formulas presented in the previous chapter can be extended to the case of N electrons in a segment of length L, where the thermodynamic limit is taken: $L \to \infty$, $N \to \infty$, and $N/L = n_0$ constant. We assume that the ground state is nondegenerate, and we deal with insulating systems only: this means that the gap between the ground eigenvalue and the excited ones remains finite for $L \to \infty$.

We start defining the one–dimensional analogue of $\hat{\mathbf{R}}$, namely, the multiplicative operator $\hat{X} = \sum_{i=1}^{N} x_i$, and the complex number

$$\mathfrak{z}_N = \langle \Psi | \mathrm{e}^{i\frac{2\pi}{L}\hat{X}} | \Psi \rangle. \tag{4.4.1}$$

It is obvious that the operator $\hat{X}$ is ill–defined in our Hilbert space, while its complex exponential appearing in Eq. (4.4.1) is well defined. The main result of Ref. [14] is that the ground–state expectation value of the position operator is given by the analogue of Eq. (4.3.5), namely:

$$\langle X \rangle = \frac{L}{2\pi} \mathrm{Im} \log \mathfrak{z}_N, \tag{4.4.2}$$

a quantity defined modulo L as above.

The right–hand side of Eq. (4.4.2) is not simply the expectation value of an operator: the given form, as the imaginary part of a logarithm, is indeed essential. Furthermore, its main ingredient is the expectation value of the multiplicative operator $\mathrm{e}^{i\frac{2\pi}{L}\hat{X}}$: it is important to realize that this is a genuine *many–body* operator.

We now focus on an uncorrelated system of independent electrons, whose N-electron wavefunction $|\Psi\rangle$ is a Slater determinant. In this case the expectation value $\langle X \rangle$, Eq. (4.4.2), is uniquely determined by the one-body density matrix. However, the formulation is simpler when expressing $\langle X \rangle$ and the resulting polarization P directly in terms of the orbitals. We define

$$|\tilde{\Psi}\rangle = \mathrm{e}^{i\frac{2\pi}{L}\hat{X}} |\Psi\rangle : \tag{4.4.3}$$

$|\tilde{\Psi}\rangle$ is indeed a Slater determinant, where each orbital $\psi(x)$ of $|\Psi\rangle$ is multiplied by the plane wave $e^{i\frac{2\pi}{L}x}$. According to a well known theorem, the overlap amongst two determinants is equal to the determinant of the overlap matrix amongst the orbitals. We therefore define the matrix:

$$S_{ij} = \langle\psi_i|e^{i\frac{2\pi}{L}x}|\psi_j\rangle = \int_0^L dx\, \psi_i^*(x)e^{i\frac{2\pi}{L}x}\psi_j(x), \tag{4.4.4}$$

in terms of which we easily get

$$X = \frac{L}{2\pi}\mathrm{Im}\log\langle\Psi|\tilde{\Psi}\rangle = \frac{L}{\pi}\mathrm{Im}\log\det S, \tag{4.4.5}$$

where the factor of 2 accounts for double spin occupancy, and the expression becomes accurate in the limit of a large system.

The expression of Eq. (4.4.5) is known as the "single–point Berry phase" and was first proposed by R. Resta in a volume of lecture notes [18]. Since then, its three-dimensional generalization has been used in a series of DFT calculations for non-crystalline systems [85].

The case of a crystalline system of independent electrons is the problem which historically has been solved first [7–9], though along a very different logical path [10–13] than adopted here. The formalism adopted here leads to the same results.

4.5 Macroscopic polarization

We are now able to describe properly the electric polarization $\mathbf{P}^{ele} = e\langle\mathbf{r}\rangle$ in a periodic system.

We can, in fact, generalize Eq.(4.4.2) to the three-dimensional case and define the Berry phase γ_μ [8–10,14]:

$$\gamma_\mu = \mathrm{Im}\log\det\mathbf{Q}^{(\mu)}, \tag{4.5.1}$$

where the matrix $\mathbf{Q}^{(\mu)}$ is defined as $\mathbf{Q}^{(\mu)}_{i,j} = \left\langle\psi_i\left|e^{i\mathbf{G}_\mu\cdot\mathbf{r}}\right|\psi_j\right\rangle$, $\mathbf{G}_\mu$ is the smallest vector

in a periodically repeated cubic cell in the direction μ. Eq.(4.5.1) can be generalized to cells of arbitrary shape, as is explained in Appendix A.

Eq.(4.5.1) is, in principle, valid in the limit of an infinite dimension of the cell, but in a non conducting material this is a good approximation even with relatively small supercells.

P_μ^{ele} is then given by:

$$P_\mu^{ele} = \frac{2\,|e|}{|G_\mu|}\gamma_\mu, \tag{4.5.2}$$

which is defined modulo $2\pi G_\mu$. We underline that Eq.(4.5.1), and consequently Eq.(4.5.2), cannot be expressed in terms of a Hamiltonian[1]. In order to deal with such an observable we will generalize variational density functional perturbation theory, which was formulated [6] for Hamiltonian perturbations to the non-Hamiltonian case.

[1]Only very recently J. Zak [84] has suggested that this property, which holds for the Berry phase, not necessarily is applicable to the geometric phase in the band structure of solids. Following Ref.[84] it seems that it is possible to cast $\langle x \rangle$ in the form of an expectation value of a well defined Hermitian operator.

Chapter 5

Variational perturbation theory

In order to calculate the polarizability, which is the basic ingredient for the calculation of the Raman scattering intensities in the zero frequency limit, we need the linear answer to a small applied electric field. For this reason, we introduce in this Chapter the tools of variational density functional pertubation theory.

5.1 Generalized variational density functional perturbation theory

The outcome of many experiments measures the way in which a physical system reacts to the application of a small applied external field. If the external field is time independent, one can relate the measured response to second order derivative of the total energy relative to appropriate fields. This is the case for instance of the electric polarizability or of the bulk modulus, which can be expressed as the second derivative of the energy relative to the external electric field and the volume respectively. Given the relevance of this class of properties, a large number of methods has been devised to calculate static linear responses, and has been implemented in the context of

many approximated electron structure theories like Hartree Fock, density functional theory [86], Møller-Plesset perturbation theory[87] or coupled clusters[88]. Here we shall focus on methods that can be applied within the density functional theory (DFT)[89] and although our approach is fairly general, we shall present applications based on the plane wave (PW) pseudopotential scheme.

The simplest way to evaluate the response functions is to calculate the energy for various values of the applied field and extract numerically the energy derivatives. This procedure can work reasonably well, but it requires several evaluations of the total energy and the numerical derivative introduces errors. A more satisfactory approach is to evaluate directly the response functions, making use of perturbation theory. This leads for the static response functions to the familiar expression of the response function in terms of a double sum over the occupied and empty electronic states. This approach has been reformulated in the context of DFT by Baroni et al.[4] and successfully applied to many problems. An essential ingredient for the success of this approach has been the use of the Sternheimer method [5] which avoids the explicit evaluation of the poorly convergent double sum and together with a good preconditioner leads to an efficient algorithm.

More recently Gonze et al. [6] have shown that if one perturbs the Hamiltonian with an external field, the induced variation in the Kohn-Sham orbitals can be obtained to all perturbative orders from a variational formulation. Use of the $2n + 1$ theorem[20] allows then to calculate the change in energy and the corresponding energy derivatives. For instance the second order energy derivatives can be calculated once the first order variation in the Kohn-Sham orbitals are known. One advantage this theory has in common with the Sternheimer approach is that it avoids the need to perform explicitly the double summation. The efficiency of the variational density functional perturbation approach is comparable to that of Baroni et al.[4].

Gonze approach as well as the more standard perturbation theory is based on a

Hamiltonian formulation. The purpose of this thesis is to generalize the Gonze variational approach to the case in which the perturbation cannot be expressed in a Hamiltonian form. The need to treat such a term arises when for instance one wants to evaluate the effect of an electric field that couples with the polarization in a periodic system. As we have discuss in Chap.4, modern theories express the polarization in terms of a Berry phase[9,10], which is not expressible in Hamiltonian terms. Furthermore, while conventional perturbation theory must be formulated in terms of Kohn-Sham eigenstates, there is some time we need to work with other orbitals. A case in point is for istance the calculation of NMR chemical shifts which can profit from the use of maximally localized orbitals[25,26].

The derivation of this thesis is very close to the spirit of DFT and in our opinion slightly more transparent than that of Gonze[6]. Of course our formulae reduce to those of Gonze in the case of Hamiltonian perturbations. In the following we will introduce the new approach and we will also address some technical problems, like the handling of the gradient corrections or the choice of appropriate preconditioners. We will illustrate the performance of the method for the calculation of the vibrational frequencies, polarizability, and Raman intensities.

5.2 Theory

In standard perturbation theory [6], a small perturbation operator λh is added to the Hamiltonian H of a system and its action evaluated. We propose a conceptually different approach, using the variational principle in the framework of DFT.

Let us consider the Kohn-Sham (KS) density functional $\mathcal{E}\left[\{|\psi\rangle\}\right]$.
We work with the formulation of the Kohn-Sham functional in terms of nonorthogonal orbitals[90]. This can be realised by writing $\mathcal{E}$ in term of the density matrix

$\rho\left(\mathbf{r},\mathbf{r}'\right)$ [90,91]:

$$\mathcal{E}[\rho\left(\mathbf{r},\mathbf{r}'\right)]=-\frac{1}{2}\int d^3r\ \int d^3r\,'\delta\ \left(\mathbf{r}-\mathbf{r}'\right)\nabla^2_{\mathbf{r}}\rho\left(\mathbf{r},\mathbf{r}'\right) +\frac{1}{2}\int d^3r\ \int d^3r\,'\frac{|\rho\left(\mathbf{r},\mathbf{r}'\right)|^2}{|\mathbf{r}-\mathbf{r}'|}+\mathcal{E}_{xc}[\rho\,]+\mathcal{E}_{ext}[\rho\,] \tag{5.2.1}$$

and expressing

$$\rho\left(\mathbf{r},\mathbf{r}'\right)=\sum_{i,j}=\psi^*_i(\mathbf{r})S^{-1}_{ij}\psi_j(\mathbf{r}') \tag{5.2.2}$$

where S^{-1}_{ij} is the inverse of the overlap matrix $S_{ij}=\langle\psi_i|\psi_j\rangle$. The minimum of this functional is $\mathcal{E}^{(0)}\left[\left\{|\psi^{(0)}_i\rangle\right\}\right]=E^{(0)}$, where we assume that (at the minimum) the orbitals are orthogonal, $\langle\psi^{(0)}_i|\psi^{(0)}_j\rangle=\delta_{\ i,j}$.

Starting from $\mathcal{E}\left[\{|\psi_i\rangle\}\right]$ we add a perturbation functional of arbitrary form $\mathcal{E}^{pert}\left[\{|\psi_i\rangle\}\right]$ multiplied by λ, a small perturbative parameter. This is meant to represent the interaction with a static, but otherwise arbitrarily complex external field.

The total functional $\mathcal{E}^{tot}\left[\{|\psi_i\rangle\}\right]=\mathcal{E}^{(0)}\left[\{|\psi_i\rangle\}\right]+\lambda\mathcal{E}^{pert}\left[\{|\psi_i\rangle\}\right]$ will have a minimum which we shall expand pertubatively

$$E=E^{(0)}+\lambda E^{(1)}+\lambda^2E^{(2)}... \tag{5.2.3}$$

Similarly the KS orbitals that minimise $\mathcal{E}^{tot}$ can be expanded in λ:

$$\psi_i=\psi^{(0)}_i+\lambda\psi^{(1)}_i+\lambda^2\psi^{(2)}_i+... \tag{5.2.4}$$

To the first order the charge density reads:

$$n(\mathbf{r})=n^{(0)}(\mathbf{r})+\lambda n^{(1)}(\mathbf{r})+... \tag{5.2.5}$$

where

$$n^{(1)}\left(\mathbf{r}\right)=\sum_{i=1}^{N}\left(\psi^{(0)*}_i\left(\mathbf{r}\right)\psi^{(1)}_i\left(\mathbf{r}\right)+\psi^{(1)*}_i\left(\mathbf{r}\right)\psi^{(0)}_i\left(\mathbf{r}\right)\right) \tag{5.2.6}$$

In order to find perturbatively the minimum of $\mathcal{E}^{tot}$

$$\mathcal{E}^{tot} = \mathcal{E}^{(0)}_{KS}\left[\left\{|\psi^{(0)}_i\rangle + \lambda|\psi^{(1)}_i\rangle + ...\right\}\ \right] + \lambda\mathcal{E}^{pert}\left[\left\{|\psi^{(0)}_i\rangle + \lambda|\psi^{(1)}_i\rangle + ...\right\}\ \right] \quad (5.2.7)$$

we functionally expand $\mathcal{E}^{tot}$ to the quadratic order:

$$\begin{aligned}
\mathcal{E}^{tot} &= \mathcal{E}^{(0)}_{KS}\left[\left\{|\psi^{(0)}_i\rangle\right\}\ \right] + \lambda\mathcal{E}^{pert}\left[\left\{|\psi^{(0)}_i\rangle\right\}\ \right] \\
&+ \quad \frac{1}{2}\lambda^2 \sum_{i,j=1,N}\left\{ \langle\psi^{(1)}_i|\langle\psi^{(1)}_j| \frac{\delta\ ^2\mathcal{E}^{(0)}}{\delta\ \langle\psi^{(0)}_i|\delta\ \langle\psi^{(0)}_j|} + \langle\psi^{(1)}_j| \frac{\delta\ ^2\mathcal{E}^{(0)}}{\delta\ \langle\psi^{(0)}_j|\delta\ |\psi^{(0)}_i\rangle} |\psi^{(1)}_i\rangle \right. \\
&+ \quad \left. \langle\psi^{(1)}_i| \frac{\delta\ ^2\mathcal{E}^{(0)}}{\delta\ |\psi^{(0)}_j\rangle\delta\ \langle\psi^{(0)}_i|} |\psi^{(1)}_j\rangle + \frac{\delta\ ^2\mathcal{E}^{(0)}}{\delta\ |\psi^{(0)}_i\rangle\delta\ |\psi^{(0)}_j\rangle} |\psi^{(1)}_i\rangle|\psi^{(1)}_j\rangle \right\} \\
&+ \quad \lambda^2 \sum_{i=1,N}\left\{ \langle\psi^{(1)}_i| \frac{\delta\ \mathcal{E}^{pert}}{\delta\ \langle\psi^{(0)}_i|} + \frac{\delta\ \mathcal{E}^{pert}}{\delta\ |\psi^{(0)}_i\rangle} |\psi^{(1)}_i\rangle \right\}\ + O(\lambda^3),
\end{aligned} \quad (5.2.8)$$

where we have used the fact that

$$\frac{\delta\ \mathcal{E}^{(0)}}{\delta\ \langle\psi^{(0)}_i|} = 0 \quad (5.2.9)$$

and a similar relation for the ket derivative. The evaluation of the second order functional derivatives $\delta\ ^2\mathcal{E}^{(0)}/\ \delta\ \langle\psi^{(0)}_i|\delta\ \langle\psi^{(0)}_j|$,$\delta\ ^2\mathcal{E}^{(0)}/\ \delta\ \langle\psi^{(0)}_i|\delta\ |\psi^{(0)}_j\rangle$ and $\delta\ ^2\mathcal{E}^{(0)}/\ \delta\ |\psi^{(0)}_i\rangle\delta\ |\psi^{(0)}_j\rangle$ produces a very complicated expression, that simplifies considerably in the limit of orthogonal orbitals $S_{ij} = \delta\ _{ij}$. This leads to the expression:

$$\begin{aligned}
\mathcal{E}^{(2)} &= \frac{1}{2}\int d^3r \int d^3r\ ' n^{(1)}(\mathbf{r})\ K(\mathbf{r},\mathbf{r}') n^{(1)}(\mathbf{r}') \\
&+ \sum_{i,j=1,N} \langle\psi^{(1)}_i|\left(H^{(0)}\delta\ _{ij} - \langle\psi^{(0)}_j|H^{(0)}_{KS}|\psi^{(0)}_i\rangle\right)\ |\psi^{(1)}_j\rangle + \\
&+ \sum_{i=1,N} \langle\psi^{(1)}_i| \frac{\delta\ \mathcal{E}^{pert}}{\delta\ \langle\psi^{(0)}_i|} + \frac{\delta\ \mathcal{E}^{pert}}{\delta\ |\psi^{(0)}_i\rangle} |\psi^{(1)}_i\rangle
\end{aligned} \quad (5.2.10)$$

where

$$H^{(0)} = -\frac{1}{2}\nabla^2 + V_{ext}(\mathbf{r}) + V_H(\mathbf{r}) + V_{xc}(\mathbf{r}) \quad (5.2.11)$$

and

$$K(\mathbf{r},\mathbf{r}') = \frac{\delta\ (V_H(\mathbf{r}) + V_{xc}(\mathbf{r}))}{\delta\ n(\mathbf{r}')} \quad (5.2.12)$$

supplemented by the orthogonality constraint which to first order on λ reads:

$$\langle \psi_i^{(0)} \, | \psi_j^{(1)} \, \rangle + \langle \psi_i^{(1)} \, | \psi_j^{(0)} \, \rangle = 0 \qquad \forall i,j \tag{5.2.13}$$

For canonical orbitals:

$$\langle \psi_j^{(0)} | H^{(0)} | \psi_i^{(0)} \rangle = \epsilon \, {}_i^{(0)} \delta \, {}_{ij} \tag{5.2.14}$$

and Eq.(5.2.10) further simplifies to:

$$\mathcal{E}^{(2)} = \frac{1}{2} \int d^3r \int d^3r' n^{(1)}(\mathbf{r}) \, K(\mathbf{r},\mathbf{r}') n^{(1)}(\mathbf{r}') + \sum_{i=1,N} \langle \psi_i^{(1)} | \left(H^{(0)} - \epsilon \, {}_i^{(0)} \right) | \psi_i^{(1)} \rangle + \\ + \sum_{i=1,N} \langle \psi_i^{(1)} | \frac{\delta \, \mathcal{E}^{pert}}{\delta \, \langle \psi_i^{(0)}|} + \frac{\delta \, \mathcal{E}^{pert}}{\delta \, |\psi_i^{(0)}\rangle} | \psi_i^{(1)} \rangle \tag{5.2.15}$$

which reduces to the form proposed by Gonze[6] if

$$\mathcal{E}^{pert} = \sum_i \langle \psi_i | h | \psi_i \rangle. \tag{5.2.16}$$

5.2.1 Minimization techniques

As discussed in Ref. [6] in an appropriated choice of the gauge, we can replace Eq.(5.2.13) with the more stringent

$$\langle \psi_j^{(0)} \, | \psi_i^{(1)} \, \rangle = 0 \qquad \forall i,j \tag{5.2.17}$$

which implies orthogonalise the $\{\psi^{(1)}\}$ to the manifold of the $\{\psi^{(0)}\}$. This constraint can be imposed via a Lagrange multiplier: to this effect we introduce the following Lagrangian

$$\mathcal{L}^{(2)} = \mathcal{E}^{(2)} - \sum_{i,j} \langle \psi_i^{(1)} \, | \psi_j^{(0)} \, \rangle \Lambda_{ji}^{(1)}, \tag{5.2.18}$$

where $\Lambda_{ij}^{(1)}$ is

$$\Lambda_{ij}^{(1)} = \langle \psi_i^{(1)} \, | (H^{(0)} - \varepsilon_i^{(0)}) | \psi_j^{(0)} \, \rangle + \langle \psi_i^{(0)} \, | (H^{(0)} - \varepsilon_j^{(0)}) | \psi_j^{(1)} \, \rangle + \\ \langle \psi_i^{(0)} \, | \langle \psi_j^{(0)} \, | K | \psi_j^{(1)} \, \rangle + \langle \psi_j^{(1)} \, | K | \psi_j^{(0)} \, \rangle | \psi_i^{(0)} \, \rangle + \\ \langle \psi_i^{(0)} | \frac{\delta \, \mathcal{E}^{pert}}{\delta \, \langle \psi_j^{(0)}|} + \frac{\delta \, \mathcal{E}^{pert}}{\delta \, |\psi_i^{(0)}\rangle} | \psi_j^{(0)} \rangle. \tag{5.2.19}$$

The minimum condition yields than the inhomogeneous nonlinear system for the $\{\psi_i^{(1)}\}$:

$$-\left(H^{(0)}-\varepsilon_i^{(0)}\right)|\psi_i^{(1)}\rangle \;=\mathcal{P}^e\;\left(\int d^3r\,'K(\mathbf{r},\mathbf{r}')n^{(1)}(\mathbf{r}')|\psi_i^{(0)}\rangle+\frac{\delta\;\mathcal{E}^{pert}}{\delta\;\langle\psi_j^{(0)}|}\right) \quad (5.2.20)$$

where

$$\mathcal{P}^e=1-\sum_j|\psi_j^{(0)}\rangle\langle\psi_j^{(0)}|. \quad (5.2.21)$$

Note that the right hand side still depends on $\{\psi_i^{(1)}\}$ via the perturbation density $n^{(1)}$. The nonlinearity of Eq.(5.2.20) comes from the dependence of the right-hand side on $n^{(1)}$, and becomes more transparent if we note that:

$$\int d^3r\,'K(\mathbf{r},\mathbf{r}')n^{(1)}(\mathbf{r}')=V_H^{(1)}(\mathbf{r})+V_{xc}^{(1)}(\mathbf{r}) \quad (5.2.22)$$

where $V_H^{(1)}$ and $V_{xc}^{(1)}$ are the variations of the Hartree and exchange-correlation potentials induced by the change in the density. In term of this two contribution Eq.(5.2.20) becomes

$$-\left(H^{(0)}-\varepsilon_i^{(0)}\right)|\psi_i^{(1)}\rangle \;=\mathcal{P}^e\;\left(V_H^{(1)}(\mathbf{r})|\psi_i^{(0)}\rangle+V_{xc}^{(1)}(\mathbf{r})|\psi_i^{(0)}\rangle+\frac{\delta\;\mathcal{E}^{pert}}{\delta\;\langle\psi_j^{(0)}|}\right) \quad (5.2.23)$$

Equations (5.2.18) and (5.2.23) are valid for canonical orbitals $\{\psi_i^{(0)}\}$. In principle, they are also valid for other orbitals, e.g. for localised orbitals (Wannier functions). In that case, however, the full Hamiltonian matrix elements $\langle\psi_j^{(0)}|H^{(0)}|\psi_i^{(0)}\rangle$ must be used instead of the KS-energies $\varepsilon_i^{(0)}$.

5.2.2 Exchange-correlation functionals

The term $V_{xc}^{(1)}$ is easily evaluated in the case of the LDA. However, its evaluation is more complex for GC functionals, which can be written in the form:

$$\mathcal{E}_{xc}=\int d^3r\;n(\mathbf{r})\varepsilon_{xc}\left(n(\mathbf{r}),\nabla_{\mathbf{r}}n(\mathbf{r})\right)\;. \quad (5.2.24)$$

The calculus of variations yields the following expression in terms of first and second derivatives of $n^{(1)}$[99]:

$$
\begin{aligned}
V_{xc}^{(1)}(\mathbf{r}) = & \left. \frac{\partial^{\,2}[n\varepsilon_{xc}(n,\nabla_{\mathbf{r}}n)]}{\partial\, n^2} \right|_{n=n^{(0)}(\mathbf{r})} n^{(1)}(\mathbf{r}) \\
& - \sum_{\alpha} \frac{\partial}{\partial\, \mathbf{r}_\alpha} \left[\left. \frac{\partial^{\,2}[n\varepsilon_{xc}(n,\nabla_{\mathbf{r}}n)]}{\partial\, n \partial\,(\partial_{\,\alpha} n)} \right|_{n=n^{(0)}(\mathbf{r})} \right] n^{(1)}(\mathbf{r}) \\
& - \sum_{\alpha,\beta} \frac{\partial}{\partial\, \mathbf{r}_\alpha} \left[\left. \frac{\partial^{\,2}[n\varepsilon_{xc}(n,\nabla_{\mathbf{r}}n)]}{\partial\,(\partial_{\,\alpha} n)\partial\,(\partial_{\,\beta} n)} \right|_{n=n^{(0)}(\mathbf{r})} \right] \frac{\partial\, n^{(1)}(\mathbf{r})}{\partial\, \mathbf{r}_\beta} \\
& - \sum_{\alpha,\beta} \left[\left. \frac{\partial^{\,2}[n\varepsilon_{xc}(n,\nabla_{\mathbf{r}}n)]}{\partial\,(\partial_{\,\alpha} n)\partial\,(\partial_{\,\beta} n)} \right|_{n=n^{(0)}(\mathbf{r})} \right] \frac{\partial^{\,2} n^{(1)}(\mathbf{r})}{\partial\, \mathbf{r}_\alpha \partial\, \mathbf{r}_\beta}. \qquad (5.2.25)
\end{aligned}
$$

The evaluation of these terms is rather cumbersome. In addition, the derivatives lead to large inverse powers of the density. When the density becomes small these terms are a source of numerical noise. One could ignore the contribution to E_{xc}^{GC} for densities smaller than a preassigned value as it is done in practice for the first order derivative. However the large negative powers that appear in the second derivative require to be cured with a much too high value of the cut-off density. This induces inaccuracies and numerical noise. We resort instead to a finite difference technique. To this effect we observe that:

$$
\begin{aligned}
& \frac{1}{2} \int d^3r \int d^3r'\, n^{(1)}(\mathbf{r}') \frac{\delta^{\,2}\mathcal{E}_{xc}}{\delta\; n^{(0)}(\mathbf{r}')\, \delta\; n^{(0)}(\mathbf{r})} n^{(1)}(\mathbf{r}) \qquad (5.2.26) \\
& = \frac{1}{2} \lim_{\varepsilon \to 0} \frac{\mathcal{E}_{xc}\left[n^{(0)}(\mathbf{r}) + \varepsilon n^{(1)}(\mathbf{r})\right] + \mathcal{E}_{xc}\left[n^{(0)}(\mathbf{r}) - \varepsilon n^{(1)}(\mathbf{r})\right] - 2\mathcal{E}_{xc}\left[n^{(0)}(\mathbf{r})\right]}{\varepsilon^2}.
\end{aligned}
$$

and therefore

$$
V_{xc}^{(1)} = \lim_{\varepsilon \to 0} \frac{V_{xc}\left(n^{(0)}(\mathbf{r}) + \varepsilon n^{(1)}(\mathbf{r})\right) - V_{xc}\left(n^{(0)}(\mathbf{r}) - \varepsilon n^{(1)}(\mathbf{r})\right)}{2\varepsilon} \qquad (5.2.27)
$$

In Eq.(5.2.27), accuracy requires the use of a small ε, but on the other hand, numerical stability favours a large ε. After some experimentation, we find that a good compromise can be achieved with a value of $\varepsilon \approx 10^{-3}$.

Our numerical approach is more reliable and stable than the analytical expression. In a PW approach, our way of proceeding is also computationally cheaper: in fact in Eq.(5.2.25) one needs to evaluate $\partial\, n^{(1)} / \partial\, \mathbf{r}_\alpha$ and $\partial^{\,2} n^{(1)} / \partial\, \mathbf{r}_\alpha \partial\, \mathbf{r}_\beta$ which require a total of 9 Fast Fourier Transforms to be compared with the 6 Fast Fourier Transforms of Eq.(5.2.27), not to mention the cost of evaluating the very complex functions in Eq.(5.2.25).

5.2.3 Preconditioning

In advanced optimization algorithms such as conjugate gradient minimization or direct inversion of the iterative subspace (DIIS), a good preconditioning is a key ingredient for optimal performance. The main objective is to reduce the condition number of the problem. In terms of the energy functional (5.2.15) to be minimized, this is equivalent to finding a good inverse of

$$H^{(0)}\delta_{\,ij} - \langle \psi_i^{(0)} | H^{(0)} | \psi_j^{(0)} \rangle. \tag{5.2.28}$$

In order to obtain a reasonably simple and numerically reliable expression, we first replace the matrix elements $\langle \psi_i^{(0)} | H^{(0)} | \psi_j^{(0)} \rangle$ by the trace of the Hamiltonian,

$$\langle \psi_i^{(0)} | H^{(0)} | \psi_j^{(0)} \rangle \qquad \mapsto \quad \delta_{\,ij}\, \frac{1}{N} \sum_k \langle \psi_k^{(0)} | H^{(0)} | \psi_k^{(0)} \rangle,$$

such that our operator Eq.(5.2.28) becomes unique for all orbitals.

In addition, we note that, since our implementation uses plane waves, the dominant contributions for high $\mathbf{G}$ come from the kinetic energy term, that in this represantation is diagonal. We thus approximate (5.2.28) by its $(\mathbf{G}, \mathbf{G})$ – elements. The

resulting expression is

$$\frac{1}{2}|\mathbf{G}|^2 + V(\mathbf{G}) - \frac{1}{N}T\,rH^{(0)}, \tag{5.2.29}$$

which can easily be inverted to obtain the preconditioning matrix. However, (5.2.29) can become very small and might almost vanish for certain **G**–vectors. To prevent the preconditioner from being singular, we smoothly keep (5.2.29) above a certain value η by transforming it to

$$\left[\left(\frac{1}{2}|\mathbf{G}|^2 + V(\mathbf{G}) - \frac{1}{N}T\,rH^{(0)}\right)^2 + \eta^2\right]^{\frac{1}{2}}$$

or optionally to an alternative variant,

$$\frac{\left(\frac{1}{2}|\mathbf{G}|^2 + V(\mathbf{G}) - \frac{1}{N}T\,rH^{(0)}\right)^2 + \eta^2}{\frac{1}{2}|\mathbf{G}|^2 + V(\mathbf{G}) - \frac{1}{N}T\,rH^{(0)}},$$

which preserves changes in the sign of (5.2.29).

In this way, our expression is never smaller that η and can safely be inverted. The final preconditioner then yields

$$\left[\left(\frac{1}{2}|\mathbf{G}|^2 + V(\mathbf{G}) - \frac{1}{N}T\,rH^{(0)}\right)^2 + \eta^2\right]^{-\frac{1}{2}} \delta_{\ ij},$$

or alternatively

$$\frac{\frac{1}{2}|\mathbf{G}|^2 + V(\mathbf{G}) - \frac{1}{N}T\,rH^{(0)}}{\left(\frac{1}{2}|\mathbf{G}|^2 + V(\mathbf{G}) - \frac{1}{N}T\,rH^{(0)}\right)^2 + \eta^2}\ \delta_{\ ij}.$$

With these preconditioners and an appropriate value of η, the number of iterations needed to minimize the second order energy functional is approximately three times less than without preconditioning.

5.3 Vibrational modes

We now turn to some illustrative examples of the method. We start with the calculation of the vibrational modes. This can be achieved diagonalizing the dynamical

matrix

$$D_{\alpha i\beta j} = \frac{1}{\sqrt{m_\alpha m_\beta}} \left(\frac{\partial\, ^2 E_{I-I}}{\partial\, R_{\alpha i} \partial\, R_{\beta j}} + \frac{\partial\, ^2 E_{KS}}{\partial\, R_{\alpha i} \partial\, R_{\beta j}} \right) \tag{5.3.1}$$

where we indicate the ions with Greek indexes $\alpha = 1, N_I$ (N_I is the number of ions) and the Cartesian coordinates with Latin indexes $i = 1, 2, 3$. The first term in this matrix can be calculated from the direct derivative of the ionic repulsion potential. The second term comes from the interaction of the electrons with the nuclei and we will shown in this section how it can be calculated using the methods presented in the previous pages. In this case we consider $3N_I$ perturbations, one for each small displacement $u_{\alpha i}$ of the atom α from its equilibrium position $\mathbf{R}\alpha$ in the direction i. The perturbative functional is given by:

$$\mathcal{E}^{pert}[n] = \int d^3r\, n(\mathbf{r}) \sum_{\beta=1,N_I} \frac{\partial\, V_{I-e}(\mathbf{r} - \mathbf{R}_\beta)}{\partial\, R_{\alpha i}} \delta_{\ \alpha\beta}, \tag{5.3.2}$$

where V_{I-e} describes the ionic Coulomb potential. In the PW approach one uses instead norm-conserving pseudopotentials [70]. Present day applications use mostly nonlocal potentials of separable form [72], which are computationally very convenient:

$$V_{I-e} = v_{loc} + \sum_{\ell=1}^{\ell_{max}} |p_\ell\rangle \omega_\ell \langle p_\ell|, \tag{5.3.3}$$

where v_{loc} is a local operator, p_ℓ the projector on the ℓ angular moment and ω_ℓ appropriated weights. Using (5.3.3) the perturbation functional reads:

$$\begin{aligned} \mathcal{E}^{pert}[n] = \int d^3r\, n(\mathbf{r}) \sum_{\beta=1}^{N_I} \frac{\partial\, v_{loc}(\mathbf{r} - \mathbf{R}_\beta)}{\partial\, R_{\alpha i}} \delta_{\ \alpha\beta} + \\ \sum_{\ell=1}^{\ell_{max}} \sum_{\beta=1}^{N_I} \sum_k \left(\langle \psi_k | \frac{\partial\, p_\ell(\widehat{r - R_\beta})}{\partial\, R_{\alpha i}} \rangle \omega_\ell \langle p_\ell(\widehat{r - R_\beta}) | \psi_k \rangle \right. \\ \left. + \langle \psi_k | p_\ell(\widehat{r - R_\beta}) \rangle \omega_\ell \langle \frac{\partial\, p_\ell(\widehat{r - R_\beta})}{\partial\, R_{\alpha i}} | \psi_k \rangle \right) \delta_{\ \alpha\beta} \end{aligned} \tag{5.3.4}$$

and the perturbative term in Eq.(5.2.15) becomes

$$\int d^3r\, n^{(1)}(\mathbf{r}) \sum_{\beta=1}^{N_I} \frac{\partial\, v_{loc}(\mathbf{r}-\mathbf{R}_\beta)}{\partial\, R_{\alpha i}} \delta_{\ \alpha\beta} +$$

$$\sum_\ell \sum_\beta \sum_k \left(\langle \psi_k^{(1)} | \frac{\partial\, p_\ell}{\partial\, R_{\alpha i}} \rangle \omega_\ell \langle p_\ell | \psi_k^{(0)} \rangle + \langle \psi_k^{(0)} | p_\ell \rangle \omega_\ell \langle \frac{\partial\, p_\ell}{\partial\, R_{\alpha i}} | \psi_k^{(1)} \rangle \right.$$

$$\left. \langle \psi_k^{(0)} | \frac{\partial\, p_\ell}{\partial\, R_{\alpha i}} \rangle \omega_\ell \langle p_\ell | \psi_k^{(1)} \rangle + \langle \psi_k^{(1)} | p_\ell \rangle \omega_\ell \langle \frac{\partial\, p_\ell}{\partial\, R_{\alpha i}} | \psi_k^{(0)} \rangle \right) \delta_{\ \alpha\beta} \tag{5.3.5}$$

The electronic term can be calculated using the Hellmann-Feynman theorem generalised to the nonlocal potential:

$$\frac{\partial\, E_{KS}}{\partial\, R_{\alpha i}} = \sum_k \langle \psi_k^{(0)} | \frac{\partial\, V_{I-e}}{\partial\, R_{\alpha i}} | \psi_k^{(0)} \rangle \tag{5.3.6}$$

and taking the second derivative:

$$\begin{aligned}
\frac{\partial^{\,2} E_{KS}}{\partial\, R_{\alpha i} \partial\, R_{\beta j}} &= \sum_k \langle \psi_k^{(0)} | \frac{\partial^{\,2} V_{I-e}}{\partial\, R_{\alpha i} \partial\, R_{\beta j}} | \psi_k^{(0)} \rangle + \\
&\langle \psi_{k,\alpha i}^{(1)} | \frac{\partial\, V_{I-e}}{\partial\, R_{\beta j}} | \psi_k^{(0)} \rangle + \langle \psi_k^{(0)} | \frac{\partial\, V_{I-e}}{\partial\, R_{\beta j}} | \psi_{k,\alpha i}^{(1)} \rangle \\
&= \sum_k \left(\langle \psi_k^{(0)} | \frac{\partial^{\,2} v_{loc}}{\partial\, R_{\alpha i} \partial\, R_{\beta j}} | \psi_k^{(0)} \rangle + \sum_\ell \langle \psi_k^{(0)} | \frac{\partial^{\,2} p_\ell}{\partial\, R_{\alpha i} \partial\, R_{\beta j}} \rangle \omega_\ell \langle p_\ell | \psi_k^{(0)} \rangle + \right. \\
&\left. \langle \psi_k^{(0)} | p_\ell \rangle \omega_\ell \langle \frac{\partial^{\,2} p_\ell}{\partial\, R_{\alpha i} \partial\, R_{\beta j}} | \psi_k^{(0)} \rangle + 2 \langle \psi_k^{(0)} | \frac{\partial\, p_\ell}{\partial\, R_{\alpha i}} \rangle \omega_\ell \langle \frac{\partial\, p_\ell}{\partial\, R_{\beta j}} | \psi_k^{(0)} \rangle \right) \delta_{\ \alpha\beta} + \\
&\langle \psi_{k,\alpha i}^{(1)} | \frac{\partial\, v_{loc}}{\partial\, R_{\beta j}} | \psi_k^{(0)} \rangle + \langle \psi_k^{(0)} | \frac{\partial\, v_{loc}}{\partial\, R_{\beta j}} | \psi_{k,\alpha i}^{(1)} \rangle \\
&+ \sum_\ell \langle \psi_{k,\alpha i}^{(1)} | \frac{\partial\, p_\ell}{\partial\, R_{\beta j}} \rangle \omega_\ell \langle p_\ell | \psi_k^{(0)} \rangle + \langle \psi_{k,\alpha i}^{(1)} | p_\ell \rangle \omega_\ell \langle \frac{\partial\, p_\ell}{\partial\, R_{\beta j}} | \psi_k^{(0)} \rangle + \\
&\langle \psi_k^{(0)} | \frac{\partial\, p_\ell}{\partial\, R_{\beta j}} \rangle \omega_\ell \langle p_\ell | \psi_{k,\alpha i}^{(1)} \rangle + \langle \psi_k^{(0)} | p_\ell \rangle \omega_\ell \langle \frac{\partial\, p_\ell}{\partial\, R_{\beta j}} | \psi_{k,\alpha i}^{(1)} \rangle
\end{aligned} \tag{5.3.7}$$

We applied the method to isolated molecules. In particular, we report in Tables 5.3.1 and 5.3.2 the results for the molecules of Disilane (Si_2H_6) and Formaldeide (CH_2O) in LDA approximation. In the case of Disilane we used a cubic cell with reticular constant of 22 a.u., Martins-Trouiller pseudopotentials [74] and a PW cutoff of 50 Ryd.

	PT	FD	$6-311G^{\ddagger}(3df,3pd)$	experiment
E_u	2153	2153	2187	2177
A_{1g}	2152.88	2152.88	2186	2163
A_{2u}	2144	2144	2177	2154
	2143	2143	2177	
E_g	2132	2132	2166	2153
	2128	2128	2162	
E_u	897	897	902	946
	896	896	902	
E_g	883	883	889	929
	883	883	889	
A_{1g}	846	846	850	910
A_{2u}	775	775	781	843
E_g	595	595	595	625
	593	593	594	
A_{1g}	428	428	433	434
E_u	337	337	338	379
	334	334	338	
A_{1u}	134	134	143	180

Table 5.3.1: Vibrational modes of Disilane

Vibrational modes of Disilane: comparison between perturbation theory (PT), finited differences (FD), Gaussian code ($6-311G^{\ddagger}(3df,3pd)$ basis set) and experiments [95]. For PT and FD we used a cubic cell with reticular constant of 22 a.u., Martins-Trouiller pseudopotentials, LDA approximation and a PW cutoff of 50 Ryd. The frequencies are in cm^{-1}.

	PT	FD	$6-311G^{\ddagger}(3df,3pd)$	6-311G	experiment
b_2	2828	2828	2850	2898	2874
a_1	2776	2776	2796	2832	2780
a_1	1809	1809	1818	1720	1743.6
a_1	1458	1458	1466	1516	1503
b_2	1214	1214	1217	1248	1280
b_1	1138	1138	1146	1177	1167

Table 5.3.2: Vibrational modes of Formaldeide

Vibrational modes of Formaldeide: comparison between perturbation theory (PT), finited differences (FD), Gaussian code ($6-311G^{\ddagger}(3df,3pd)$ and 6-311G basis sets) and experiments [96]. For PT and FD we used a cubic cell with reticular constant of 24 a.u., Martins-Trouiller pseudopotentials, LDA approximation and a PW cutoff of 70 Ryd. The frequencies are in cm^{-1}.

In the case of Formaldeide we used a cubic cell with reticular constant of 24 a.u., Martins-Trouiller pseudopotentials [74] and a PW cutoff of 70 Ryd. We performed our calculations using CPMD (Car-Parrinello-Molecular-Dynamics) code[92], where we have implemented the method here presented. We compare our results with the ones obtained by finited differences using CPMD with the same cell, cutoff and pseudopotentials and we find a very good agreement which validates our approach. For comparison we report calculation made by using the GAUSSIAN program[93], which is an all-electrons method and which expands the KS orbitals into Gaussians. We also show as a reference the experimentally determined frequencies[1] which are in good agreement with all the theoretical results.

[1]The experimental frequencies reported are the observed fundamentals [94].

Chapter 6

Raman spectra: experiments and theory

In the previous Chapters, we have introduced all the theoretical tools necessary to build up an ab-initio Raman spectrum. In the following we will describe in detail the techniques used in this thesis in order to perform such simulations. We start with a reminder to basic concepts of Raman scattering experiments. Then we show how Car-Parrinello molecular dynamics [3] is combined with the generalized variational perturbation theory, introduced in Chap.5.2, in order to obtain Raman spectra for disordered and anharmonic systems.
Finally, we validate the new theory by presenting some numerical tests.

6.1 Raman scattering experiments

Raman scattering is a spectroscopic technique that provides information about electronic, vibrational, and rotational energy levels.
When photons impinge on a system, they can impart energy to (or gain energy from)

the translational, rotational, vibrational, and electronic degrees of freedom. They thereby suffer frequency shifts. Thus, the frequency spectrum of the scattered light will exhibit resonances at the frequencies corresponding to these transitions. Raman scattering, therefore, provides information about the energy spectra. Advances in the laser techniques have made possible the measurement of very small frequency shifts in the light scattered from gases, liquids and solids.

A simplified scheme of such an experiment is the following: the light from a laser passes through a polarizer to define the polarization of the incident beam and then impinges on the scattering medium. The scattered light then passes through an analyzer which selects a given polarization and finally enters a detector. The position of the detector defines the scattering angle Θ as shown in Fig.6.1.1.

It is now convenient for the future applications to specify also the scattering geometries. Essentially we will use two scattering geometries. The plane defined by the initial and final wavevectors of the light is called scattering plane. It is necessary to define the scattering geometry in relation to the scattering plane. Once one has chosen the scattering plane, there are four different pairs of polarization directions commonly used, as shown in Fig.6.2.1. The subscripts V and H correspond to directions that are vertical and horizontal with respect to the scattering plane. I_{VV} is called polarized component and I_{VH} and I_{HV} are usually called depolarized components.

6.2 Raman intensity

We describe here a practical way of calculating Raman scattering.

We will work in the so called zero frequency limit, in which the incoming radiation cannot induce transitions to the excited electronic states. This limit is discussed for instance in the book of Berne and Pecora [108] and the Raman scattering is related

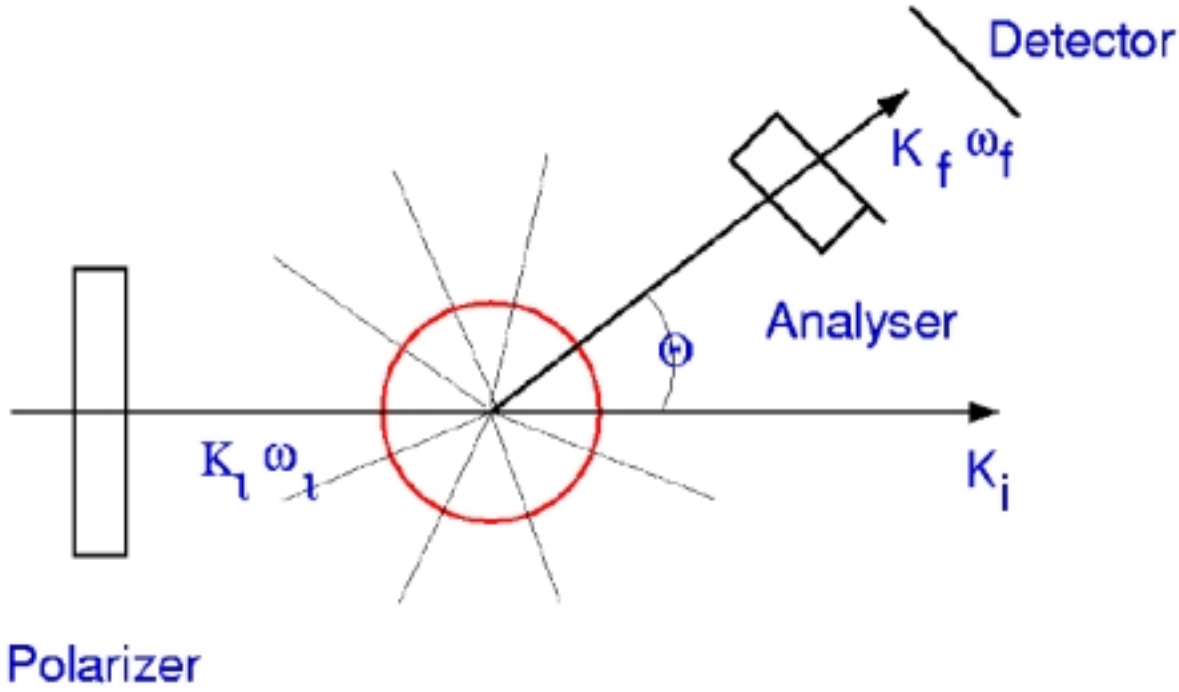

Figure 6.1.1: *Simplified scheme of a light scattering experiment: the light from a laser passes through a polarizer to define the polarization of the incident beam and then impinges on the scattering medium. The scattered light then passes through an analyzer which selects a given polarization and finally enters a detector. The position of the detector defines the scattering angle .*

to the time-dependent fluctuations of the polarizability tensor

$$\alpha\left(t\right)=\left\|-\frac{\partial\,\mathbf{P}_{\mu}}{\partial\,\mathbf{E}_{\nu}}\right\|\equiv\left\|\frac{\partial\,^{2}E}{\partial\,\mathbf{E}_{\mu}\partial\,\mathbf{E}_{\nu}}\right\| \tag{6.2.1}$$

In this limit the polarization fluctuation are induced only by atomic motions. In an isotropic system $\alpha\left(t\right)$ can be divided in an isotropic part $\alpha(t)$ and and anisotropic component $\beta(\mathbf{t})$:

$$\alpha\left(t\right)=\alpha(t)\mathbf{I}+\beta(\mathbf{t}), \tag{6.2.2}$$

where $\alpha(t)=\frac{1}{3}\mathrm{Tr}\alpha\left(\mathbf{t}\right)$. Then one has for the two different polarization scattering geometries:

$$\mathbf{I}_{VV}\left(\omega_{f}\right)\;=\mathbf{I}_{ISO}\left(\omega_{f}\right)\;+\frac{4}{3}\mathbf{I}_{VH}\left(\omega_{f}\right)\;, \tag{6.2.3}$$

where

$$\mathbf{I}_{ISO}\left(\omega_{f}\right)\;=\frac{N}{2\pi}\int dt\,e^{-i\omega_{f}t}\langle\alpha\left(0\right)\alpha\left(t\right)\rangle, \tag{6.2.4}$$

and

$$\mathbf{I}_{VH}\left(\omega_{f}\right)\;=\frac{N}{2\pi}\int dt\,e^{-i\omega_{f}t}\frac{1}{10}\left\langle \mathrm{Tr}(\beta\left(0\right)\cdot\beta\left(t\right))\right\rangle \tag{6.2.5}$$

and ω_{f} is the frequency of the scattered light.

The $\mathbf{I}_{VH}$ Raman spectrum depends on both molecular vibration and rotation, while $\mathbf{I}_{ISO}$ depends only on the vibrational motion.

6.3 Harmonic Raman spectra calculation

One possible approach to the calculation of the two components of the polarizability tensor α and β is to approximate them with their expansion in the vibrational normal coordinates of the system:

$$\alpha\mathbf{I}\simeq\alpha_{0}\mathbf{I}+\sum_{i}\frac{\partial\,\alpha\mathbf{I}}{\partial\,\mathbf{Q}_{i}}\mathbf{Q}_{i} \tag{6.3.1}$$

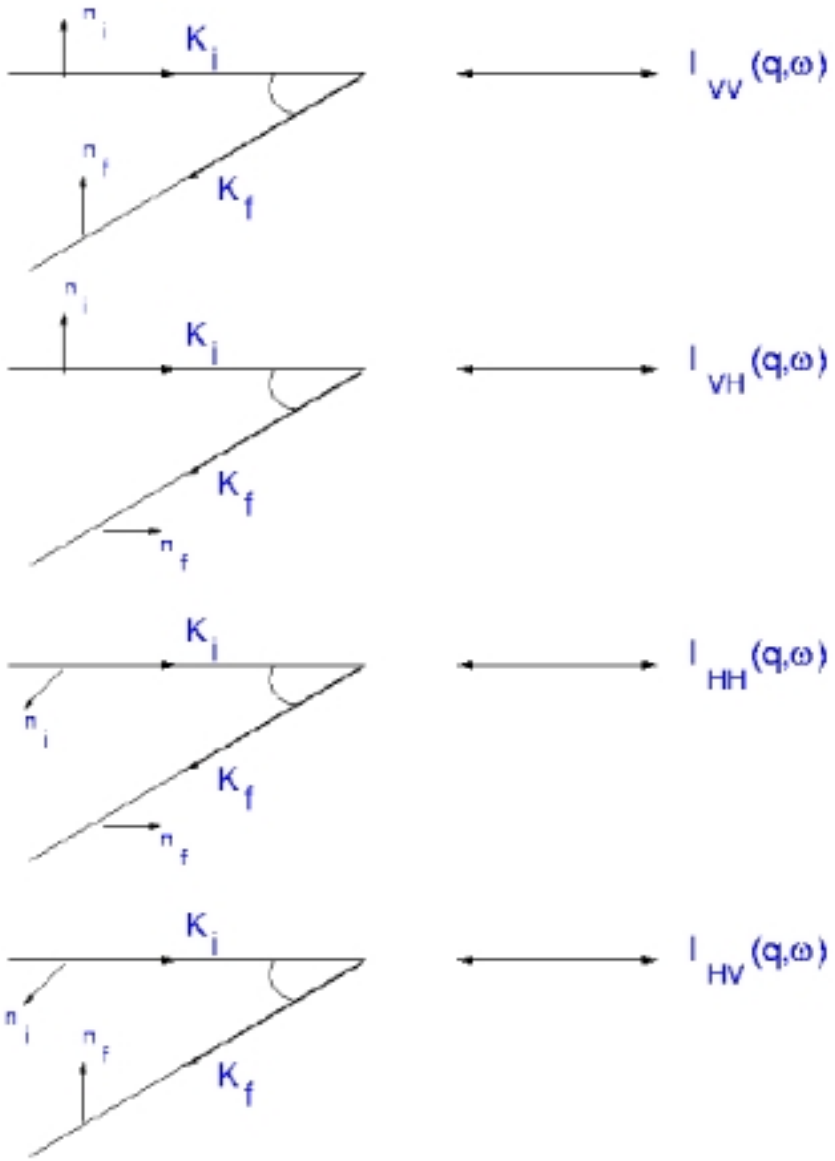

Figure 6.2.1: *Polarization geometries in light scattering experiments. The plane defined by the initial and final wavevectors of the light is called scattering plane. It is necessary to define the scattering geometry in relation to the scattering plane. Once one has chosen the scattering plane, there are four different pairs of polarization directions commonly used, VV,VH,HV, and HH. The subscripts V and H correspond to directions that are vertical and horizontal with respect to the scattering plane.* I_{VV} *is called polarized component and* I_{VH} *and* I_{HV} *are usually called depolarized component.*

$$\beta \simeq \beta_0 + \sum_i \frac{\partial\, \beta}{\partial\, \mathbf{Q}_i} \mathbf{Q}_i, \tag{6.3.2}$$

where the derivatives are evaluated at the equilibrium geometry.

Not all the normal modes of the system will contribute to the sum in Eqs.(6.3.1) and (6.3.2): a normal mode is "inactive" or "active" depending whether $(\partial\, \alpha \mathbf{I}/\, \partial\, \mathbf{Q}_i)$ and $(\partial\, \beta/\, \partial\, \mathbf{Q}_i)$ are zero. The symmetry of the normal mode may be used to determines which modes are active; if a mode has "gerade" symmetry, then it is Raman active; if it is "ungerade", it is Raman inactive and contributes only to the IR spectrum of the system. This way of calculating the Raman spectrum gives accurate results for system where the harmonic approximation is good, like perfect crystals or isolated molecules. This limitation to harmonic effects can be overcome by evaluating the polarizability as a function of the time during a molecular dynamics run, as we will explain in the next section.

6.4 Anharmonic Raman spectra calculation

In order to obtain anharmonic effects, we evaluate α and β as a function of the time during a molecular dynamics run and then apply directly Eqs. (6.2.4) and (6.2.5). However, if one is not carefull, this method can become computationally too expensive.

In fact, a single evaluation of $\alpha(t)$ in the standard approach is rather demanding, since it involves the calculation of the excitation spectrum and cannot be computed using only the ground state properties.

The textbook expression for the components of $\alpha(t)$ is:

$$\alpha_{\mu,\nu} = \sum_{c,v} \frac{\langle \psi_c | r_\mu | \psi_v \rangle \langle \psi_v | r_\nu | \psi_c \rangle}{\varepsilon_c - \varepsilon_v} \tag{6.4.1}$$

The double sum in Eq.(6.4.1) over occupied valence states and empty conducting states is notoriously difficult to carry out. One solution of this problem is to use a Green's function approach, based Sternheimer procedure[5], where the problem of calculating the excited states and evaluating the double sum is turned into an iterative scheme. However, as we have extensively discussed in Sec.4, in periodic systems the position operator is ill defined. One possibility to solve this problem, which is alternative to the modern theory of polarization, exposed in Sec.4, is the use of the velocity operator $\mathbf{v}$, which is well defined. We have:

$$\langle \psi_c | \mathbf{r} | \psi_v \rangle = -i \frac{\langle \psi_c | \mathbf{v} | \psi_v \rangle}{\epsilon_{\ c} - \epsilon_{\ v}}, \tag{6.4.2}$$

where[1]

$$\mathbf{v} = i\,[H, \mathbf{r}] = \mathbf{p} + i[v_{ext}, \mathbf{r}]. \tag{6.4.3}$$

Using this expression for the position expectation value, one rewrites Eq.(6.4.1) as:

$$\alpha_{\mu,\nu} = \sum_{c,v} \frac{\langle \psi_c | v_\mu | \psi_v \rangle \langle \psi_v | v_\nu | \psi_c \rangle}{(\epsilon_{\ c} - \epsilon_{\ v})^3}, \tag{6.4.4}$$

which can be also recasted in a computationally more convenient form:

$$\alpha_{\mu,\nu} = \sum_{c,v} \frac{\langle \psi_c | v_\mu | \psi_v \rangle \langle \psi_v | \dfrac{\partial\, V_{eff}}{\partial\, E_\nu} | \psi_c \rangle}{(\epsilon_{\ c} - \epsilon_{\ v})^2}. \tag{6.4.5}$$

This formula alleviates but does not solve the problems associated with the slow double sum convergence. The quantity $1/\left(\epsilon_{\ c} - \epsilon_{\ v}\right)^2$ goes rapidly to zero as the band index c increases, but when c runs over the lowest conduction bands, small changes in

[1] Note that, when one uses nonlocal pseudopotentials, the commutator $[v_{ext}, \mathbf{r}]$ is different from zero.

the energy denominator causes large variations in the integrand, making numerical integration instable.

Thus, one has to resort to the Sternheimer procedure.

In order to obtain a convienient form for practical purposes, one defines

$$|\phi_v^\mu\rangle = \sum_c |\psi_c\rangle \frac{\langle\psi_c|[H, r_\mu]|\psi_v\rangle}{\epsilon_c - \epsilon_v} = P_c G_0(\epsilon_v) P_c [H, r_\mu]|\psi_v\rangle, \tag{6.4.6}$$

where P_c is the projector over the conduction-state manifold, and $G(\epsilon) = 1/(\epsilon - H)$ is the one-electron Green's function of the unperturbed system. If now one introduces the following notation for the response of the wavefunction $|\psi_v\rangle$ to an applied electric field:

$$\left|\frac{\partial \psi_v}{\partial E_\nu}\right\rangle = P_c G_0(\epsilon_v) P_c \frac{\partial V_{eff}}{\partial E_\nu}|\psi_v\rangle, \tag{6.4.7}$$

the polarizability tensor reads:

$$\alpha_{\mu,\nu} = \sum_v \langle\phi_v^\mu \left|\frac{\partial \psi_v}{\partial E_\nu}\right\rangle. \tag{6.4.8}$$

However, due to the necessity to avoid the explicity evaluation of the Green's function in Eqs.(6.4.6) and (6.4.7), the Sternheimer procedure has to be repeated twice.

The use of the variational perturbation theory, introduced in Chap.5, overcomes this problem. As discussed before, in order to be able to treat the polarizability in such a scheme, we have generalized the theory to non-hamiltonian perturbations.

The coupling of the electric field with the polarization induces a perturbation in the KS functional of the type:

$$\lambda \mathcal{E}^{pert}[\{|\psi_v\rangle\}] = -\mathbf{E}\cdot\mathbf{P}^{ele} = -\sum_\nu E_\nu \frac{2|e|}{|\mathbf{G}_\nu|} \mathrm{Im}\log\det\left\langle\psi_v\left|e^{i\mathbf{G}_\nu\cdot\mathbf{r}}\right|\psi_{v'}\right\rangle \quad . \tag{6.4.9}$$

In this formula we have used the fact, extensively exposed in Chap.4, that the polarization in the Γ only sampling of the Brillouin zone can be expressed in terms of the Berry phase γ_μ, Eq.(4.5.1) [8–10,14]. In this approach,

$$P_\mu^{ele} = \frac{2|e|}{|G_\mu|}\gamma_\mu = \frac{2|e|}{|G_\mu|}\mathrm{Im}\log\det\mathbf{Q}^{(\mu)},$$

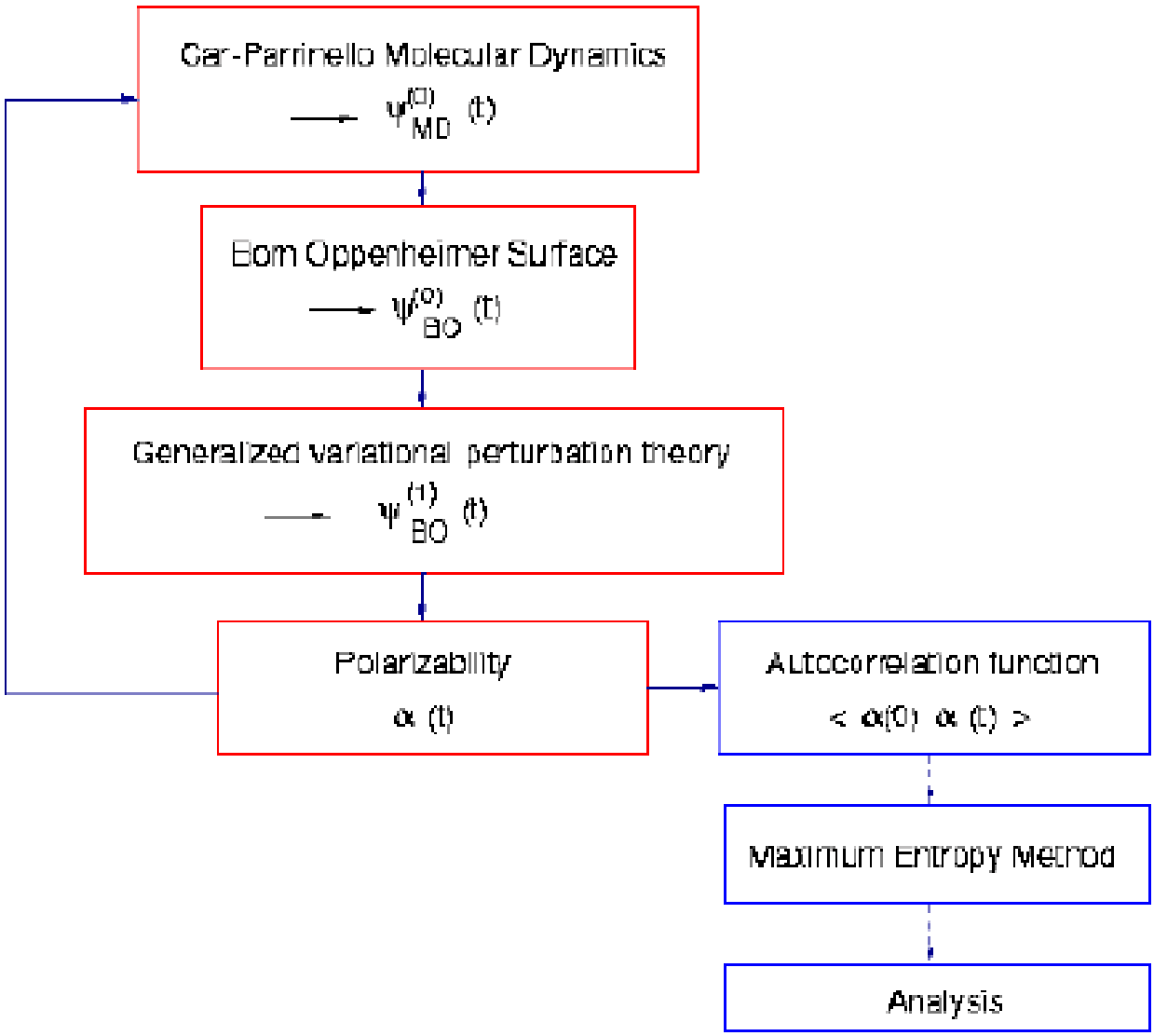

Figure 6.4.1: *This scheme illustrate how one can calculate the Raman spectrum of a system, using Car-Parrinello molecular dynamics and generalized variational perturbation theory.*

where the matrix $\mathbf{Q}^{(\mu)}$ is defined as $\mathbf{Q}^{(\mu)}_{i,j} = \left\langle \psi_i \middle| e^{i\mathbf{G}_\mu \cdot \mathbf{r}} \middle| \psi_j \right\rangle$, and $\mathbf{G}_\mu$ is the smallest vector in a periodically repeated cubic cell in the direction μ. This expression can be generalized to cells of arbitrary shape, as explained in appendix A.

This formula is in principle valid in the limit of a cell of infinite dimension, but is a good approximation in a non conducting material, even with relatively small supercells. In this particular case the perturbative parameter is E_ν and $|\psi_i\rangle \simeq |\psi_i^{(0)}\rangle - E_\nu |\psi_i^{(1)}\rangle$.

The derivative $\delta\ \mathcal{E}^{pert}/\ \delta\ \langle\psi_i^{(0)}|$ and its ket conjugate, necessary to calculate the functional of Eq.(5.2.10), can be evaluated using the formula for the derivative of a matrix A with respect to a generic variable x:

$$\frac{d}{dx} \ln \det A = \frac{dA_{ij}}{dx} A^{-1}_{ji}. \tag{6.4.10}$$

The perturbative term in Eq.(5.2.10) becomes:

$$\frac{2\,|e|}{|\mathbf{G}_\nu|} \mathrm{Im} \left[\sum_{i,j} \left(\left\langle \psi_i^{(1)} \middle| e^{i\mathbf{G}_\nu \cdot \mathbf{r}} \middle| \psi_j^{(0)} \right\rangle + \left\langle \psi_i^{(0)} \middle| e^{i\mathbf{G}_\nu \cdot \mathbf{r}} \middle| \psi_j^{(1)} \right\rangle \right) \mathbf{Q}^{(\nu)-1}_{j,i} \right]. \tag{6.4.11}$$

Using this perturbative term in Eq.(5.2.10) we can calculate, solving the nonlinear system of equations (5.2.23), the first order correction to the wavefunctions $\{\psi_i^{(1)}\}$. This allows us to evaluate the induced dipole moment in the μ direction to linear terms:

$$\begin{aligned} \delta\ P^{ele}_\mu &= \frac{2\,|e|}{|\mathbf{G}_\mu|} \delta\ \gamma_\mu \qquad (6.4.12) \\ &= -\sum_\nu \frac{2\,|e|}{|\mathbf{G}_\nu|} \mathrm{Im} \left[\sum_{i,j} \left(\left\langle \psi_i^{(1)} \middle| e^{i\mathbf{G}_\mu \cdot \mathbf{r}} \middle| \psi_j^{(0)} \right\rangle + \left\langle \psi_i^{(0)} \middle| e^{i\mathbf{G}_\mu \cdot \mathbf{r}} \middle| \psi_j^{(1)} \right\rangle \right) \mathbf{Q}^{(\nu)-1}_{j,i} \right] E_\nu \end{aligned}$$

and the polarizability $\alpha_{\mu,\nu} = -\partial\ P_\mu/\ \partial\ E_\nu$

$$\begin{aligned} \alpha_{\mu,\nu} = & \qquad (6.4.13) \\ & \frac{2\,|e|}{|\mathbf{G}_\nu|} \mathrm{Im} \left[\sum_{i,j} \left(\left\langle \psi_i^{(1)} \middle| e^{i\mathbf{G}_\mu \cdot \mathbf{r}} \middle| \psi_j^{(0)} \right\rangle + \left\langle \psi_i^{(0)} \middle| e^{i\mathbf{G}_\mu \cdot \mathbf{r}} \middle| \psi_j^{(1)} \right\rangle \right) \mathbf{Q}^{(\nu)-1}_{j,i} \right]. \end{aligned}$$

L(a.u.)	α_1	α_2	α_3
		A^3	
15	1.46	1.36	1.27
25	1.57	1.51	1.47
35	1.61	1.57	1.53
45	1.63	1.59	1.57
ref[97]	1.62	1.60	1.59

Table 6.4.1: Polarizability of a molecule of water

Polarizability of a molecule of water as a function of the length L of the cubic cell. We used Martins-Trouiller pseudopotentials, BLYP gradient corrections functional and a PW cutoff of 70 Ryd.

In order to find the minimum of (5.2.15) we use a preconditioned conjugated gradient approach (see Sec.5.2.3).

6.5 Test of the method

We tested the new method in several different situations. We first checked the accuracy of the evaluation of the polarizability in the case of isolated molecules, then we applied the method to a periodic system.

6.5.1 Calculation of the polarizability of molecules

We tested the validity of this approach performing a set of calculations on isolated molecules which we treat within the supercell scheme. In order to evaluate the effect of the finite dimension of the cell, we performed several calculations with different sizes of the cell and we extrapolated the value of the polarizability for

N	8	64	216	Ref.[99]
ϵ_{∞}	6.6	8.58	9.81	12.9

Table 6.5.1: Dielectric constant of Silicon

Dielectric constant of Silicon: we performed several calculations of ϵ_∞ as a function of the number of atoms in the cell. We used PW, Car-von Barth pseudopotential and LDA approximation.The cutoff was of 14 Ryd.

an infinite cell. We report this study in the case of a molecule of water in Table 6.4.1. We have compared our results with standard quantum chemical calculations. The agreement was excellent expecially considering the difference between the two calculations (different basis set, use of the pseudopotential in our case, etc. etc.).

6.5.2 Calculation of the dielectric constant

We applied the present scheme to a truly periodic systems, where the use of the Berry phase approach is mandatory. Here the comparison is less straightforward since one needs to perform adequate sampling over the Brillouin Zone(BZ). The present implementation is restricted to the Γ point only of the BZ and therefore BZ sampling convergence studies have to be replaced with calculations on larger and larger supercells. In particular we treat the case of silicon and we compare with the results of Baroni and Resta [98]. First we evaluated the dielectric constant ϵ_{∞}:

$$\epsilon_{\infty} = 1 + 4\pi \frac{\partial \mathbf{P}}{\partial \mathbf{E}} \tag{6.5.1}$$

and we compared our results with the results of Dal Corso et al. [99]. As one can see from Table 6.5.1 the convergence of such a quantity with the number of atoms in the cell is quite slow.

Because we are interested in Raman spectrum calculations, we performed a more

N	8	64	Ref[98]	experiment
$\gamma(u)/\ u$	6	6	7.15	6.2 ± 1

Table 6.5.2: Raman activity of Silicon

$\gamma(u)/u$ for Silicon: comparison with the previous results of Baroni and Resta[98]. We present the data for $u = 0.0001$.

stringent test evaluating by a finite difference method the derivative of the polarizability with respect to the atomic displacements from the equilibrium γ, which is the quantities that really determine the Raman activity.

The latter converge much faster. In fact we calculate the value of the derivatives of the polarizability in the direction $(1, 1, 1)$ for different values of a dimensionless amplitude u moving the atomic positions of $\pm ua(1, 1, 1)$ where a is the lattice constant. The results for $\gamma(u)/\ u$, reported in Table 6.5.2 are in good agreement with [98] and show that these derivatives converge to a limit value independently from the size of the cell.

6.6 Technical details

In the following, we describe the practical procedure which should be followed in order to calculate and analyze a Raman spectrum.

6.6.1 *Ab initio* simulation

As discussed in the previous pages, in order to simulate first-principles Raman spectra for disordered and anharmonic systems one should combine Car-Parrinello molecular dynamics with the evaluation of the polarizability (see Eq.(6.4.14)) through

the modern theory of polarization and generalized variational perturbation theory. However, it is important to notice that the latter holds only if the ground state wavefunctions are exactly on the BO surface: simple algebra shows that if the $\{\psi^{(0)}\}$ are not exactly on the BO surface, the $2n+1$ theorem does not hold any more. This implies that is not possible to use directly the Car-Parrinello wavefunctions to calculate the polarizability following Eq.(6.4.14).

It is therefore necessary to calculate the exact ground state wavefunctions minimizing the ground state energy, even if the wavefunctions obtained through Car-Parrinello molecular dynamics are not so different from the exact ones (see Sec.3.3.2). A scheme of such a procedure is shown in Fig.6.4.1.

6.6.2 Smoothing a spectrum: maximum entropy method

Once one has a set of polarizability $\{\alpha(t)\}$ as a function of the time, one calculates the autocorrelation function $C(t) = \langle\alpha(0)\alpha(t)\rangle$ and obtains the spectrum transforming $C(t)$ in the frequency domain, through Eq.(6.2.3). There are several method to do such a transformation.
The truncation of $C(t)$ after a finite time, and the presence of random statistical errors, makes the evaluation of the Fourier transform difficult [77]. Spurious feature in $C_{run}(\omega)$, produced by transforming a truncated $C_{run}(t)$, can obscure the features present in the complete spectrum $C(\omega)$. In particular, the truncation causes spectral leakage, which often results in rapidly varying side-lobes around a peak, and loss of resolution.

The maximum entropy method is a technique for computing the most uniform spectrum consistent with a set of data. In practice the method works as follows.
We make the assumption that every discrete point $C_{run}(\tau)$ in the correlation func-

tion has a Gaussian error associated with it which is described by the variance $\sigma^2(\tau)$. The quantity that we shall be varying is a trial fit spectrum $C_{fit}(\nu)$ evaluated at a large number of discrete frequencies ν. We can easily transform $C_{fit}(\nu)$ to obtain the trial correlation function $C_{fit}(\tau)$, and the measure of a good fit is the quantity:

$$\chi^2 = \sum_{\tau=1}^{\tau_{max}} \frac{|C_{fit}(\tau) - C_{run}(\tau)|^2}{\sigma^2(\tau)} \tag{6.6.1}$$

In fact, a reasonable fit (one within the statistical errors) would have $\chi^2 = \tau_{max}$ and the technique will aim to fix χ^2 at this value. The most probable fit subject to this constraint is obtained by maximizing

$$-\sum_{\nu} C_{fit}(\nu)\log C_{fit}(\nu) + \frac{\lambda}{2}\sum_{\tau=1}^{\tau_{max}} \frac{|C_{fit}(\tau) - C_{run}(\tau)|^2}{\sigma^2(\tau)}. \tag{6.6.2}$$

λ is a Lagrange multiplier which constraints χ^2 to be a constant. The first term in Eq.(6.6.2) is the information-theoretical entropy of the spectrum. By differentiation we obtain

$$C_{fit}(\nu) = \exp\left\{-1 + \lambda\left[\frac{1}{\tau_{max}}\sum_{\tau=1}^{\tau_{max}} \frac{(C_{fit}(\tau) - C_{run}(\tau))}{\sigma^2(\tau)}\exp(2\pi i\nu\,\tau/\,\tau_{max})\right]\right\}, \tag{6.6.3}$$

which can be solved iteratively. For a particular λ, we begin with a uniform $C_{fit}(\nu)$ to produce by transformation $C_{fit}(\tau)$. This is used to recalculate $C_{fit}(\nu)$, and the process repeated to convergence. The whole procedure is carried out for a number of λ value until we obtain a consistent $C_{fit}(\nu)$ which has $\chi^2 = \tau_{max}$.

6.6.3 Normal modes and velocity-velocity spectrum

One of possible method of assignments of the peaks in a spectrum is the analysis of the normal modes $\mathbf{Q}_i$ $(i = 1, 3N_I)$ of the system. In Sec.5.3 we have described how it is possible to obtain them from the variational perturbation theory. Given a particular normal mode $\mathbf{Q}_i$, it is possible to identify the corresponding peak of the

spectrum (IR or Raman, following the symmetry of the mode, as we have explained in Sec.6.3), projecting the mode on the velocities $\mathbf{v}_\alpha$ ($\alpha = 1, N_I$)

$$\tilde{v}_i(t) = \sum_{\alpha=1}^{N_I} \sum_{j=1}^{3} \frac{1}{M_\alpha} Q_{i\alpha j} v_{\alpha j}(t) \tag{6.6.4}$$

The spectrum obtained from the autocorrelation function $\langle \tilde{v}_i(0)\tilde{v}_i(t)\rangle$ is characterized by a single peak (and its overtones) which corresponds to the particular mode $\mathbf{Q}_i$ used in the projection. Obviously, such a method to identify peaks works properly only for harmonic systems.

6.7 Raman spectrum of a single water molecule

Finally, we tested the procedure to calculate the Raman spectrum on a very simple and harmonic system, an isolated water molecule. In order to do this, we follow the procedure illustrated in Fig.6.4.1 for the case of a single water molecule in a cubic box of 10 a.u., which is big enough to consider the molecule isolated. The simulation was done using Martin-Trouillers [74] pseudopotentials and BLYP exchange and correlations potential, which is at present one of the best ways to describe the hydrogen bond in DFT [67].

Once one has excluded molecular rotations and translations, there are three normal modes for the water molecule: symmetric stretching ν_1, antisymmetric stretching ν_3, and bending ν_2. A schematic plot is shown in Fig.6.7.1. Only one of these modes, ν_1, is Raman active. The observed frequency (fondamental) of this mode is 3657 cm^{-1}, the harmonic corrected frequency is of 3832 cm^{-1} [94]. Several calculations of such a frequency through DFT, but using different basis sets and exchange-correlation potentials, range from 3400 to 3600 cm^{-1}. Our simulated Raman spectrum show a well defined peak at $\sim$ 3330cm^{-1}, in good agreement with experimental and theoretical data, as can be observed in Fig.6.7.2.

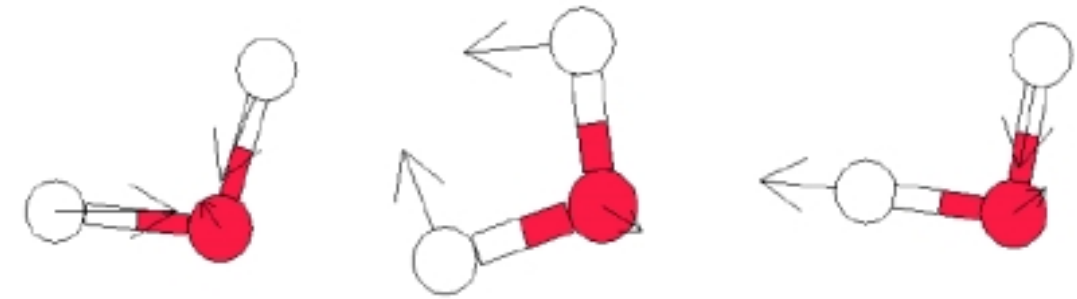

Figure 6.7.1: *Normal modes of a water molecule. Left panel: symmetric stretching ν_1; Center panel: bending ν_2; Right panel: antisymmetric stretching ν_3.*

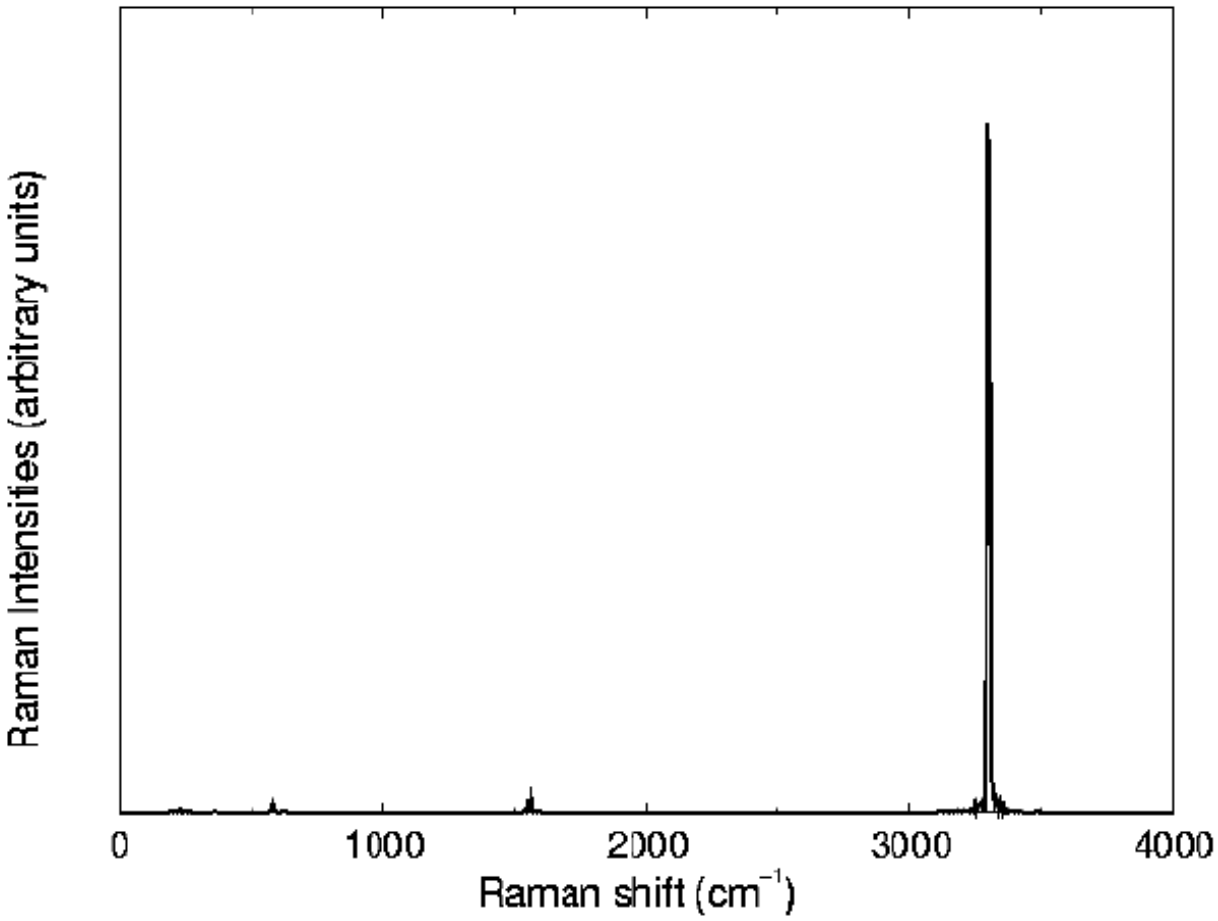

Figure 6.7.2: *Raman spectrum of a single water molecule: only the symmetric stretching ν_1 is Raman active. The peak we obtain is in good agreement with the calculated frequency for this mode within DFT [94].*

Chapter 7

High pressure ice

7.1 Introduction

The hydrogen bond is one of the most important interactions in nature. It is responsible for several phenomena which are of interest in many areas of science, ranging from biology to planetary physics [27].

In particular, this bond is the reason for the very complicated and interesting phase diagrams of water, which is the most common molecule on the earth's surface and constitutes about 70% of the human body. A schematic picture of such a phase diagram is shown in Fig.7.1.1.

The high pressure region of the phase diagram of ice is very important for condensed matter, planetary physics [27] and biology. In the last 25 years, a lot of effort has been dedicated to the study of the phase transition from ice VIII to ice X[29]. However, only very recently has the development of new experimental techniques, which permit to work at very high pressures, and of powerful simulation tools open up the possibility of a deeper investigation of such a phenomenon.

This phase transition, which will be described later, is very interesting because it

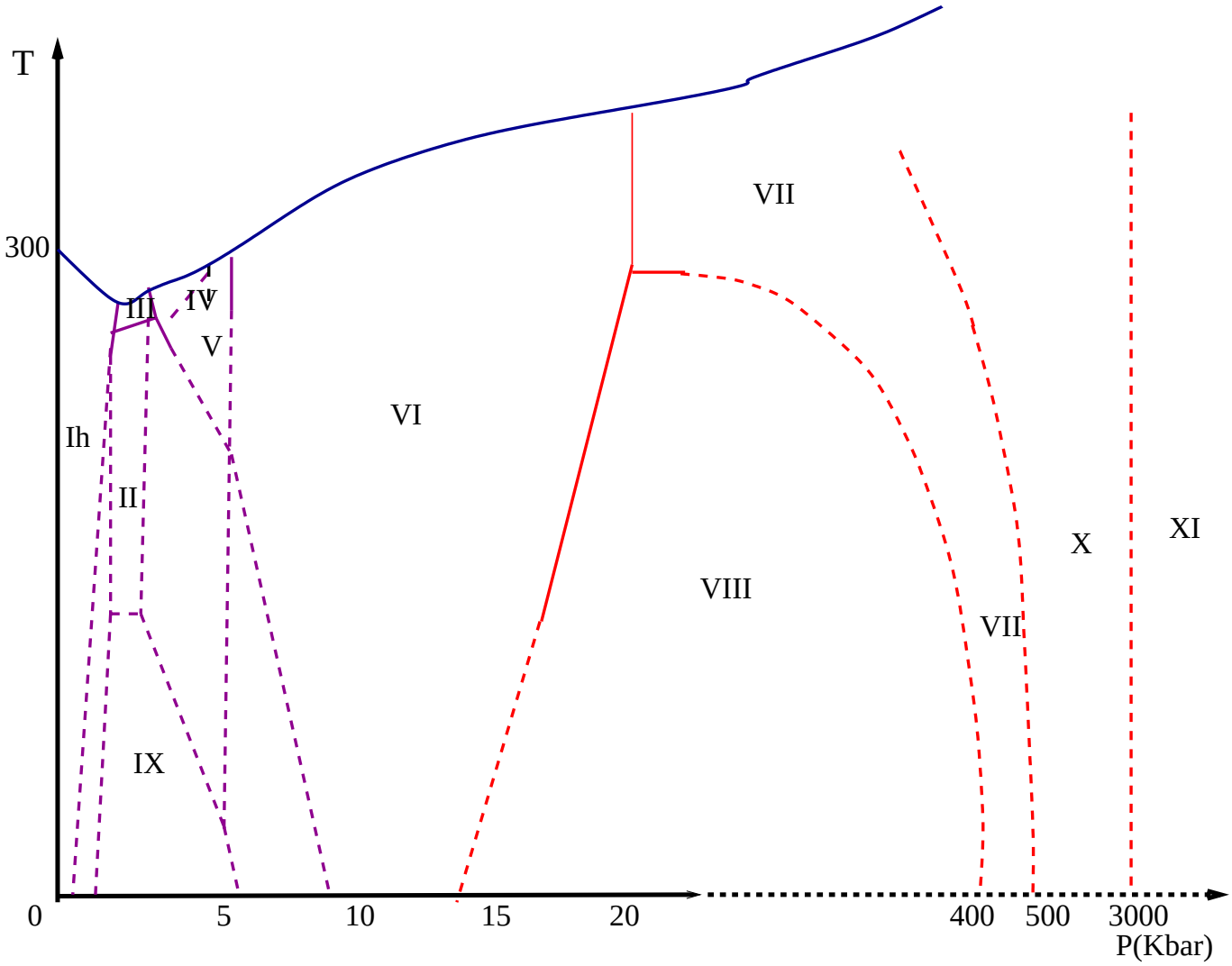

Figure 7.1.1: *At least 14 varieties of solid ice have been observed in various domains of the pressure-temperature (p, T) plane, which correspond to different amorphous or crystalline networks of the H_2O molecule.*

involves the phenomenon of proton transfer. This behavior of ice is a good prototype of similar phenomena in much more complex biological systems, for example in the HIV enzyme [28].

Furthermore, the study of high pressure ice is important in planetary physics, because H_2O is a major component of Saturn, Uranus, and Neptune.

A slightly different phenomenon happens in hydrogen-bonded ferroelectrics or antiferroelectrics such as KH_2PO_4, $NH_4H_2PO_4$, and $H_2C_4O_4$ under pressure. Usually,

a disordered crystal progressively orders under pressure, but these compounds do not. In this class of crystals, the temperature T_c of the order-disordered transition is known to decrease with increasing pressure in more than 30 H-bonded compounds, and often tend to 0 K at a critical pressure p_c. In other words, at pressures above p_c the system is disordered even at very low temperature. In the paraelectric phase of these systems, the proton positions are disordered along the H-bonds whereas they are ordered in the ferroelectric (or antiferroelectric) phase. The behavior of these systems is somehow similar to the one of ice, as we will see in detail in the following section. However, in these other systems, the type of disorder, which is very likely at the origin of the pressure dependence of T_c, is not rotational but only translational.

As will be explained in this Chapter, Raman spectroscopy is a very useful tool to investigate this problem. Various theoretical and experimental results reported sofar and their validation by our computer simulation of the Raman spectrum have been discussed.

7.2 Structures of ice VIII, VII and X

Ordinary ice (ice Ih), which is stable at atmospheric pressure, is only one of the many phases of ice. Depending on the temperature and on the pressure several different phases exist: at least 14 varieties of solid ice have been observed in various domains of the pressure-temperature (p, T) plane, which correspond to different amorphous or crystalline networks of the H_2O molecule.

For reasons described below, we are interested in three of these phases, ice VIII, VII and X.

Ice VIII has one of the simplest structures compared to other phases of ice. It is composed of two interpenetrating but not interconnected sublattices of hydrogen bonded water molecules, where the oxygen atoms form a slightly tetragonally dis-

torted body-centered-cubic structure [30].
The space group is $I4_1/$ amd(D_{4h}^{19}) and the primitive cell, shown in Fig.7.2.1, includes 8 molecules.

Neutron diffraction studies have shown the structure to be both fully proton and oxygen ordered [31]. The structure can be viewed as being built up from two interprenetrating ice Ic lattices, where the direction of the dipole moments of water molecules in one lattice is opposite to the direction in the other lattice; the final system is antiferroelectric. The two lattices are not perfectly centered with respect to each other. If they were, the oxygen atoms would lie in a body-centered arrangement. As a result of this displacement, each water molecule will have two non-hydrogen bonded neighbors that are closer than the four hydrogen bonded neighbors.

As the pressure increases a new phase, ice VII, appears. This phase transition has a clear experimental fingerprint, the disappearance of the tetragonal distortion. Proton disorder set in and the proton occupies with equal probability two symmetric positions along the O-O bond [31,32]. This structure, shown in the left panel of Fig.7.2.2, is disordered and paraelectric. The symmetry is cubic, the space group $Pn\bar{3}m$ with 2 molecules per unit cell. In the low-pressure region and at high temperature, the disorder of this structure is believed to be induced by the rotations of molecules, which creates Bejerrum defects, whereas at high pressures, the dominant mechanism is thermal hopping and/or tunneling of the proton along the hydrogen bond.

At even higher pressures it is speculated that there exists another phase, ice X[33–36], where the molecular-crystal structure breaks down completely and transforms into a non-molecular structure (Cu_2O type) connected by hydrogen bond symmetrization induced by the pressure, as can be seen in Fig.7.2.2. The overall symmetry of this structure is increased and the hydrogen atoms are tetrahedally arranged in the cubic sublattice. The resulting space group is Pn3m (O_h^4).

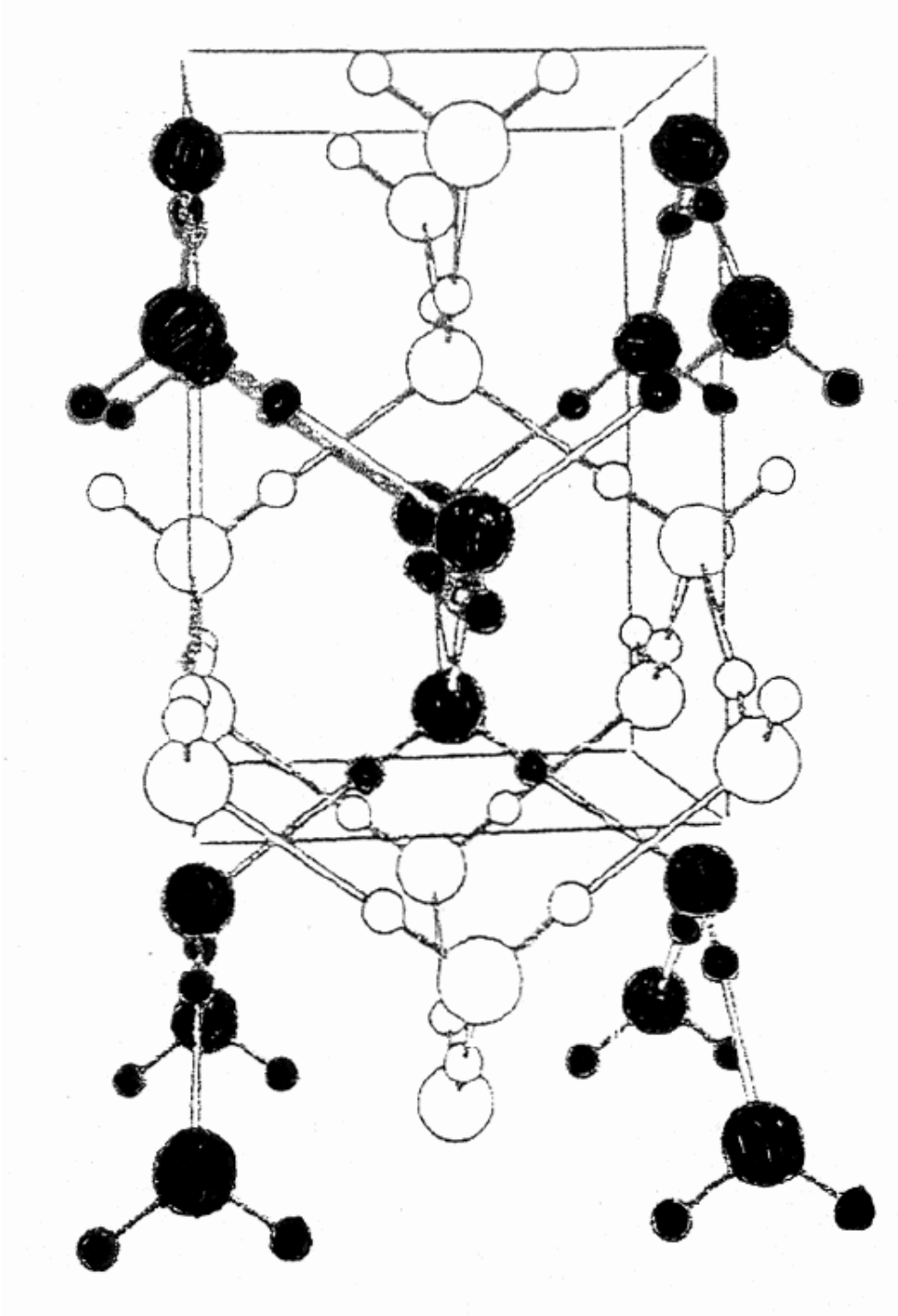

Figure 7.2.1: *Snapshot of the crystal structure of ice VIII. One of the two interprenetrating lattices has been shadowed. (Picture from Ref.[30])*

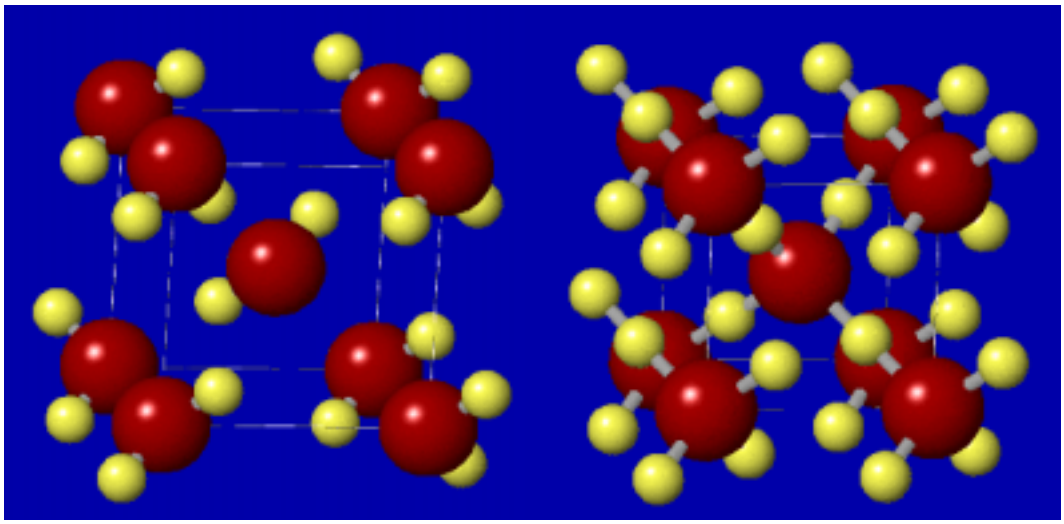

Figure 7.2.2: *Left panel: snapshot of the crystal structure of orientationally-disordered ice VII. Right panel: snapshot of the crystal structure of ice X.*

The boundaries between ice VIII and VII in the phase diagram are well defined and identified by the loss in phase VII of the tetragonal distortion. However, the boundary regions of ice X are still not well defined [37], because a definite identification of the H-bond symmetrization requires structural tools able to probe the H sublattice. These are still lacking. X-ray diffraction data were obtained up to 128 GPa [38] but provided no information about the proton sublattice, while neutron diffraction studies, which are able to locate the H positions, have been reported only up to 20 GPa [39]. Neutron diffraction experiments at higher pressures are at present no possible, because the only samples, which can be brought at so high pressure, are too small to apply this technique. Experiments, first-principles molecular dynamics simulations and infrared calculations [43] suggest that ice VIII does not transform directly into ice X, but the phase transition happens between ice VII and X. However, the boundaries of this phase transition are still not completely

clear. It is supposed [37] that, with increasing pressure, rotational-disordered ice VII, present around 2.5 GPa, transforms into translational-disordered ice VII. This seems to be indicated from the change of slope of the transition temperature T_c *vs* pressure curve (Fig.7.2.3), observed around 12-18 GPa. Furthermore, above 15 GPa a regular decrease of T_c with pressure, similar to what is encountered in other H-bonded compounds, characterized only by translational disorder, is observed. This phase transforms then into proton-disordered ice X, which under further compression transforms into proton-ordered ice X. A scheme of this particular region of the diagram of phase is shown in Fig.7.2.3 [37].
It is important to mention that it is experimentally very difficult to identify the position of the hydrogen at so high pressures. Furthermore, the description of low energy Bejerrum defects through *ab initio* simulations is practically impossible, because it requires the use of very big simulation cells and very long simulation times.

7.3 Group theory

Using symmetry properties, one can identify the fingerprints of phase VIII and phase X, which should be present in IR and Raman spectra. An inspection of such symmetry coordinates shows that with the phase transition, almost all the Raman active modes of ice VIII become optically inactive zone boundary modes, only the $\nu_{T_z}B_{1g}$ and $\nu_{T_{xy}}E_g$ lattice modes would develop into a triply degenerate, Raman active T_{2g} mode, totally decoupled from the hydrogen motions. This result comes directly from the analysis of the correlation tables in group theory.
In fact, the crystalline structure of ice VIII is represented by the group D_{4h}, which is a subgroup of O_h, to which the structure of ice X belongs. In the correlation table of O_h is shown that the representation of lower symmetry $B_{1g} + E_g$ of its subgroup D_{4h} goes into the representation of full symmetry T_{2g}[112]. The complete result of

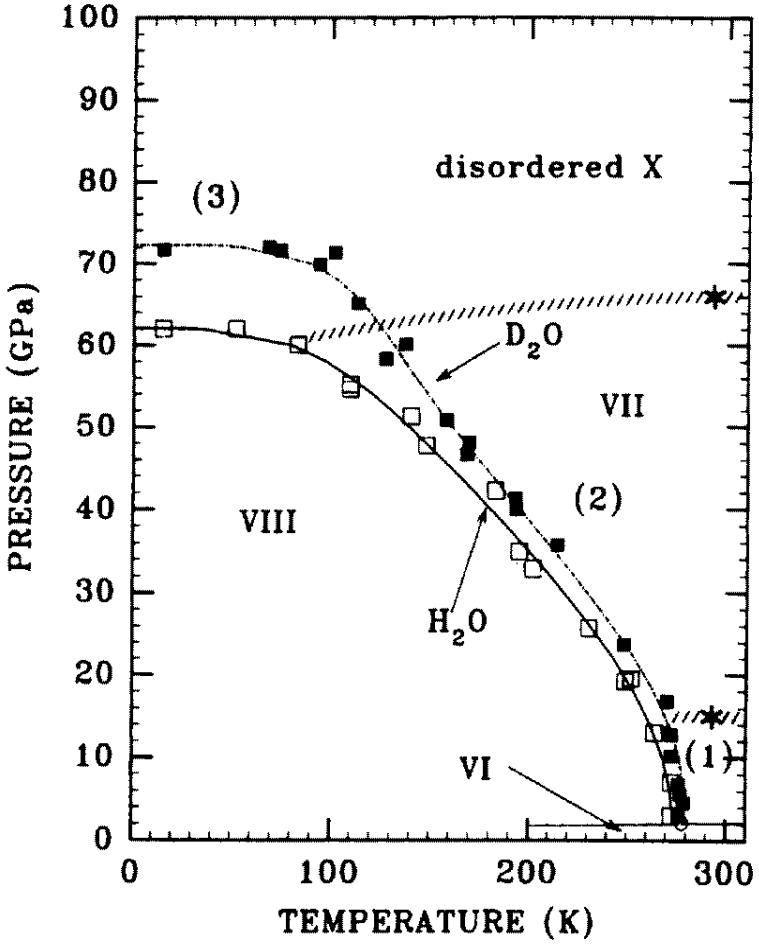

Figure 7.2.3: *Phase transition from ice VIII to ice X. ice VII-VIII transition line pressure p (GPa) as a function of temperature (K). Hollow and filled squares: experimental points for H_2O and D_2O, respectively. Solid and dotted lines: fit of the data for H_2O and D_2O, respectively. Hatched zones: expected transition lines from rotational disorder (1) to quasistatic disorder (2) and from quasistatic disorder (2) to translational disorder (3) named disordered ice X. This latter line is not shown for deuterated ice. $*$: from X-ray data. (Picture from Ref.[37])*

the vibrational analysis is illustrated schematically in Fig.7.3.1 including the assignments for the zone center modes. Part of the stretching, bending, and rotational modes of ice X are identical to those of a tetrahedron, while the new decoupled mode of oxygen with T_{2g} symmetry is identical to the same mode of carbon in diamond. As indicated in Fig.7.3.1, one expects that the two IR active $\nu_1 A_{2u}$ and $\nu_3 E_u$ stretching modes and the two $\nu_2 A_{2u}$ and $\nu_{Rxy} E_u$ bending rotational modes of ice VIII remain IR active in ice X as triply degenerated T_{1u} modes. All selection rules instead break down in the case of ice VII.

This behavior was claimed to be observed by Hirsch et al.[33] in 1986 in Raman experiments; however, at that time there were still not avaliable tools to really perform experiments at very high pressure (the highest pressure possible was of the order of 50 Gpa) and the results remained controversial.

7.4 Proton transfer

The phase transition of ice, described in the previous pages, has a link with the proton transfer phenomena. It has been known for more than half a century that the potential acting on a proton, which moves along a hydrogen bond between two heavy atoms, depends crucially on the distance between donor and acceptor, i.e. on the length of the hydrogen bond. In ice, both donor and acceptor are oxygen atoms and the basic proton transfer situation may be sketched as $O--H\cdots O \rightleftharpoons O\cdots H--O$, neglecting any charges or residual atoms. The crucial point is that the one-dimensional adiabatic electronic potential acting on the shared proton, that is transferred from one oxygen atom to the other one, changes qualitatively as a function of the OO separation: in Fig. 7.4.1 the solid line describes the case of four representative distances between the two oxygen atoms. For large separations (a), the proton is preferentially covalently bound to one of the

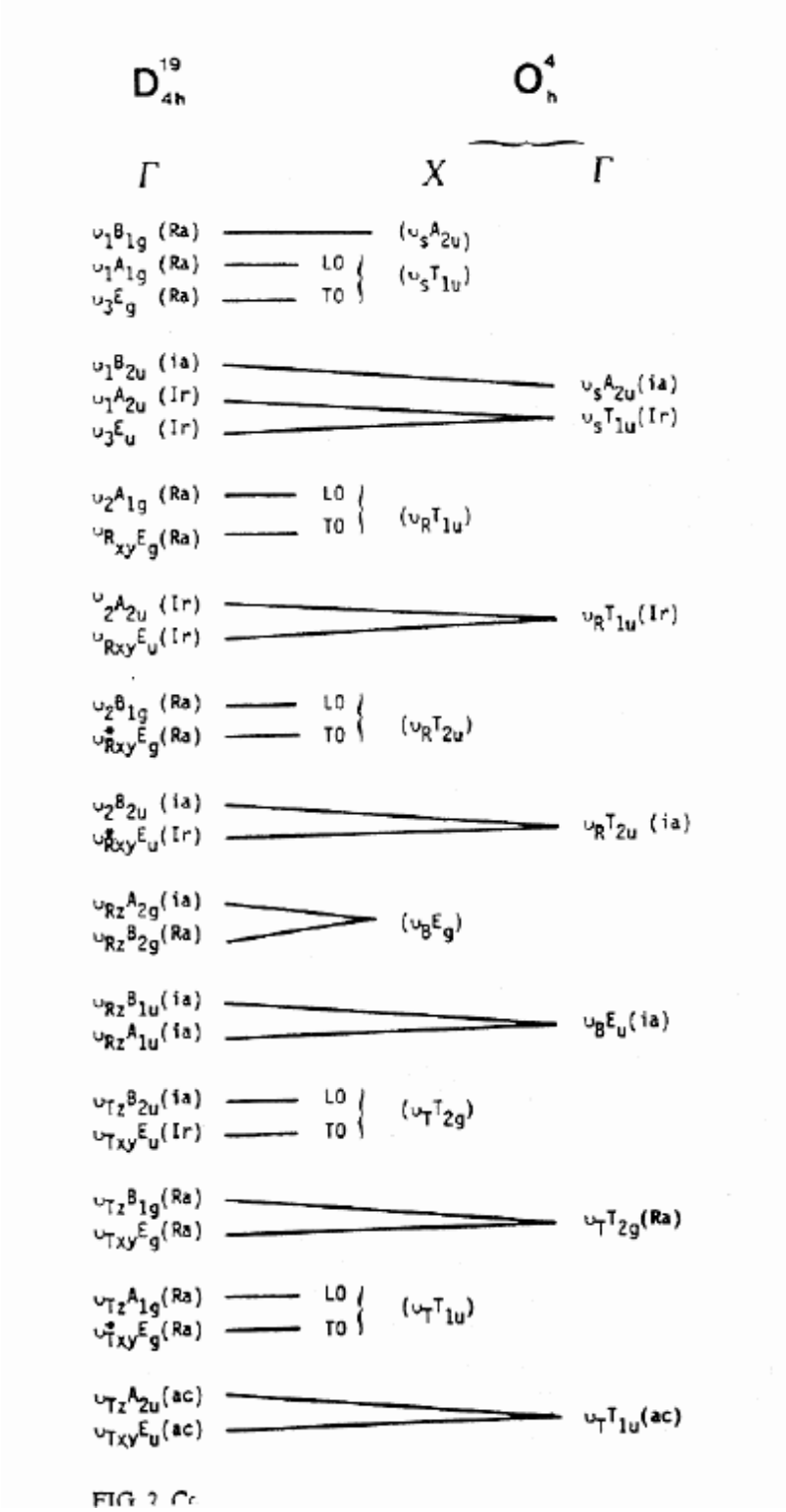

Figure 7.3.1: *Correspondences between the zone center modes of ice VIII (D_{4h}^{19}) and the zone center and X-point boundary modes of ice X (O_h^4). The symmetry assignments given in parentheses at the X point indicate the mode symmetry at the zone center of the phonon branches. (Picture from Ref.[33]).*

water molecules. Keeping this OO distance fixed and forcing the proton to move to the other oxygen atom, it has to overcome an energy barrier with a maximum at the centro-symmetric configuration, which leads to a double-well potential with a high barrier. This barrier to proton transfer, however, decreases with decreasing OO separation, as it is shown in (b) and (c). In the limit of very short OO separations, the proton resides preferentially midway between the two water molecules (d), leading to a single-well potential [101]. Thus, this centro-symmetric configuration (d) is an energy minimum for short OO separations, and a transition state for large separations. This correlation was also found experimentally.

Many essentials of proton transfer and conduction can be traced back to the particular regime in the sequence (a)-(d) of Fig.7.4.1 as governed by the OO separation. However, it is experimentally difficult to study in a controlled way the properties of hydrogen-bonded systems as a function of the OO separation. High-pressure ice is a system that is experimentally accessible under controlled conditions by present-day diamond anvil cell techniques. In addition, the three ice modifications VII, VIII, and X have essentially the same structure of the oxygen sublattice (bcc or close to bcc in the case of ice VIII), but they show a very different behavior concerning the proton positions, as already discussed. Applying hydrostatic pressure at constant temperature allows one to vary continuously the OO distance while simultaneously measuring properties.

This is a dramatic simplification as compared to hydrogen-bonded solids at ambient pressure, systems in the gas or liquid phases, or even 'biomolecules'. Thus, ice at high compression is an ideal candidate for performing experiments where the proton transfer potential can be tuned as a function of the applied external pressure, i.e. without changing the chemical composition of the solid. In particular, the phases (b) and (c) are very interesting; this regime is called "low-barrier H-bond" [102] and plays a very important role in very complex biological substances, for example in

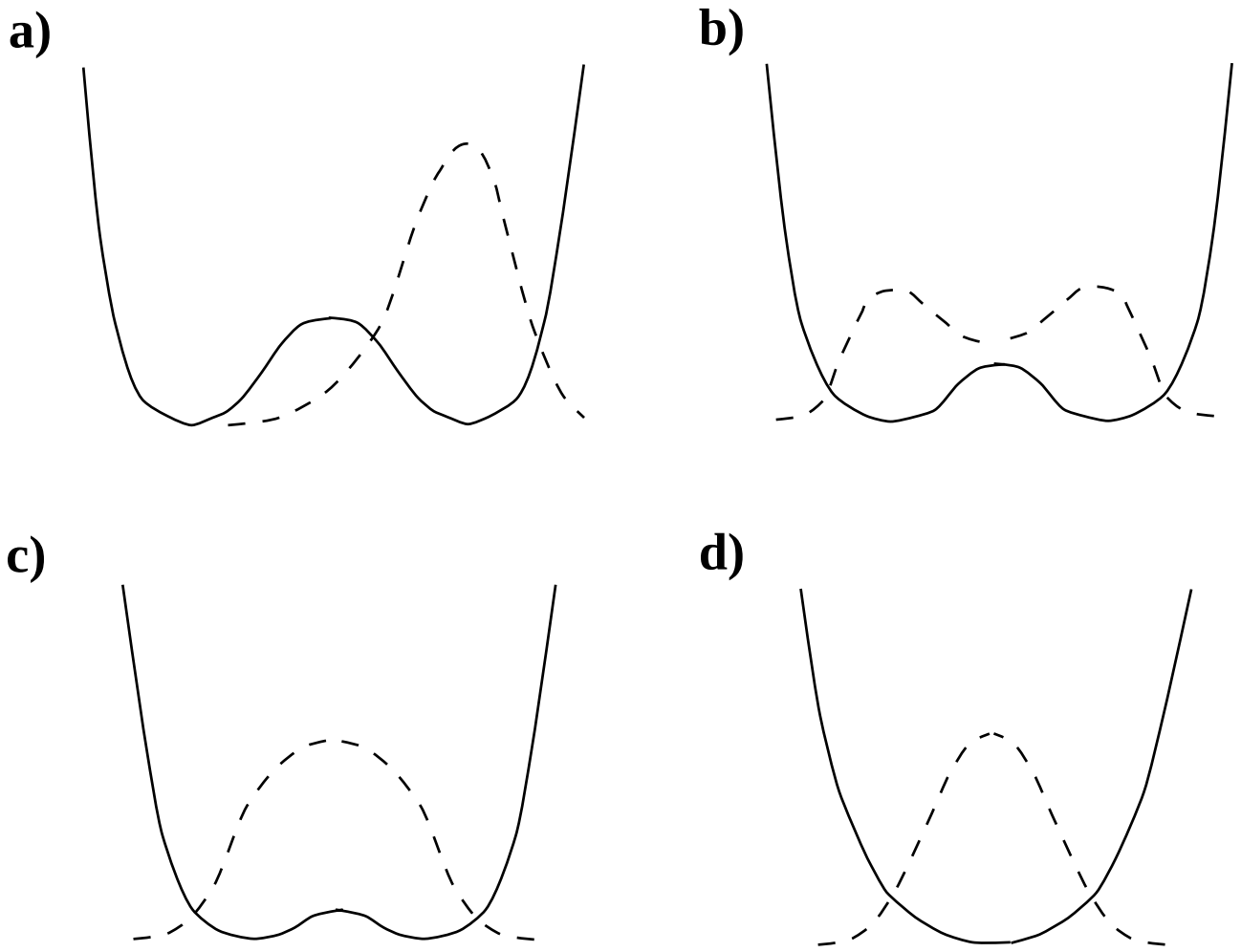

Figure 7.4.1: *Schematic schetch of the adiabatic electronic potential energy profile (solid lines) and the corresponding proton densities (dashed lines) for proton transfer. (Picture from Ref.[101])*

the HIV enzyme [28].

7.5 Path Integral Molecular Dynamics

The picture of the proton transfer, described in the previous section, has recently been confirmed by *ab initio* path integral molecular dynamics simulations [44] where the proton is treated as a quantum particle.

In this approach, the symmetrization of the hydrogen bond is followed in Fig.7.5.1 by monitoring the evolution of the quantum-statistical average of the shortest oxygen-hydrogen bond length R_{OH} as a function of the nearest-neighbor oxygen- oxygen distance R_{OO} (which in turn is a function of the pressure), the signature of the symmetric ice simply being $R_{OH} = R_{OO}/\,2$ (solid line). In Ref.[44] the authors find that this relation is approximatively linear in the low pressure regime, which has been also found by neutron scattering up to 20 GPa [39]. On compression, however, the lengthening of the R_{OH} bond becomes much more pronounced as a function of decreasing R_{OO}. The quantum system (filled circles) finally undergoes a symmetrization transition at $\sim$ 72 GPa, whereas in the corresponding classical system (open circles) a much higher pressure of $\sim$ 102 GPa is needed to observe the transition. Ice VIII does not transform directly into symmetric ice: in the quantum simulation there is clear evidence that proton-disordered molecular ice VII exists between proton-ordered ice VIII at lower pressures and symmetric non-molecular ice X at higher pressures. In fact, it is possible to analyze the average proton distribution $P(\delta\ , R_{O_aO_b})$ as a function of the proton position relative to the bond midpoint $\delta\ = R_{O_aH} - R_{O_bH}$ and the corresponding oxygen-oxygen separation $R_{O_aO_b}$, which is shown in Fig.7.5.2. The quantum simulations (a),(b) and (c)+(d) clearly correspond to ice VIII, VII and X, respectively. In ice VIII (a) the quantum fluctuations only induce a zero-point motional broadening of the distribution relative

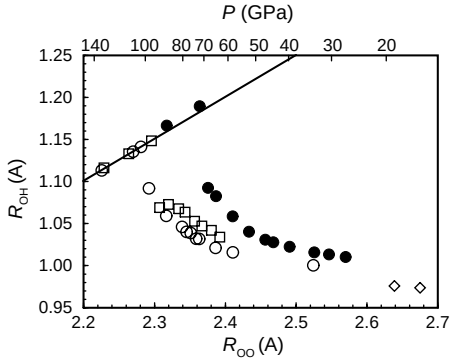

Figure 7.5.1: *Filled circles: quantum nuclei at 100 K; open squares: classical nuclei at 300 K; open diamond: experimental* (R_{OO}, R_{OH}) *data about 240 K (Ref.[39]);solid line: "symmetrization line"* $R_{OH} = R_{OO}/2$*, indicating ice X. (Picture from Ref.[44])*

to the classical case (e) without effecting its shape. Dramatic are the quantum effects in ice VII (b), where the proton tunneling along the hydrogen bonds is totally absent in the classical case (f), that leads to proton disorder and thus to a bimodal distribution. Finally in ice X (c) the distribution is broad and flat, but unimodal and centered at $\delta = 0$ that sharpens considerably upon further compression (d). In contrast the classical calculation (g) is characterized by a bimodal distribution reflecting an underlying double-well proton transfer effective potential. Taking into account that the thermal fluctuations correspond to the same temperature in (c) and (g), it is a zero-point motion effect which shifts the lowest vibrational level of the proton wavefunction above the double-well barrier. This form of ice (c) could be dubbed "proton-disordered symmetric ice" with delocalized protons since the proton distribution is very broad, cover both potential wells, but nevertheless peaks at the bond midpoint $\delta = 0$. Only at higher compression exceeding about 102 GPa there is a single well (h) with the potential minimum right at the center position $\delta = 0$, which in turn could be called "proton-ordered symmetric ice" (d) with localized protons at the bond midpoints. We finally note that the classical treatment of the

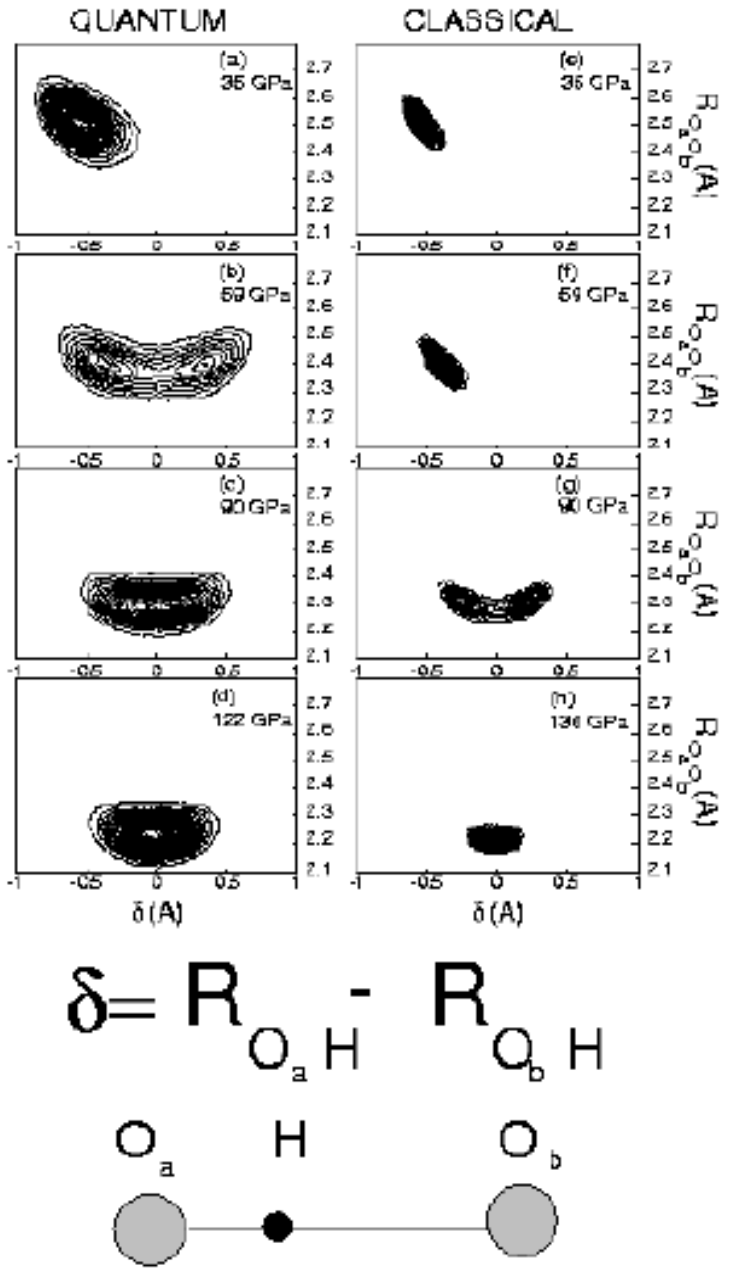

Figure 7.5.2: *Contour plots of the average proton distribution function $P(\delta, R_{O_aO_b})$ as a function of the proton position relative to the bond midpoint $\delta = R_{O_aH} - R_{O_bH}$ and the corresponding oxygen-oxygen separation $R_{O_aO_b}$ for quantum (left panels) and classical (right panels) simulations at several representative volumes and 100 K; note that $\delta = 0$ corresponds to the proton being located midway between its neighboring oxygen atoms O_a and O_b irrespective of the actual $R_{O_aO_b}$ distance (Picture from Ref.[44])*

proton reproduces the qualitative features of the phase transition, the main effect of quantum fluctuations and tunneling being a shift to lower pressures of the VIII-VII and VII-X phase boundaries.

7.6 Infrared absorption

In the following section recent results obtained by IR experiments and simulations will be discussed.

7.6.1 Infrared experiments

The development of new spectroscopic techniques based on the use of synthetic diamond anvils, shown in Fig.7.6.1, have made possible to investigate spectroscopic properties of materials at high pressure.
The experiments reported in this thesis were performed in the Geophysical Laboratory and Center for High Pressure Research in Washington DC by A.F. Goncharov, V.V. Struzhkin, H. Mao, and R.J. Hemley. The new techniques developed in this group allows to study materials under very high pressures in the range also of 100 GPa.
In fact, there are two main difficulties. First, the O-H stretching modes are so intense that the absorbance maxima typically saturate for sample thickness appropriate for measurement of bulk absorption properties. Second the transmission through the diamond anvils is 0.05% in the region of second-order diamond absorption ($1900 - 2100$ cm^{-1}), precluding measurements in a crucial spectral region. These difficulties were resolved by measuring both reflectivity and absorption with an intense syncroton infrared source, combined with the use of thin anvils allowing 3% transmission in the diamond second order absorption region. Reflectivity

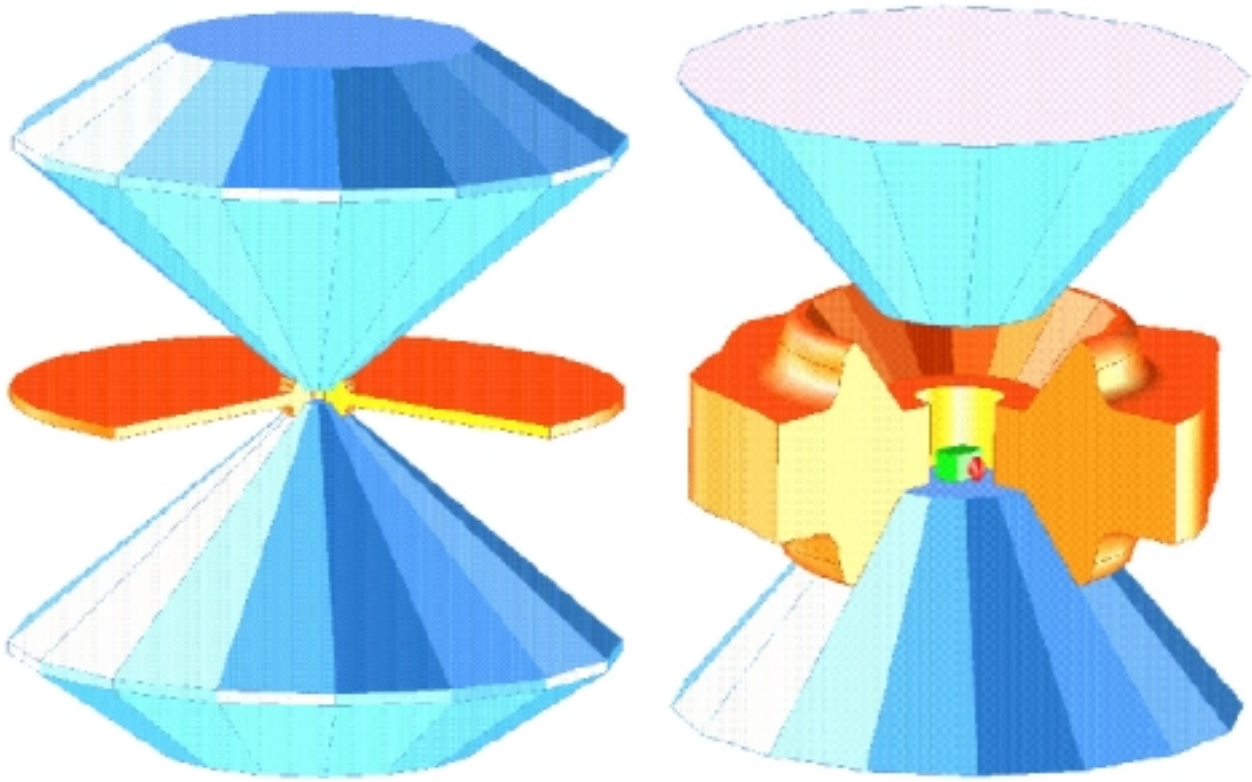

Figure 7.6.1: *Diamond anvil cell. The high pressure chamber usually consists of a 30 to 300 μm hole drilled in the metal gasket (schematically depicted in orange). Small chips of ruby are placed in the chamber for in situ pressure determinations. Samples are loaded with a transmitting medium, consisting of a condensed gas or fluid. Rare gas such as argon and neon have been shown to produce quasi-hydrostatic conditions to pressures above 80 GPa and are particularly useful because these materials lack a first order Raman spectrum in the solid state and hence do not contribute to the background signal. The scattered light is observed through a small hole at the top and the bottom of the cell using a microscope.*

measurements were used in order to identify strong feature, while absorption measurements are ideal for weaker features.
These recent infrared measurements, published in Ref.[40,41] and shown in Fig.7.6.2 and 7.6.3, have provided evidence for the phase transition from ice VII to ice X beginning at 60 GPa and stable to at least 210 Gpa. Such infrared reflectivity measurements demonstrate that the softening of the O-H stretching modes, previously documented at lower pressure [33,35], is profound in this pressure range.

The frequencies of the IR modes decrease from 3150-3220 cm^{-1} (ice I at zero pressure) to ~ 150 cm^{-1} at 60 GPa (in ice VII) followed by a hardening of the stretching mode at higher pressure.
This result provided evidence for the transition to the nonmolecular phase with symmetric hydrogen bonds. However, there is still a lot of incertitude in the determination of the boundaries between ice VII and the nonmolecular phase, supposed to be ice X. It is only sure that such a phase exists at very high pressures.
Furthermore, there is no way to obtain the IR spectra in the region of absorbance of the diamond anvil cell (dot-line in Fig.7.6.4) and the window of frequencies accessible with these experiments do not include the low frequency range.

It is also important to mention that the broad peaks present at high pressure force the harmonical analysis to be only a qualitative tool for the interpretation of the data. For all these reasons, in order to validate the data and perform an accurate analysis one should take recourse to *ab initio* simulations.

7.6.2 *Ab initio* simulations

In order to validate the experimental data, *ab initio* calculations of the infrared spectrum were done by M. Bernasconi et al. [43].

The simulations were performed using *ab initio* molecular dynamics, where the pro-

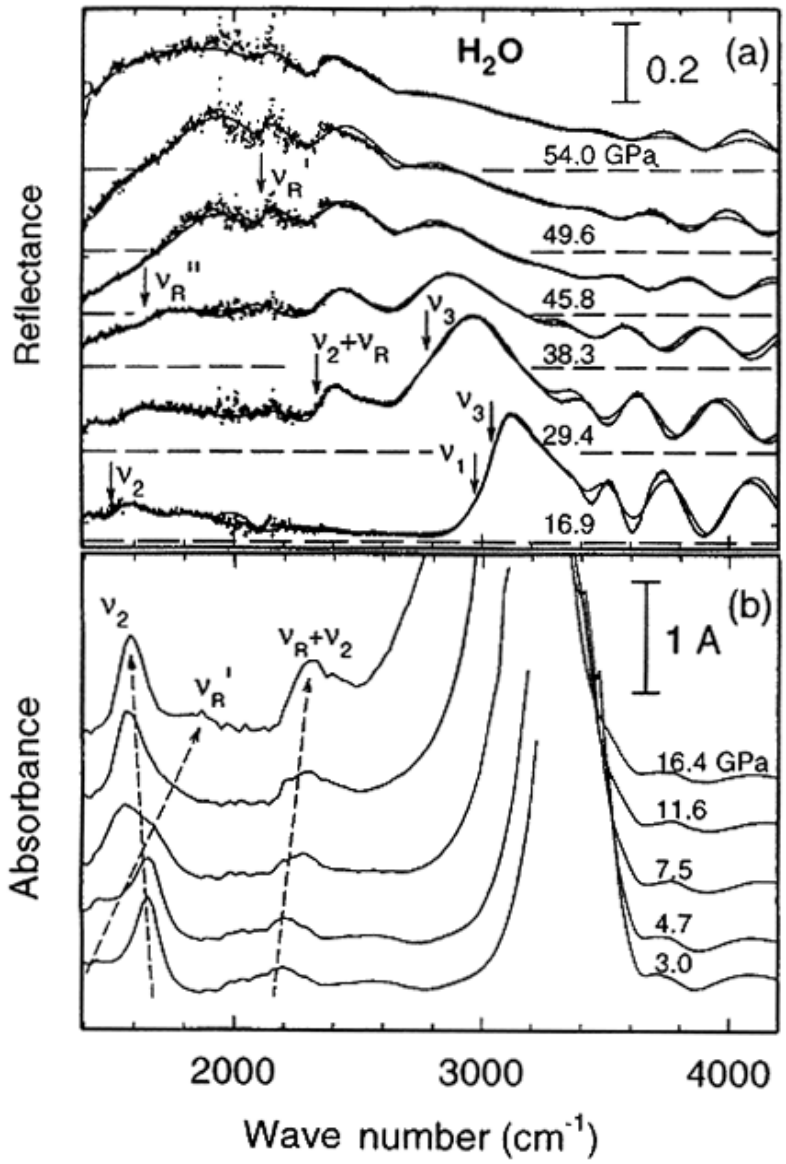

Figure 7.6.2: *Syncroton infrared spectra of H_2O at 3-55 GPa and 300 K. (a) Reflectivity spectra. Solid lines are oscillator fits; dashed line are zero lines for the corresponding reflectivity spectra. (b) Absorbance spectra. The oscillation at high frequency are interference fringes created by the diamond cell. Dashed lines with arrows are guides to the eye. (Picture from Ref.[41])*

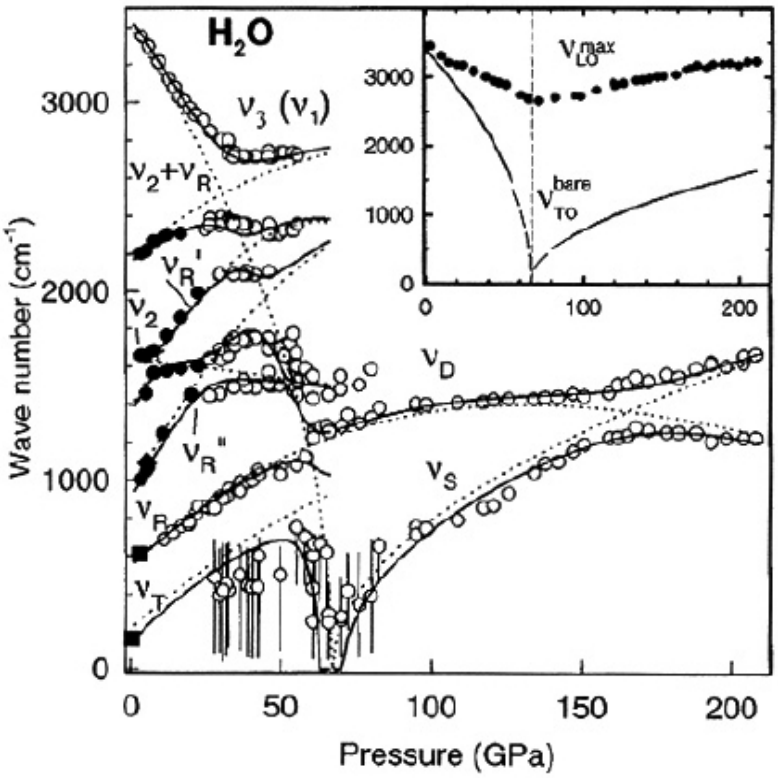

Figure 7.6.3: *Vibrational frequencies for H_2O up to 210 GPa. Closed circles, absorption spectra. Solid lines are fits to the multiple Fermi resonance model, and the dot lines are bare frequencies. Inset: Closed circles show the variation of the highest LO frequency with pressure; solid and dashed lines correspond to the bare TO frequency. (Picture from Ref.[41])*

tons are treated classically. Also the imaginary part of the dielectric function $\epsilon_2(\omega)$ was calculated in the classical limit from the formula [103]

$$\epsilon_2(\omega) = \frac{2\pi\omega}{3V\,k_B T}\int_{-\infty}^{\infty} dt\; e^{-i\omega t}\,\langle \mathbf{M}(t)\cdot\mathbf{M}(0)\rangle \qquad (7.6.1)$$

where V is the volume, k_B the Boltzmann constant, T the temperature, $\mathbf{M}$ the total dipole moment of the sample and the angular brackets indicate the statistical average. The correlation function $\langle \mathbf{M}(t)\cdot\mathbf{M}(0)\rangle$ was computed directly in the MD simulation. The electronic contribution to $\mathbf{M}$ is computed by using the Berry phase scheme.

As already discussed, a classical treatment of the protons reproduces the qualitative features of the phase transitions, the main effect of the quantum fluctuation and tunneling being a shift to lower pressures of the VIII-VII and VII-X phase boundaries. Bernasconi et al. [43] have checked the validity of their approximation looking at the classical distribution function of the proton position along the $\mathrm{O}--\mathrm{H}\cdots\mathrm{O}$ bond in the VIII, VII and X phases, illustrated in the left-hand panels of Fig.7.6.4. The *ab initio* MD simulations [92] were performed at constant volume in a supercell containing 16 water molecules initially arranged in the ice VIII geometry. The small tetragonal distortion of ice VIII [39] has been neglected. Furthermore, the relaxation times for rotational disorder are rather large; in addition, as we have already discussed in Sec.7.2, the simulation cell used is too small to allow the creation of low-energy Bejerrum defects. This prevents Bernasconi et al. from observing a rotationally disordered ice VII and we can go directly only from ice VIII to translationally disordered ice VII at 300 K [43]. The authors of Ref.[43] used a gradient correction to the local-density approximation for the exchange energy part only in the form proposed by Becke [65]. This choice has been shown to describe well the hydrogen bonding in water [67]. The conversion of the simulation cell volume to the pressure is based on the experimental equation of state [38]. As we have discussed

above, in order to take account of the classical treatment of the proton the results at such pressures should be compared with experimental data at lower pressures.

7.6.3 Analysis of the IR spectrum

The main features of the experimental spectra and their evolution with pressure are well reproduced by the calculations of Ref.[43], as can be seen in Fig.7.6.4.

By increasing pressure the intramolecular stretching modes ν_3 and ν_1 shift to lower frequency and merge with the librational mode ν_R. The resulting peak sharpens up at higher pressure and above 80 GPa a new peak appears at the lower boundary of the frequency window accessible experimentally. At pressure above 98 GPa the spectrum is characterized by two peaks ten times larger in intensity than the IR peaks at low pressure (13.7 GPa). The theoretical spectra reproduce well all these features and in addition fill the experimental gap in the IR spectra in the range 1800-2400 cm^{-1} and below 500 cm^{-1}, where a new strong peak is revealed by the simulation in the region of stability of ice VII.

At low pressure in ice VIII (below 50 GPa in the calculated spectra) the system is mainly harmonic and the attribution of the IR peaks to lattice modes is relatively simple. The spectrum at high frequency is characterized by three intramolecular vibrations: the symmetric (ν_1), and antisymmetric (ν_3) OH bond stretchings, and the OH bond bending (ν_2). In addition a librational mode (ν_R) and a lattice translational mode (ν_T) are IR active. The ν_T mode is an antisymmetric stretching of the two hydrogen bonds connecting a water molecule with two neighboring molecules. Its IR activity is due to the charge transfer associated with the antisymmetric H-bond stretching. A mode of similar origin has been identified in water at 165 cm^{-1}[111]. In the pressure range 70-80 GPa which corresponds to the region of stability of ice VII, the protons jump between the two sites of the double well potential. The sys-

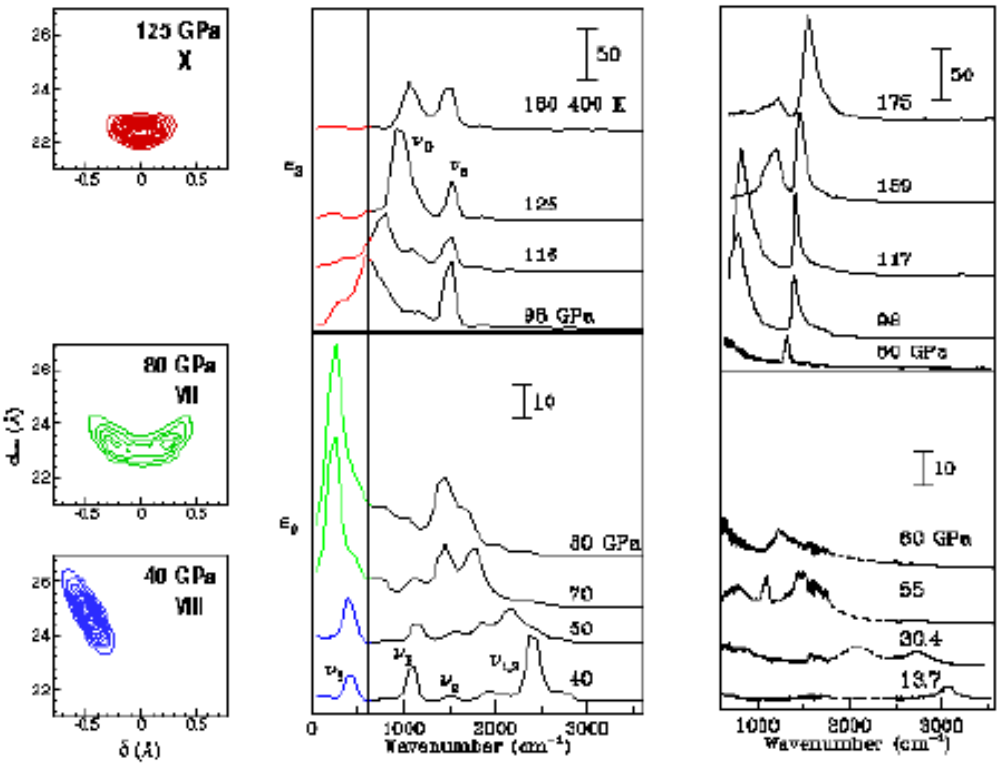

Figure 7.6.4: *Left panels: Contour plots of the average proton distribution function as a function of the proton position relative to the bond midpoint* $\delta = R_{O_aH} - R_{O_bH}$ *and the corresponding oxygen-oxygen separation* $d_{O_aO_b}$ *for the simulation at the three representative pressures and room temperature. Center panels: Theoretical IR spectra of* H_2O *computed at room temperature, but for the spectrum at 160 GPa which is computed at* 400 *K (see Ref. [43]) The vertical line represents the lowest frequency reported in the experimental data.*
Right panels: experimental [40] IR spectra of H_2O *at several pressures. The data at 13.7 and 30.4 GPa are recorded at 295 K, all others at 85 K. In the range of strong diamond absorption* ($1800 - 2400\ cm^{-1}$) *there are no experimental data. In this range the dashed lines are the result of a fit [40]. Since quantum tunneling of the protons, neglected in this simulation, is expected to reduce the transition pressures by 30 GPa, [44] the experimental data should be compared to the theoretical spectra at higher pressures. (Picture from Ref.[43])*

tem is strongly anharmonic and the attribution of the peaks in terms of the lattice dynamics is more difficult. The spectrum at 70 GPa in Fig.7.6.4 displays two broad peaks at 1450 cm^{-1} and 1750 cm^{-1} and a new strong peak around 250 cm^{-1}, outside the frequency window experimentally accessible, but which can possibly be seen as a very strong rise in intensity at the lowest accessible frequencies in the experiments. A calculation based on the harmonic approximation for the phonons and on the use of effective charges to evaluate the IR activity fails completely to reproduce such a spectrum. Anharmonicities are essential and can be due to anharmonicity in the lattice dynamics and/or in the effective charges. The effect of the former was evaluated in Ref.[43]: it gives two bands at $\sim$ 1400 cm^{-1} and $\sim$ 1700 cm^{-1} in reasonable agreement with the position of the two higher peaks, which are therefore proton disordered broadened harmonic modes. The nature of the peak at 250 cm^{-1} is different. A clue as to the nature of this peak is provided by the isotope effect. In fact in the calculated IR spectrum of D_2O at 80 GPa the 250 cm^{-1} peak does not show isotope shift. This implies that the peak is mostly due to lattice modes of the oxygen atoms. In ice VII at 70-80 GPa the modes which modulate the O-O distance are strongly coupled to the proton jumps between the two sites of the double well potential. Selection rules for IR activity break down due to proton disorder and the anharmonicity of the effective charges enhances the IR intensity of these particular lattice modes.

Above 98 GPa the spectra reproduce the sharpening of the highest frequency peak (ν_S) and the appearance of a new stronger low frequency peak around 800 cm^{-1} (ν_D). The magnification by a factor of ten of the peak intensity at high pressure is also well reproduced. The intensity of the peaks are very sensitive to quantum effects of the protons and the introduction of quantum corrections [110] change peak intensities by up to a factor of two.

The ν_D mode does not evolve into the 250 cm^{-1} mode characteristic of ice VII. In

fact at 98 GPa both the ν_D and the 250 cm^{-1} modes coexist. In this pressure range the system is ice X. Ref.[43] therefore confirms that the presence of the two strong IR peaks is a signature of the symmetric H-bond as suggested by K. Aoki et al. in Ref. [100] and by A.F. Goncharov et al. in Ref.[40]. The experimental spectra show an intensity exchange between the two peaks above 117 GPa. This feature has been attributed to a Fermi resonance due to anharmonic coupling between the two modes.

In the simulated spectra at 220 K this intensity exchange has not been observed, probably because of the underestimation of the anharmonicity due to the neglect of quantum fluctuations. If, as a way of increasing the anharmonic interaction, the IR spectrum is calculated at 400 K, it reproduces the observed intensity exchange. Due to the limited frequency resolution the authors of Ref.[43] were not able to identify the cascade of Fermi resonances discussed in Ref. [41].
In conclusion, IR experiments and *ab initio* simulations allow to identify the fingerprints of the VIII $\rightarrow$ VII and VII $\rightarrow$ X transformations in ice at high pressure.The two-peak spectrum at high pressure is characteristic of ice X. Moreover, the simulations predict that a strong IR peak at 250 cm^{-1} should be the signature of the transition to ice VII. Since molecular ice VIII is first transformed into disordered ice VII via proton jumps and tunneling, the symmetrization transition is mainly order-disorder in character. This feature explains the large damping of the soft mode close to the transition reported experimentally [40,41].

7.7 Raman scattering

The analysis of the IR spectra, presented in the previous pages, indicates the presence at very high pressure of a nonmolecular phase, which is supposed to be ice X. In order to complete this analysis, Raman spectroscopy is a very useful tool and

in the following we will present the experiments and the first application of the *ab initio* method developed in this thesis.

7.7.1 Raman experiments

High pressure Raman spectra experiments are still more difficult than the IR experiments described in the previous pages. Only very recently [104], in the Geophysical Laboratory and Center for High Pressure Research in Washington DC, A.F. Goncharov, V.V. Struzhkin, H. Mao, and R.J. Hemley proposed a new experimental setup, which allows to obtain, also for Raman scattering, data at very high pressure, of the order of 100 GPa.

In fact, the principal difficulty in the high pressure Raman studies of ice is the presence of background luminescence and Raman scattering from the diamond anvils, which is normally much stronger than the weak Raman signal from the sample. Because of such very low scattering cross sections of the materials at these pressures, the results of Raman spectra obtained in the past were controversial [109]. This problem was overcome by use of high-purity synthetic diamond anvils in an optical configuration that substantially suppresses the luminescence and spurious Raman signals as well as effects of pressure gradients on the spectra.
However, all these techniques require the use of several different spectrometers in different regions of frequencies. Furthermore, the subtraction of the diamond anvil signal induces strong errors and results in the regions of frequency which correspond to the excitations of the diamond anvils are not accurate.
In Fig.7.7.1 we have reported a scheme of the experimental setup used for Raman experiments.

In 1999, thanks to the introduction of these new spectroscopic techniques, A.F. Goncharov et al. [42] performed Raman experiments on ice in the range of pressures

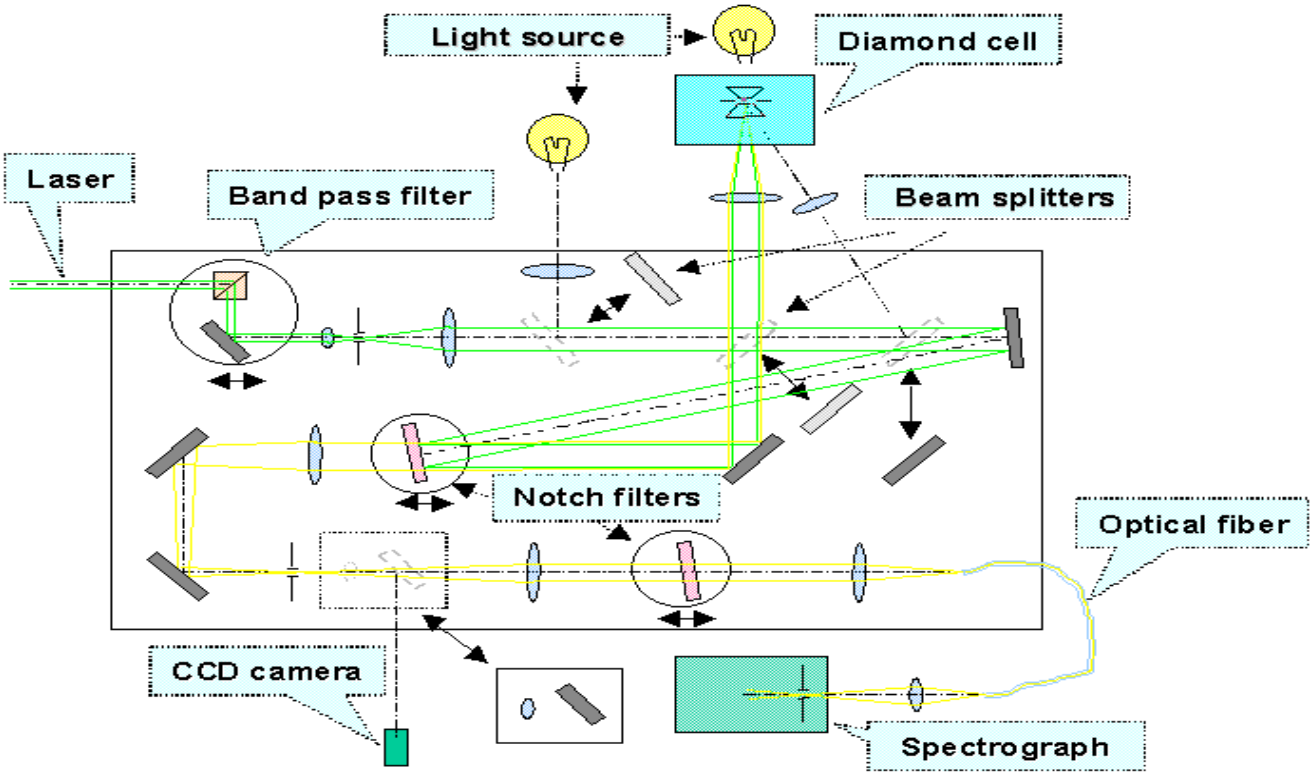

Figure 7.7.1: *Experimental setup for high pressure Raman scattering at the Geophysical Laboratory and Center for High Pressure Research in Washington.*

20-128 GPa. The spectra obtained are reported in Fig.7.7.2 and 7.7.3. In order to interpretet these data, the experimentalists used a multiple coupled oscillator model to the observed Raman modes. This kind of approach was introduced in 1971 by R.S. Katiyar [107]; in the following we give a short summary of it.

7.7.2 Coupled modes model

The spectra can be determined from the imaginary part of the complex susceptibility for the coupled modes in terms of the corresponding Green's function G and mode strengths (plasma frequencies) ω_p. The inverse of the frequency-dependent Green's function of a single oscillator is $G_{ii}^{-1}(\omega) = \Omega_i^2 - \omega^2 - i\omega\gamma_i$ (where Ω_i is i'th oscillator frequency and γ_i its damping constant); the inverse Green's function of the system of coupled oscillators is given by:

$$G^{-1}(\omega) = ||G_{ii}^{-1}(\omega)|| + ||\Delta_{ij}^2||, \tag{7.7.1}$$

where $||G_{ii}^{-1}||$ is a matrix having single oscillator inverse Green's function on the diagonal and non-diagonal terms equal to zero, and $||\Delta_{ij}^2||$ is a non-diagonal matrix with coupling strengths between the oscillators i and j and diagonal element equal to zero. The response of the system of such a coupled oscillators in terms of $G(\omega)$ is given by

$$I(\omega) = \mathrm{Im}(\sum_{ij} \omega_p^i G_{ij}(\omega) \omega_p^j). \tag{7.7.2}$$

The observed spectra were fitted in this scheme by a superposition of the soft mode and a number of oscillators that are either coupled or uncoupled to it. These bands include deformational (ν_2), translational and rotational modes, and their combinations. Fits of the frequency shifts of the modes at lower pressure were used to probe the coupling with the soft mode at higher pressures. The parameters of the model were determined by fitting the model to the measured spectra. This procedure gave

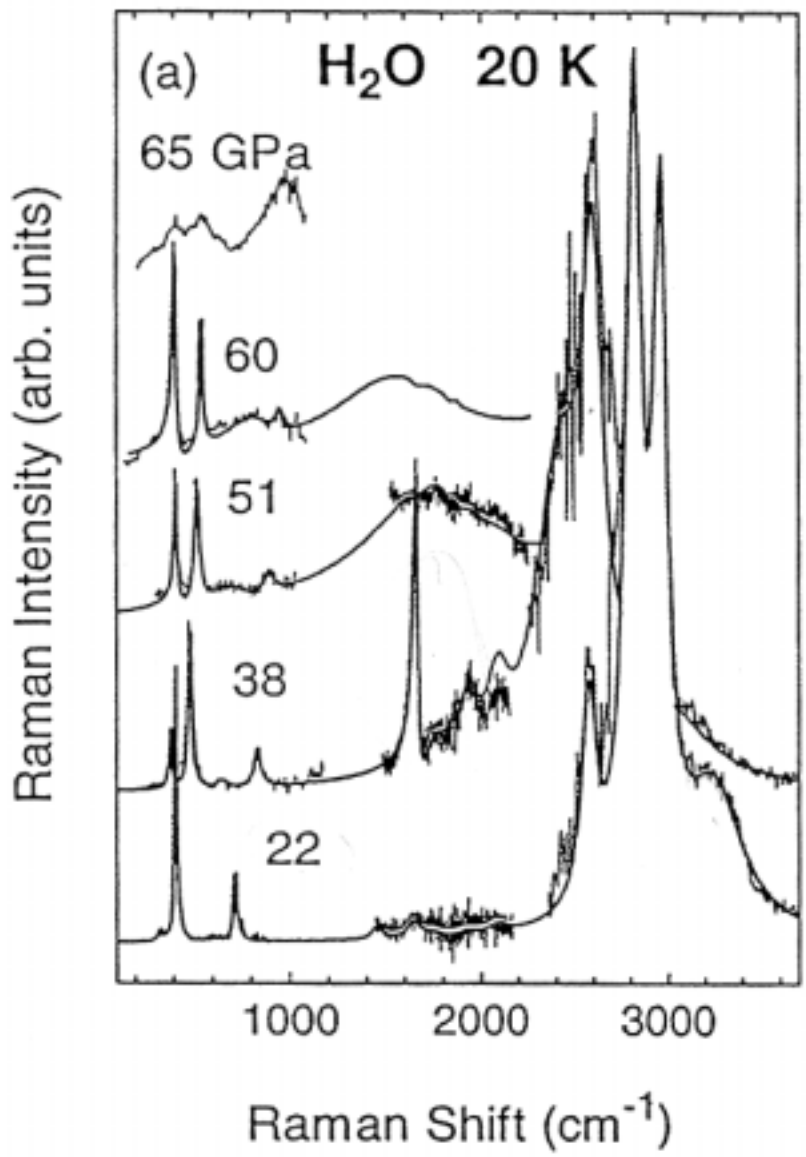

Figure 7.7.2: *Representative Raman spectra at 22-65 GPa and 20 K. The points are experimental data. First and second order Raman signals from the diamond anvils are subtracted. The lines represent the results from the coupled oscillator model. The data in the* $1700 - 2200\ \mathrm{cm}^{-1}$ *range were measured with higher resolution and hence have a lower signal/noise ratio. (Picture from Ref.[42])*

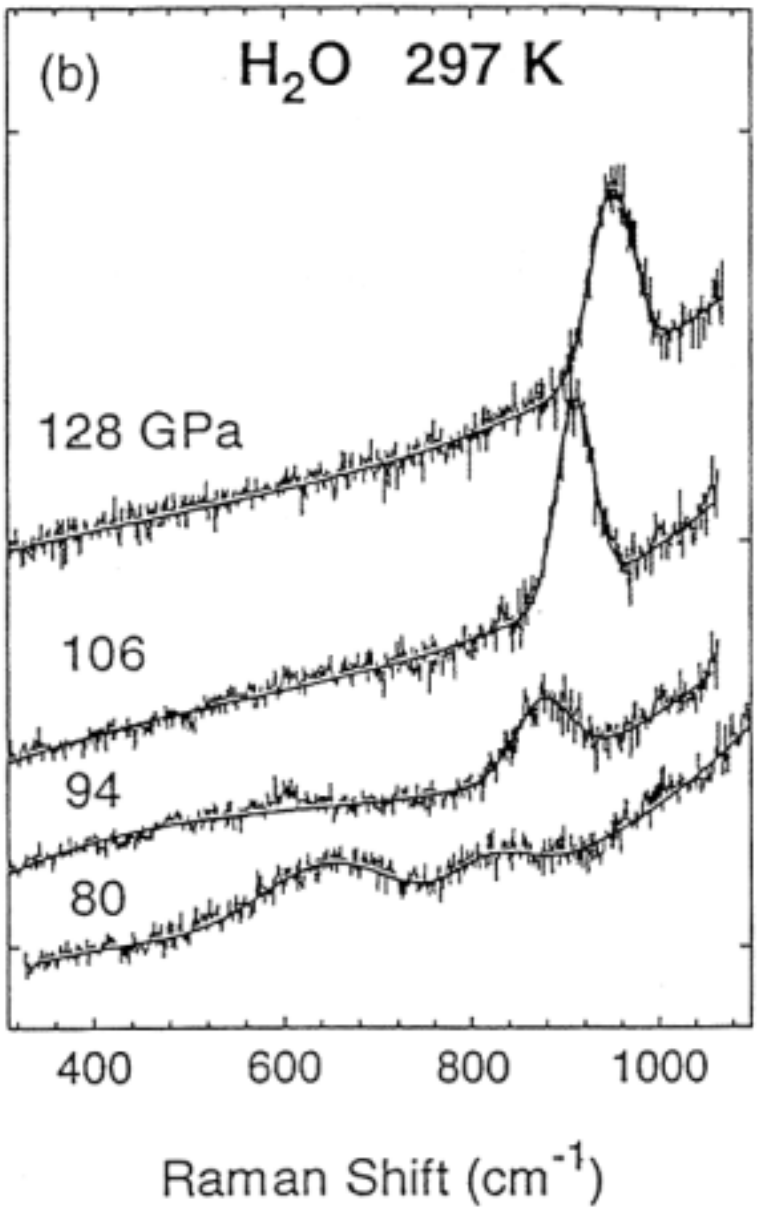

Figure 7.7.3: *Raman spectra of ice at 70-128 GPa and room temperature. The line is a phenomenological fit.(Picture from Ref.[42])*

the pressure dependence of mode parameters. The assignment of the peaks obtained is reported in Fig.7.7.4 and discussed in more details in Sec.7.7.3.

7.7.3 Experimental data

As already observed in the previous pages, the behavior of ice VIII is mainly harmonic and the attribution of the peaks is relatively simple and was done [42] through the multiple coupled oscillator model, described before (see also Fig.7.7.4).
At low pressure the spectrum of ice VIII is dominated, like the IR spectrum, by the high-frequency O-H stretching vibrations: they form a triplet (a doublet and a small shoulder), which has been assigned to $\nu_1(A_{1g})$, $\nu_3(E_g)$, and $\nu_1(B_{1g})$ modes in order of increasing frequency. These modes soften with pressure. Despite the merging with the second order band from the diamond anvils at 22 GPa, the experimentalists were able to track the behavior of these bands by subtracting the signal from the diamond taken as a reference at 17GPa. The high-frequency $\nu_1(A_{1g})$ band has the largest pressure shift. As this mode decreases in frequency, the intensities of the other bands are enhanced sequentially from higher to lower frequency to produce prominent resonances, which appear and disappear as the pressure increases. The most notable is the resonance at 38 GPa in the region (1650 cm^{-1}) where the results of the experiments are more uncertain because of the presence of the signal of the diamond-anvil cell. In the low frequency range and at low temperature the spectrum is dominated by the sharp translational bands assigned to the $\nu_{T_z}(A_{1g}) + \nu_{T_{xy}}(E_g)$ and $\nu_{T_z}(B_{1g}) + \nu_{T_{xy}}(E_g)$ excitations at 400 and 500 cm^{-1}; they exhibit only minor frequency shifts at 45-60 GPa, soften and broaden just above 60 GPa and then increase in frequency with pressure. Changes are also observed near 60 GPa in a broad band at 700 cm^{-1}, which appears only at high pressure. At $T \geq 100$ K the broad translational band of ice VII at 500 cm^{-1}, which correlates with the $\nu_{T_z}(B_{1g}) + \nu_{T_{xy}}(E_g)$ band of ice VIII, evolves into a doublet. The changes

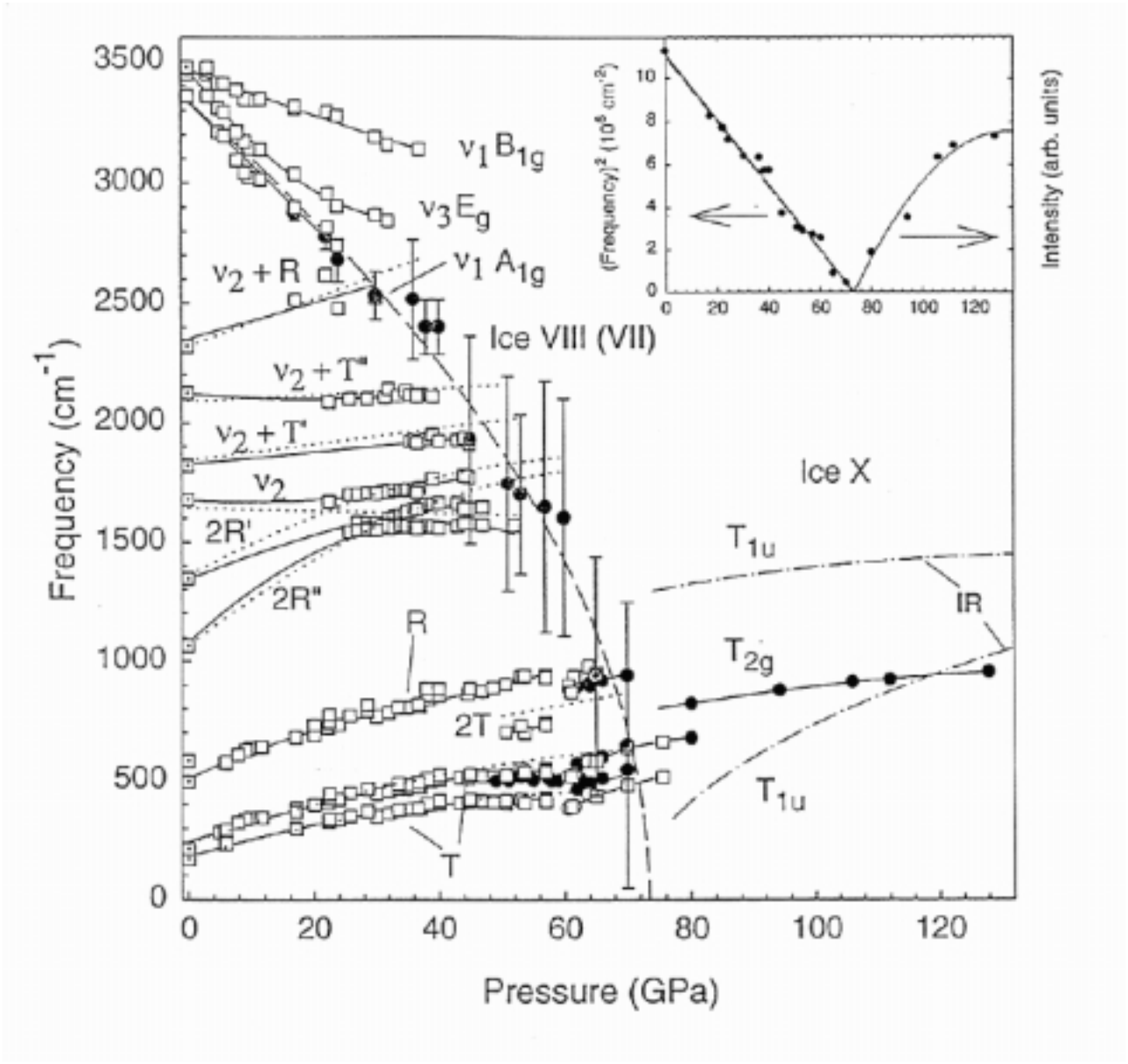

Figure 7.7.4: *Raman frequencies of* H_2O *to 128 GPa. Changes in intensities and pressure dependences of the lower frequency modes are observed at 60 GPa and* $\sim$ *80 GPa, as described in Ref.[42]. The open squares are measured frequencies at 20 K; black circles correspond to room temperature. The observed frequency shifts are indicated by the solid lines. The low-pressure data* ($\leq$ *30 GPa) agree with the previous measurements (Refs.[33]). The ambient pressure data (dotted open squares) are from Ref.[105]; the high pressure IR data (dot-dash lines) are from Ref.[40]. The dotted lines are the bare frequencies obtained from the coupled oscillator model for ice VIII. Details of the model are presented in Ref.[42]. The assignment of combination of bands is tentative. Inset: Pressure dependence of the square of the soft mode frequency and intensity of the single peak in the high-pressure phase (points and solid line). The dashed line is the extrapolation of the soft mode based on lower pressure measurement. (Picture from Ref.[42]).*

near 60 GPa becomes less pronounced as the temperature increases: the linewidth of the lowest frequency band of the doublet increases with the temperature, and both lower band tend to increase in frequency (Fig.7.7.4) and become an unresolved doublet at room temperature. The intensity of the rotational band gradually decreases and disappears in approximately the same pressure range. Further increase in pressure produces a major alteration in the spectrum. At 80-90 GPa, a new narrow band (Fig.7.7.3) appears, while all the other excitations appear to weaken. The frequency of this new excitation increases with pressure, with little qualitative change in the spectrum between 100 and 128 GPa. This new band is identified as the T_{2g} O-O vibration, as expected for the Cu_2O structure.

7.7.4 *Ab initio* simulations

In order to be able to reproduce the experimental spectra of strongly anharmonic systems, we have used the method illustrated in Chap.6 (see Fig.6.4.1).
We performed MD simulations [92] of 16 water molecules initially arranged in the ice VIII supercell geometry. As we have already mentioned in Sec.7.2, the small tetragonal distortion of ice VIII [39] can be neglected[1]. Furthermore, the relaxation times for rotational disorder are rather large; in addition, our simulation cell is too small to allow the creation of low-energy Bejerrum defects. This prevents also in the case of Raman simulations from observing a rotationally disordered ice VII and we can go directly only from ice VIII to translationally disordered ice VII at 300 K. We used BLYP gradient correction [65,66] to the local density approximation which describe well the hydrogen bond in water[67]. We have used Martins-Trouillers norm conserving pseudopotentials [74] and an integration time step of 0.12 fs. The

[1]Our resulting system is cubic and consequently has more symmetries than the real one. However, in the following for the description of the normal modes, we will continue to use the nomenclature relative to the tetragonally distorted system.

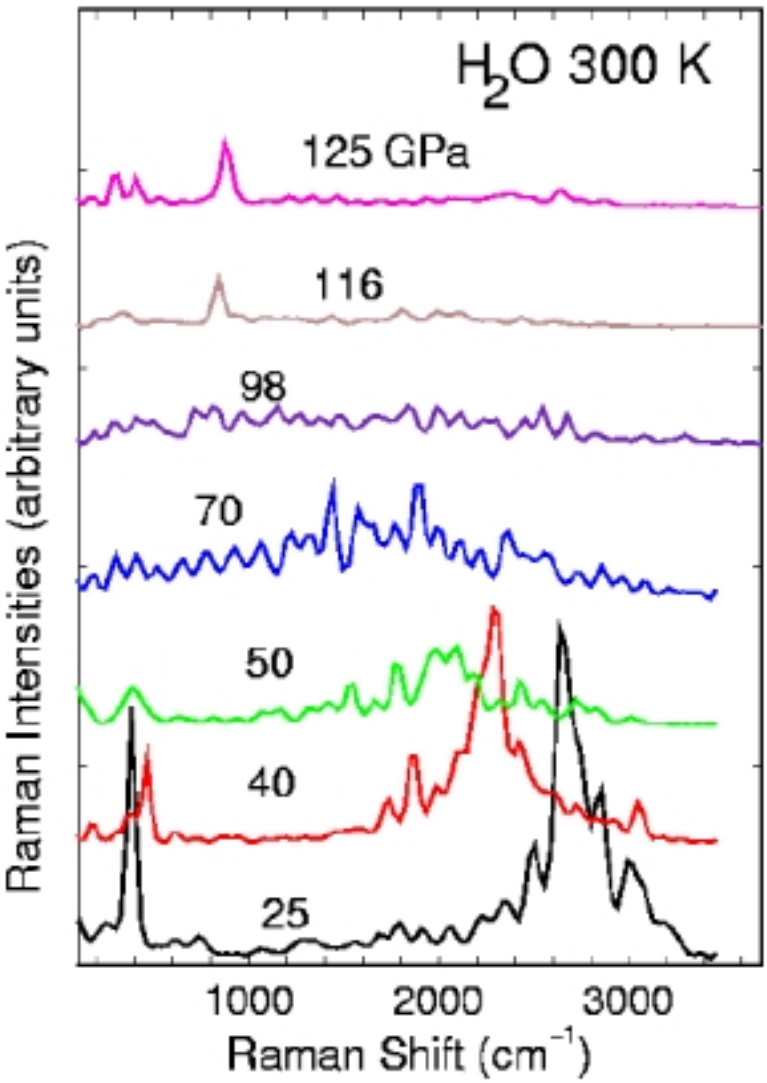

Figure 7.7.5: *Raman spectra of high pressure ice by ab initio simulations. At low pressure the spectrum of ice VIII is dominated, like the IR spectrum, from the high-frequency O-H stretching vibrations: they form a triplet (a doublet and a small shoulder), which has been assigned to* $\nu_1(A_{1g})$, $\nu_3(E_g)$, *and* $\nu_1(B_{1g})$ *modes in order of increasing frequency and soften with pressure. In the low frequency region, then appears only a broad translational band* $\nu_{T_z}(B_{1g})+\nu_{T_{xy}}(E_g)$, *as also reported in the experiments [42]. The spectrum in the range of pressure of 70-100 GPa is broad and no particular mode can be distinguished: the system is completely disordered and its Raman spectrum gives a confirmation of this effect. With increasing pressure a new band appears, while all the other excitations appear to weaken. This new band is identified as the* T_{2g} *O-O vibration, as expected for the* Cu_2O *structure.*

electronic wavefunctions $\{\psi^{(0)}\}$ and their linear order response to the perturbation $\{\psi^{(1)}\}$ were expanded in plane waves up to a cutoff of 70 Ryd. The Brillouin zone sampling was restricted to the Γ point. We performed constant volume simulations at different densities corresponding to pressures from 20 to 125 GPa. The conversion of the simulation cell volume to the pressure is based on the experimental equation of state [38]. Microcanonical runs up to 7 ps long were performed at the average ionic temperature of $\sim$ 300 K. The correlation function $\langle \alpha(0)\,\alpha(t) \rangle$ is computed classically and quantum effect corrections are taken in account multiplying Eq.(6.2.3) by the factor $[1 - \exp(-\hbar\omega / K_B T)]/\ 2$ [110].

7.7.5 Analysis of the Raman spectra

The simulated spectra are in good agreement with the experiments performed by A.F. Goncharov et al.[42], as can be seen in Fig.7.7.6 and 7.7.7.

As already observed in the previous pages, the behavior of ice VIII is mainly harmonic and the attribution of the peaks, reported in Fig.7.7.8, is relatively simple and confirms the assignment made by A.F. Goncharov et al.[42] (see also Fig.7.7.4).

The low pressure region is dominated by the high frequency O-H stretching vibrations: they form a triplet which has been assigned to $\nu_1(A_{1g})$, $\nu_3(E_g)$, and $\nu_1(B_{1g})$ modes in order of increasing frequency. These modes soften with pressure.
The $\nu_1(A_{1g})$ mode has the largest pressure shift and can be considered the order parameter of the phase transition. The experiments claim that, with the decrement in frequency of this mode, the intensities of other bands are enhanced sequentially from higher to lower frequency to produce prominent resonances, which appear and disappear as the pressure increases. The most notable is the resonance at 38 GPa

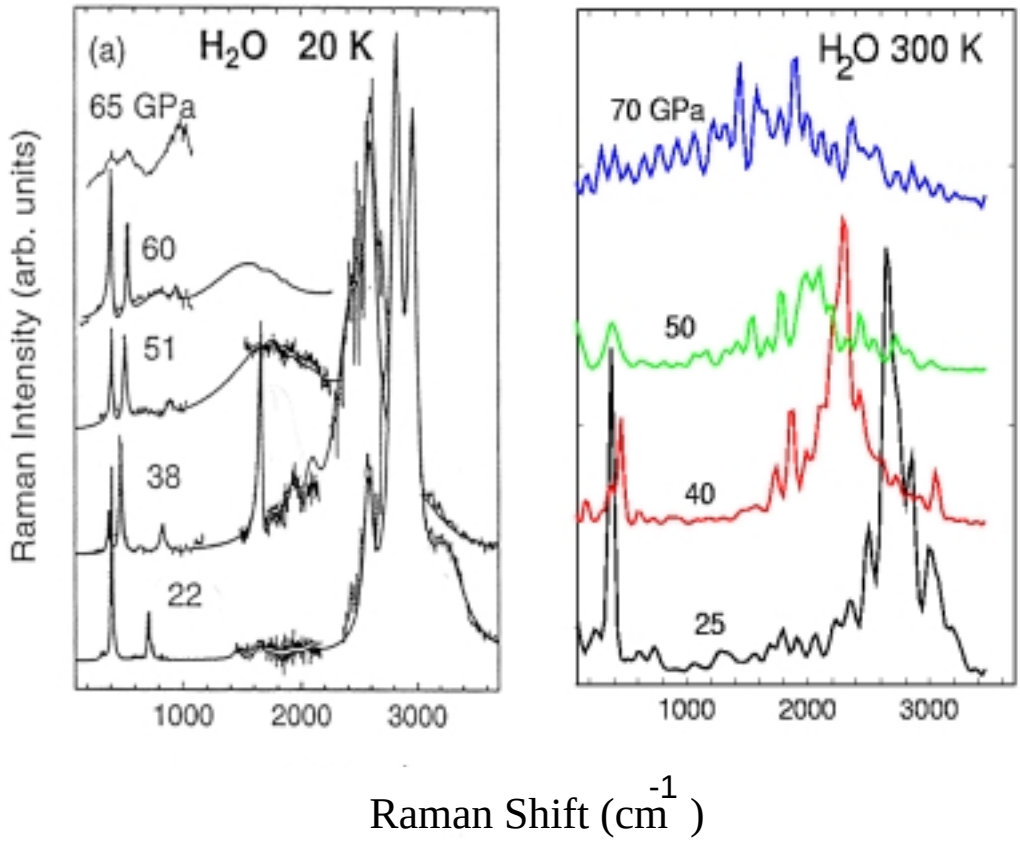

Figure 7.7.6: *Comparison with the experiments. Left panel: experimental data [42]. Right panel: simulated data. At low pressure the spectrum of ice VIII is dominated, from the high-frequency O-H stretching vibrations: they form a triplet (a doublet and a small shoulder), which has been assigned to* $\nu_1(A_{1g})$, $\nu_3(E_g)$, *and* $\nu_1(B_{1g})$ *modes in order of increasing frequency and soften with pressure. The high-frequency* $\nu_1(A_{1g})$ *band has the largest pressure shift. As this mode decreases in frequency, the intensities of the other bands are enhanced sequentially from higher to lower frequency to produce prominent resonances, which appear and disappear as the pressure increases. The most notable is the resonance at 38 GPa in the region (1650* cm^{-1}*) where the results of the experiments are more uncertain because of the presence of the signal of the diamond-anvil cell. In our simulation such a pronounced resonance is not visible; however, some of the smaller structures of that frequency region, present also in the experiments, are evident. In the low frequency range and at low temperature the spectrum is dominated by the sharp translational bands assigned to the* $\nu_{T_z}(A_{1g}) + \nu_{T_{xy}}(E_g)$ *and* $\nu_{T_z}(B_{1g}) + \nu_{T_{xy}}(E_g)$ *excitations of ice VIII at 400 and 500* cm^{-1}*; they exhibit only minor frequency shifts at 45-60 GPa, soften and broaden just above 60 GPa and then increase in frequency with the pressure. At higher temperature, like in our simulation, appears only a broad translational band* $\nu_{T_z}(B_{1g}) + \nu_{T_{xy}}(E_g)$*, as also reported in the experiments [42].*

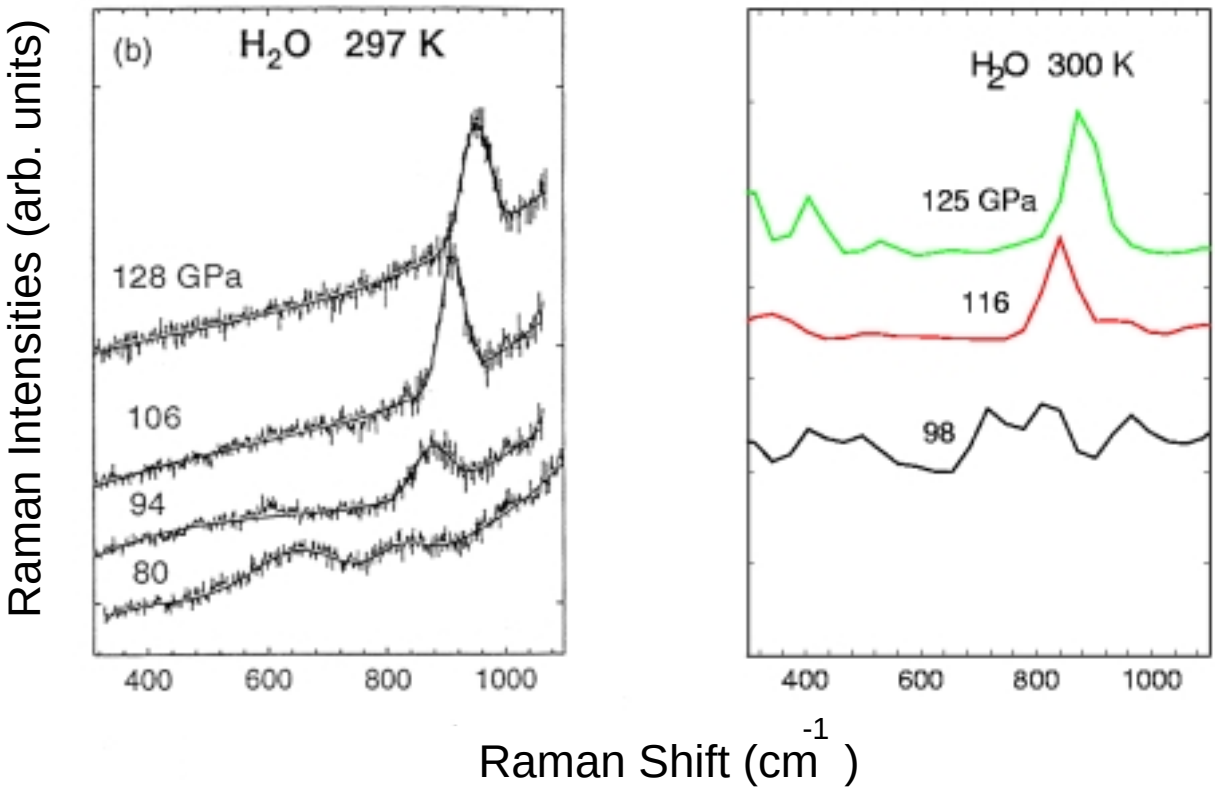

Figure 7.7.7: *Comparison with the experiments. Left panel: experimental data [42]. Right panel: simulated data. With increasing pressure a new band appears, while all the other excitations appear weaken. This new band is identified as the T_{2g} O-O vibration, as expected for the* Cu_2O *structure.*

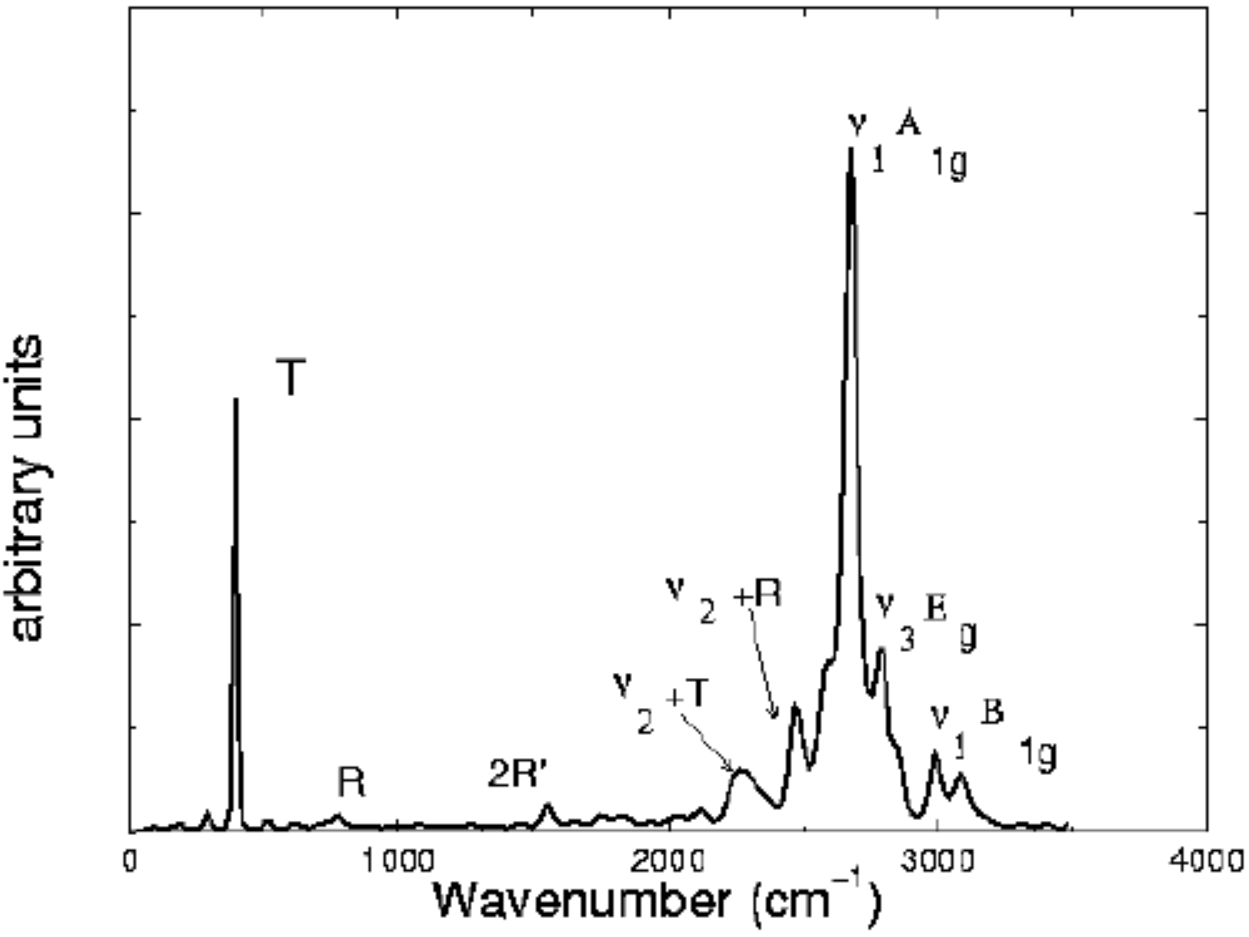

Figure 7.7.8: *Simulated Raman spectrum of ice VIII at 25 GPa and 300 K. At low pressure the spectrum is dominated, like the IR spectrum, by the high-frequency O-H stretching vibrations: they form a triplet, which has been assigned to $\nu_1(A_{1g})$, $\nu_3(E_g)$, and $\nu_1(B_{1g})$ modes in order of increasing frequency and soften with pressure. In the low frequency range the spectrum is dominated by the translational bands assigned to the $\nu_{T_z}(A_{1g})+\nu_{T_{xy}}(E_g)$ and $\nu_{T_z}(B_{1g})+\nu_{T_{xy}}(E_g)$ excitations, which are unresolved at room temperature.*

around 1650 cm^{-1}, which belongs to a frequency region, where the results of the experiments are more uncertain because of the presence of the signal of the diamond-anvil cell. In our simulation such a pronounced resonance is not visible; however, some of the smaller structures of that frequency region, present also in the experiments, are evident, as can be observed in Fig.7.7.6.
These three modes are typical intramolecular vibrations. In fact, the $\nu_1(A_{1g})$ mode, which is double degenerate in the tetragonal distorted system, consists of a linear combination of symmetric stretching of each water molecule, as shown in Fig.7.7.9. The following mode $\nu_3(E_g)$ is a linear combination of antisymmetric stretching of each water molecule, as can be seen in Fig.7.7.10. Finally, the highest frequency mode, $\nu_1(B_{1g})$ is a linear combination of anti-phase symmetric stretching of each water molecule, as shown in Fig.7.7.11.

In order to follow their evolution with increasing pressure, we constructed the velocity-velocity spectrum of the mode, following the procedure described in Sec.6.6.3, and compared it with the Raman spectrum. The result of such an analysis is reported in Figs.7.7.12, 7.7.13 and 7.7.14. As expected, in ice VIII one can observe a clear line, which allows the assignment of the peak to the corresponding mode, while in ice VIII the velocity-velocity spectrum reveals the absence of these normal modes. It is also clear that ice VII is characterized by a very strong disorder. Another measure of the same phenomena, is the observation of the velocity-velocity autocorrelation function in time space, as is reported in Fig.7.7.15 in the case of the soft mode $\nu_1(A_1g)$. In the case of ice VIII, which is mostly harmonic, the autocorrelation function has a oscillatory behavior,in agreement with the strong presence of the mode in the spectrum. In contrast, in the ice VII phase the mode is highly dampened, due to proton transfer processes along the H-bond. Its Raman cross section is very much reduced and consequently the autocorrelation function is strongly dampened. In ice X, as can be observed in Fig.7.3.1, this mode, together with

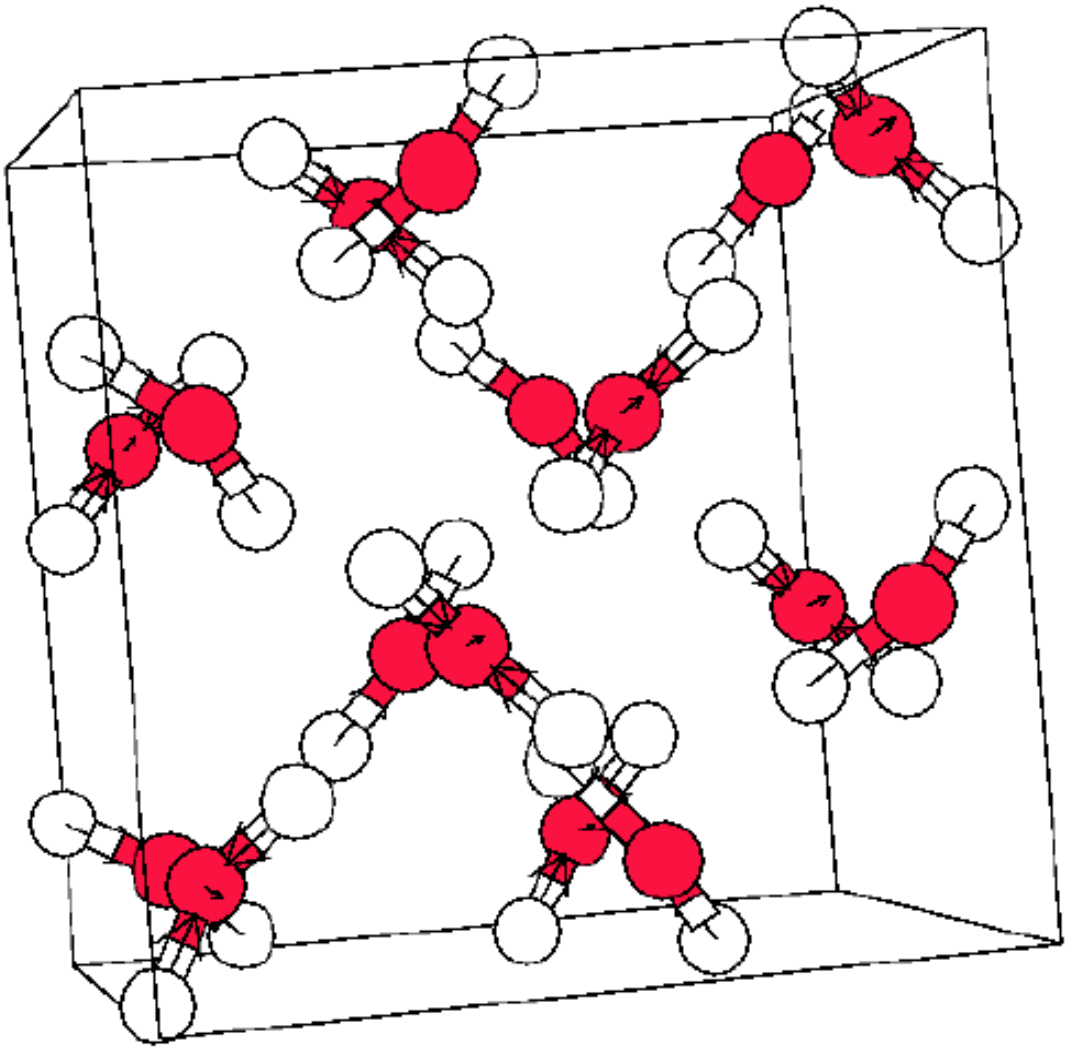

Figure 7.7.9: *Snapshot of the normal mode $\nu_1(A_{1g})$ in ice VIII. This mode is double degenerate in the tetragonal distorted system and consists of a linear combination of in-phase symmetric stretchings of the water molecules.*

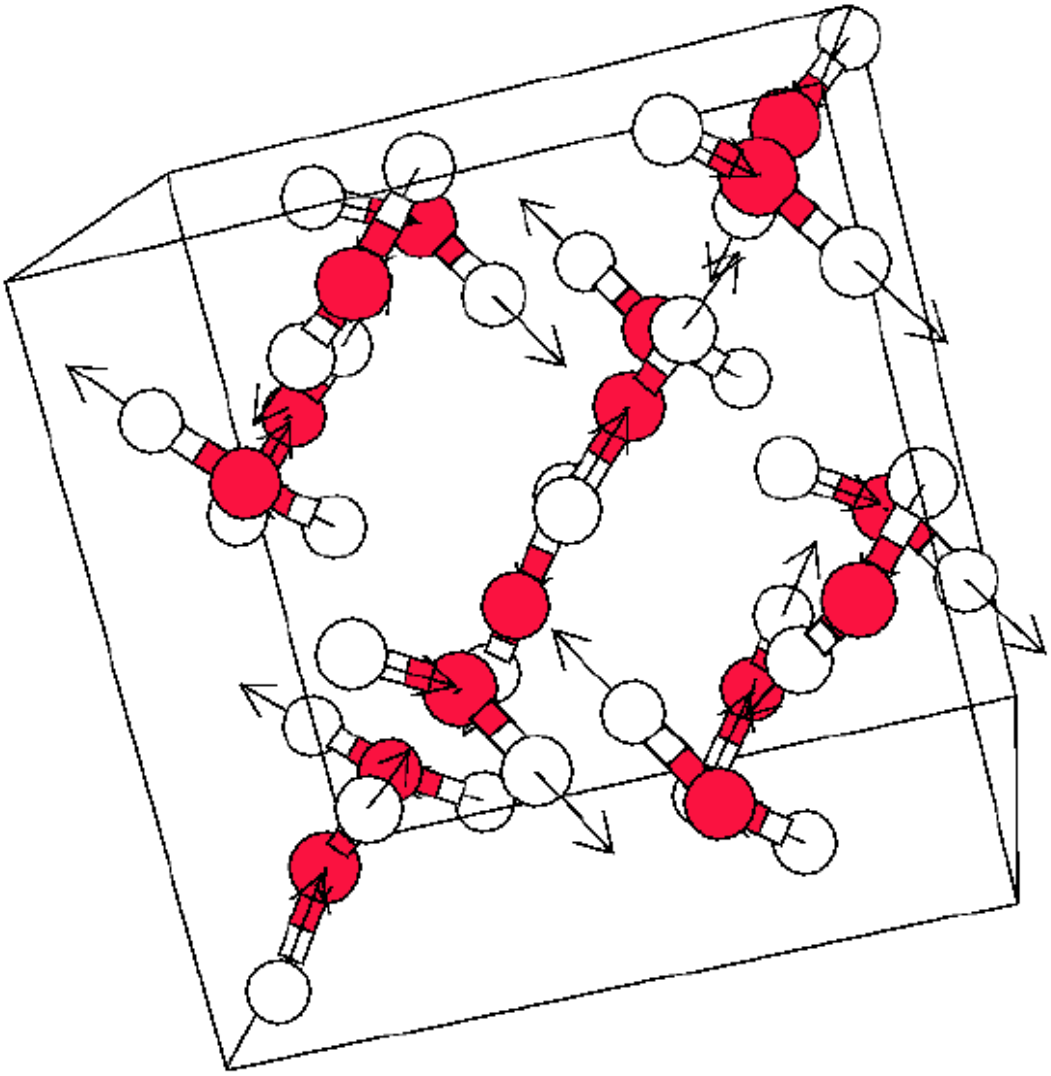

Figure 7.7.10: *Snapshot of the normal mode $\nu_3(E_g)$ in ice VIII. This mode consists of a linear combination of the antisymmetric stretching of each water molecule.*

the other intramolecular modes $\nu_3(E_g)$ and $\nu_1(B_{1g})$, is not observable because it transforms in a mode active only at X point.

In the low frequency range, the spectrum is dominated by the translational bands assigned to the $\nu_{T_z}(A_{1g}) + \nu_{T_{xy}}(E_g)$ and $\nu_{T_z}(B_{1g}) + \nu_{T_{xy}}(E_g)$ excitations, which at the temperature of the simulation are unresolved.

Further increase in pressure produces a major alteration in the spectrum. At 70-100

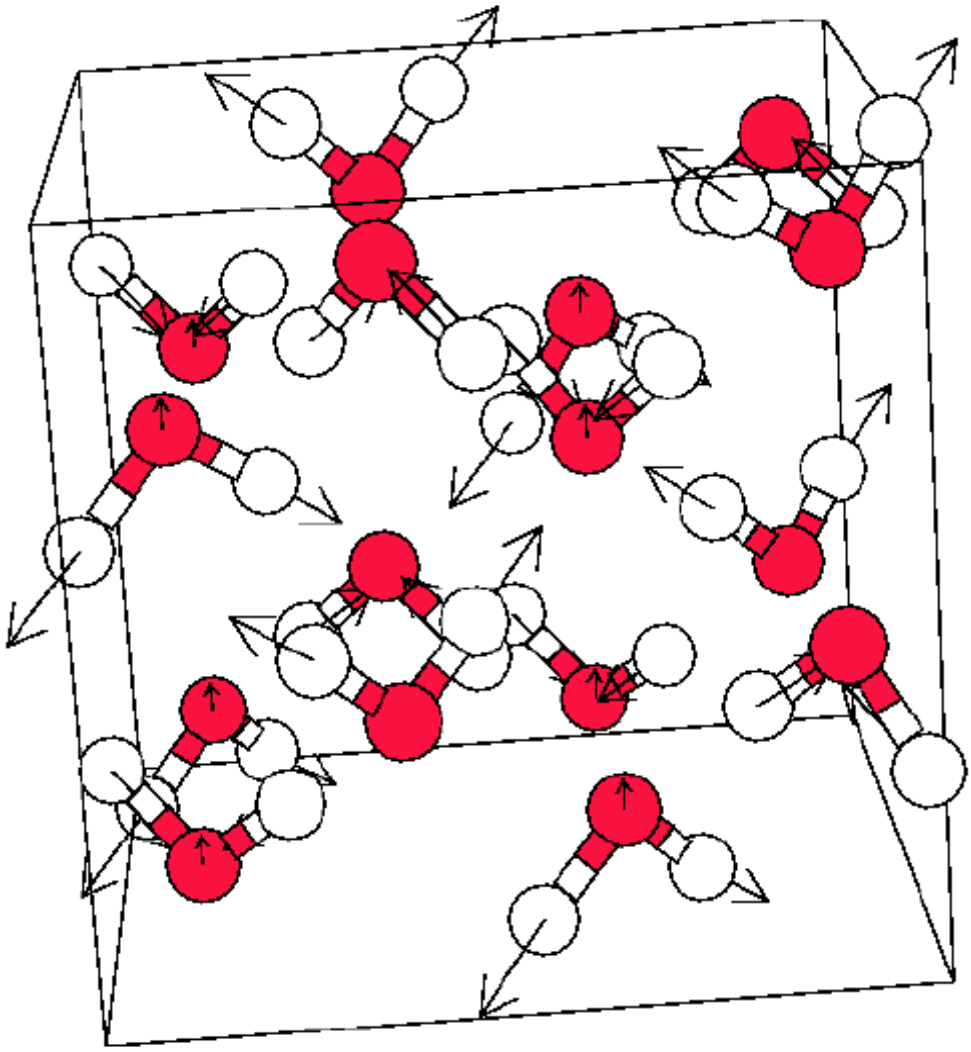

Figure 7.7.11: *Snapshot of the normal mode $\nu_1(B_{1g})$ in ice VIII. This mode is double degenerated in the tetragonal distorted system and consists of a linear combination of anti-phase symmetric stretchings of the water molecules.*

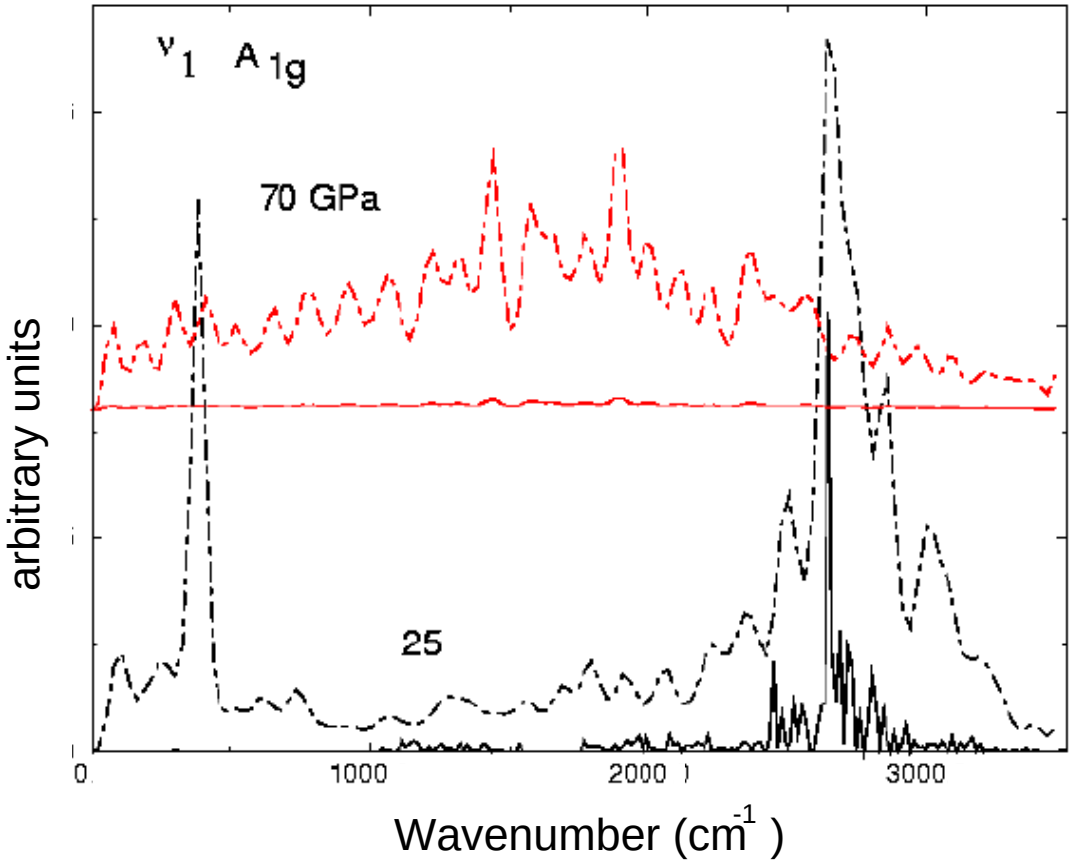

Figure 7.7.12: *Evolution with increasing pressure of the $\nu_1(A_{1g})$ band. Solid line: velocity-velocity spectra; dashed line: Raman spectra.*

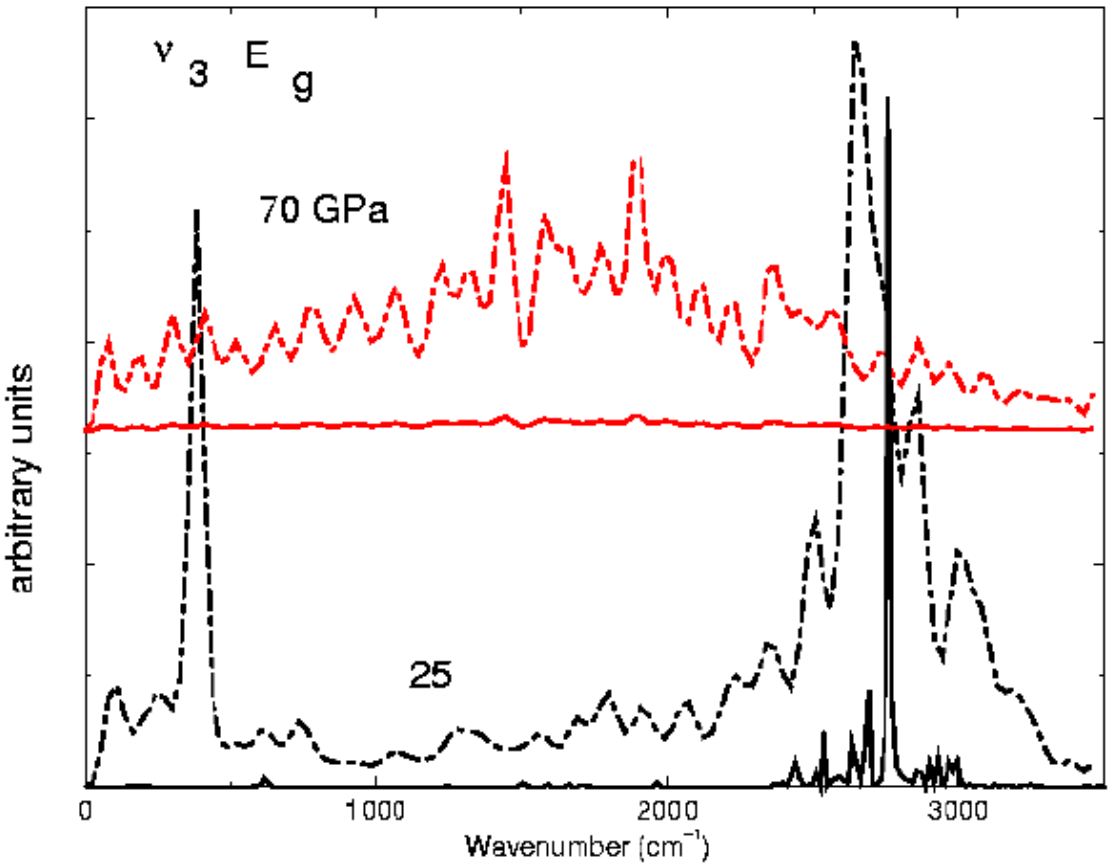

Figure 7.7.13: *Evolution with increasing pressure of the $\nu_3(E_g)$ band. Solid line: velocity-velocity spectra; dashed line: Raman spectra.*

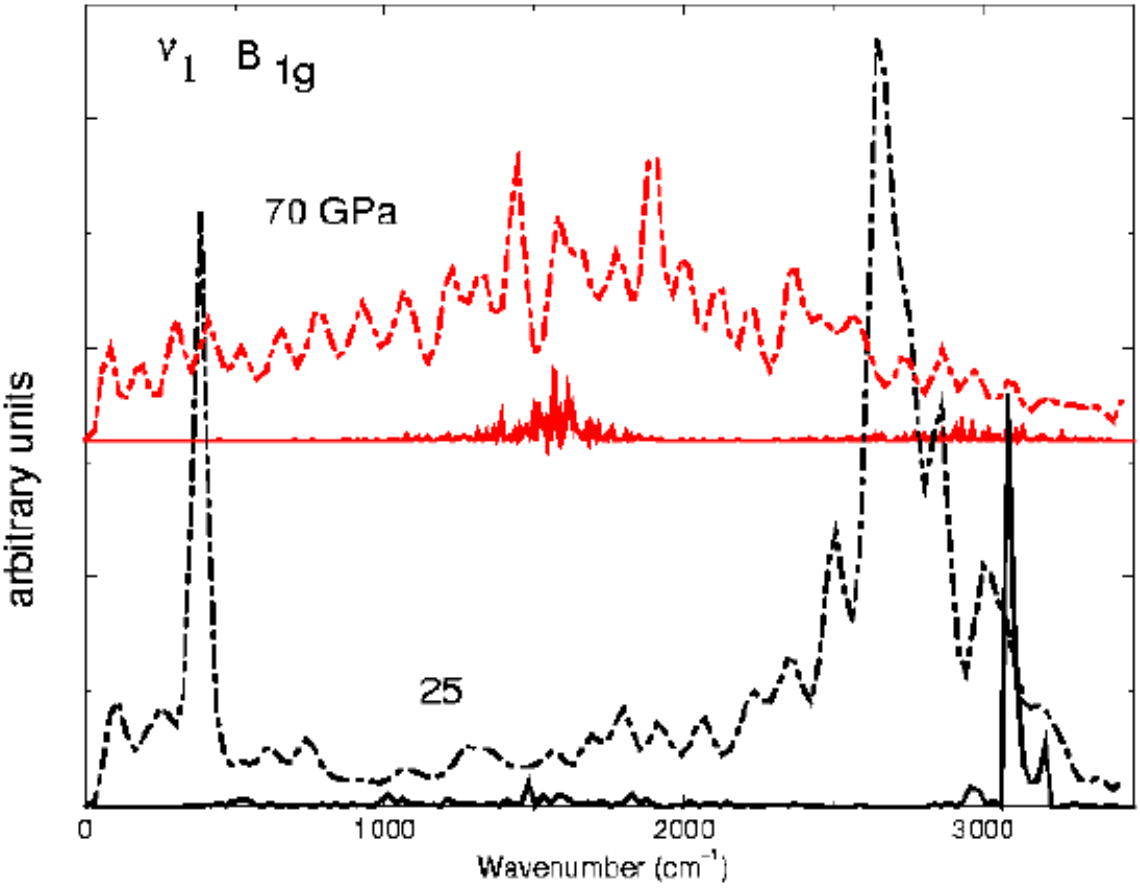

Figure 7.7.14: *Evolution with increasing pressure of the $\nu_1(B_{1g})$ band. Solid line: velocity-velocity spectra; dashed line: Raman spectra.*

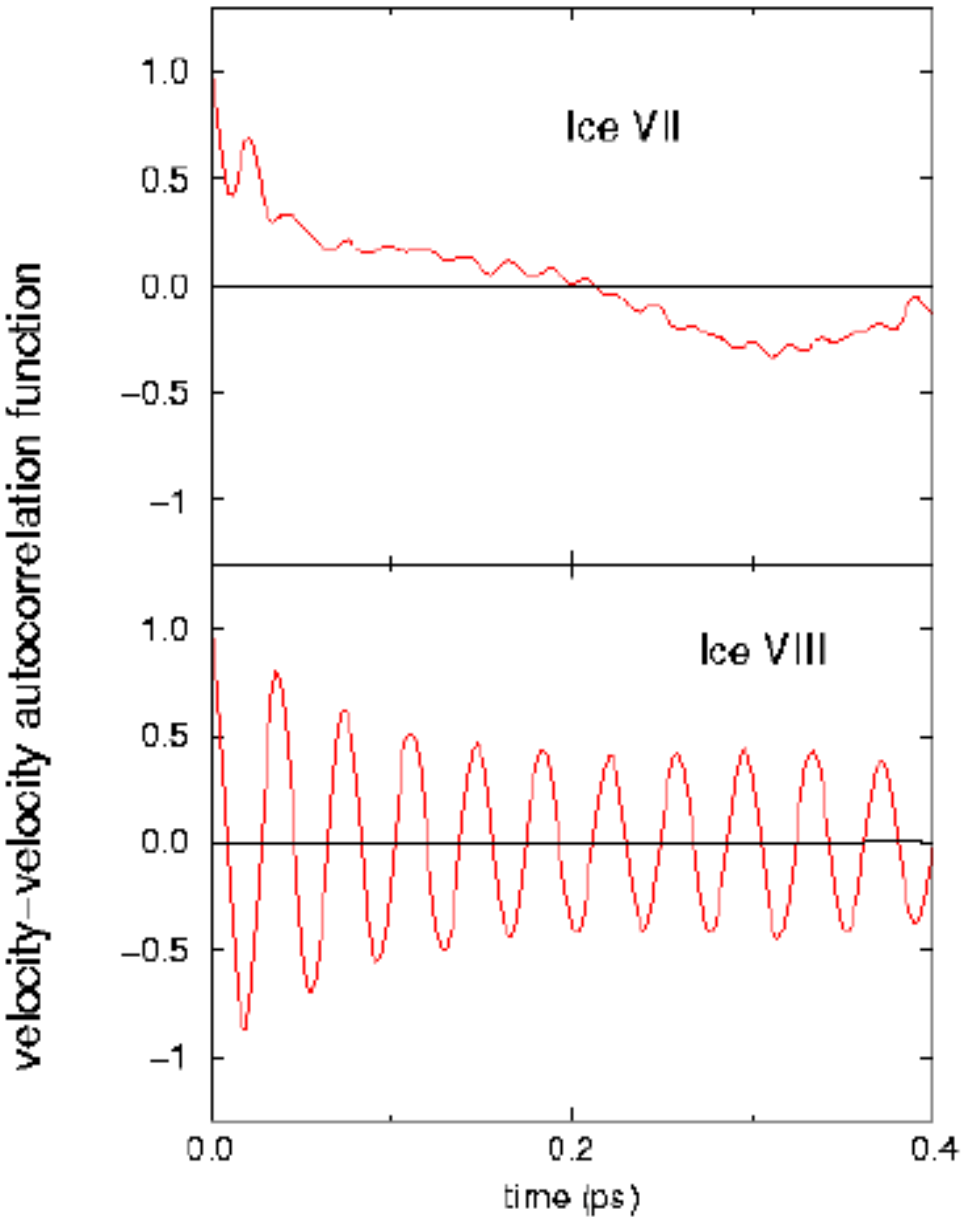

Figure 7.7.15: *Evolution with increasing pressure of the velocity-velocity autocorrelation function in time space for the $\nu_1(A_{1g})$ mode.*

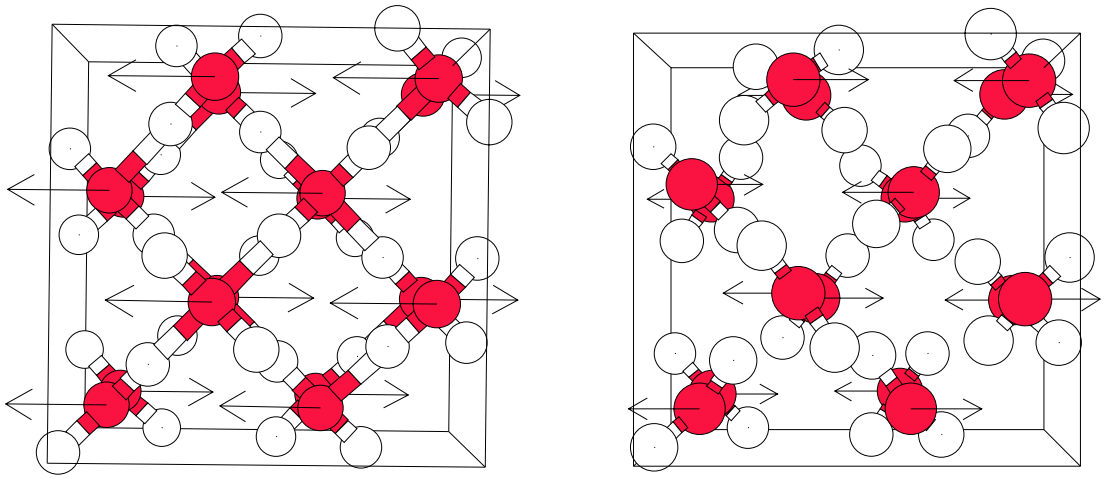

Figure 7.7.16: *Left panel: one of the three modes* $\nu_{\mathrm{T}}(\mathrm{T_{2g}})$ *in ice X. Right panel: one of the modes of the band* $\nu_{T_z}(B_{1g}) + \nu_{T_{xy}}(E_g)$ *in ice VIII.*

GPa the spectra seem indicate a strongly disordered structure. At pressure higher than 100 GPa, finally, a new narrow band (Fig.7.7.5) appears, while all the other excitations appear to weaken. The frequency of this new excitation increases with pressure.

We identified this band as the T_{2g} O-O vibration, as expected for the Cu_2O structure. This normal mode, which is triply degenerate, is an anti-phase vibration of the two oxygen body-centered cubic sublattices, as shown in the right panel of Fig.7.7.16. As we have already discussed in Sec.7.3, the translational band $\nu_{T_z}(B_{1g}) + \nu_{T_{xy}}(E_g)$ of ice VIII, shown in the left panel of Fig.7.7.16, evolves with increasing symmetry into the translational band T_{2g}. All the molecular modes present at lower pressure disappear, as expected from group theory and discussed by Hirsch et al.[33] (see Fig.7.3.1). In order to validate this idea, we performed also in this case the vibrational analysis for two modes.

The result is shown in Fig.7.7.17: at low pressure in ice VIII a translational mode $\nu_{T_z}(B_{1g}) + \nu_{T_{xy}}(E_g)$ of the O-O lattice is clearly present. This mode evolves at high pressure in the T_{2g} band that identifies the cuprite structure, confirming the prediction of Ref.[33]. However, it is important to observe that in ice X the effects of anharmonicities are very important. In fact, in contrast with the case of ice VIII, in ice X the vibrational peak is shifted with respect to the Raman spectrum. This is reflected also in the real space representation, where the velocity-velocity autocorrelation function for this translational modes is slightly damped due to proton disorder, as can be observed in Fig.7.7.18. As a consequence, only a small and shifted signal is observed.

7.7.6 Isotropic and anisotropic part of the Raman spectra

In order to add further information to the experiments, we look in detail to the two contributions to the Raman spectrum, the isotropic and the anisotropic part. As we have seen in Sec.6.2, the two different contributions are responsible for the two different geometric contributions to the total intensity and they are related also to the nature of the modes responsible of the peaks:

$$\mathbf{I}_{VV}(\omega) = \mathbf{I}_{ISO}(\omega) + \frac{4}{3}\mathbf{I}_{VH}(\omega)$$

where

$$\mathbf{I}_{ISO}(\omega) = \frac{N}{2\pi}\int dt\, e^{-i\omega_f t}\langle \alpha(0)\,\alpha(t)\rangle$$

and

$$\mathbf{I}_{VH}(\omega) = \frac{N}{2\pi}\int dt\, e^{-i\omega_f t}\frac{1}{10}\langle \mathrm{Tr}(\beta(0)\cdot\beta(t))\rangle$$

The $\mathbf{I}_{VH}$ Raman spectrum depends on both molecular vibration and rotation, while $\mathbf{I}_{ISO}$ depends only on the vibrational motion.

In Fig.7.7.19 we report the isotropic and the anisotropic spectra for ice VIII and ice

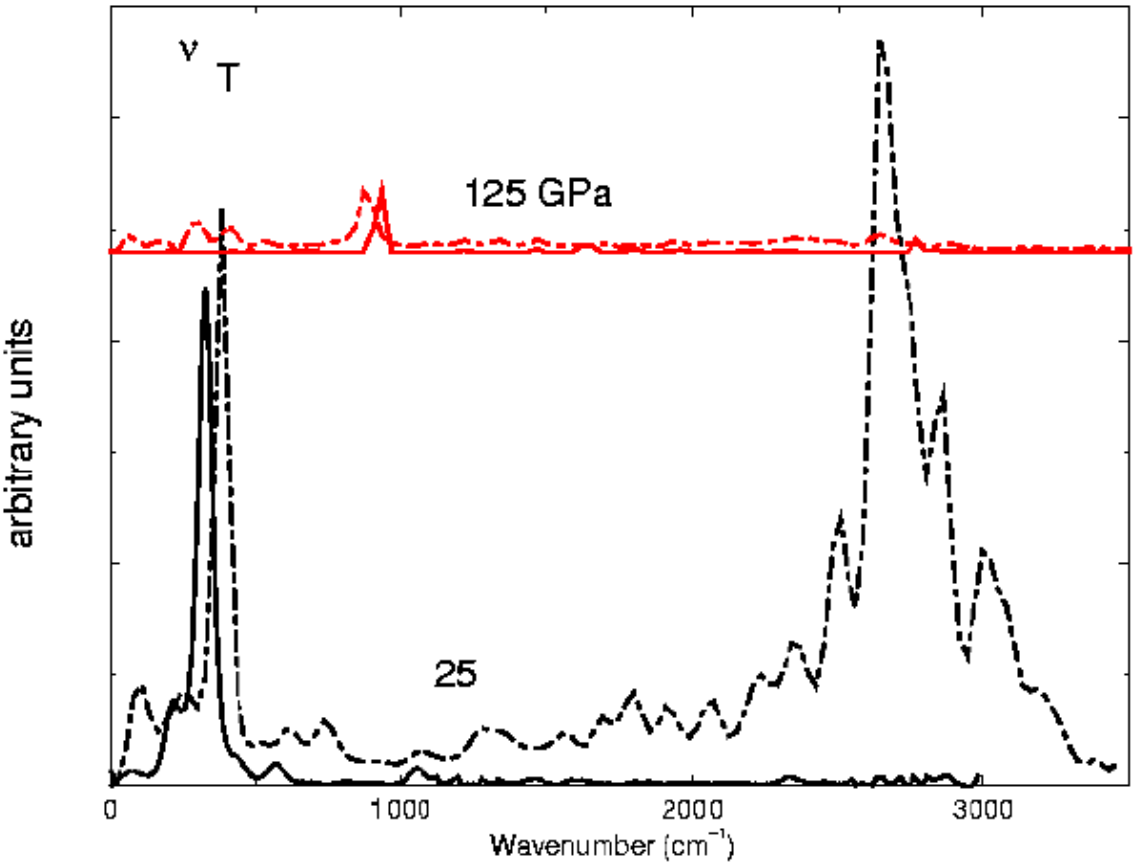

Figure 7.7.17: *Comparison between the Raman spectrum and the velocity-velocity spectrum of the mode ν_T. Solid line: velocity-velocity spectrum; dashed line: Raman spectrum. At low pressure in ice VIII a translational mode of the O-O lattice is clearly present. This mode evolves at high pressure in the T_{2g} band that identifies the cuprite structure. This is predicted by the group theory through the correlation table of the group O_h.*

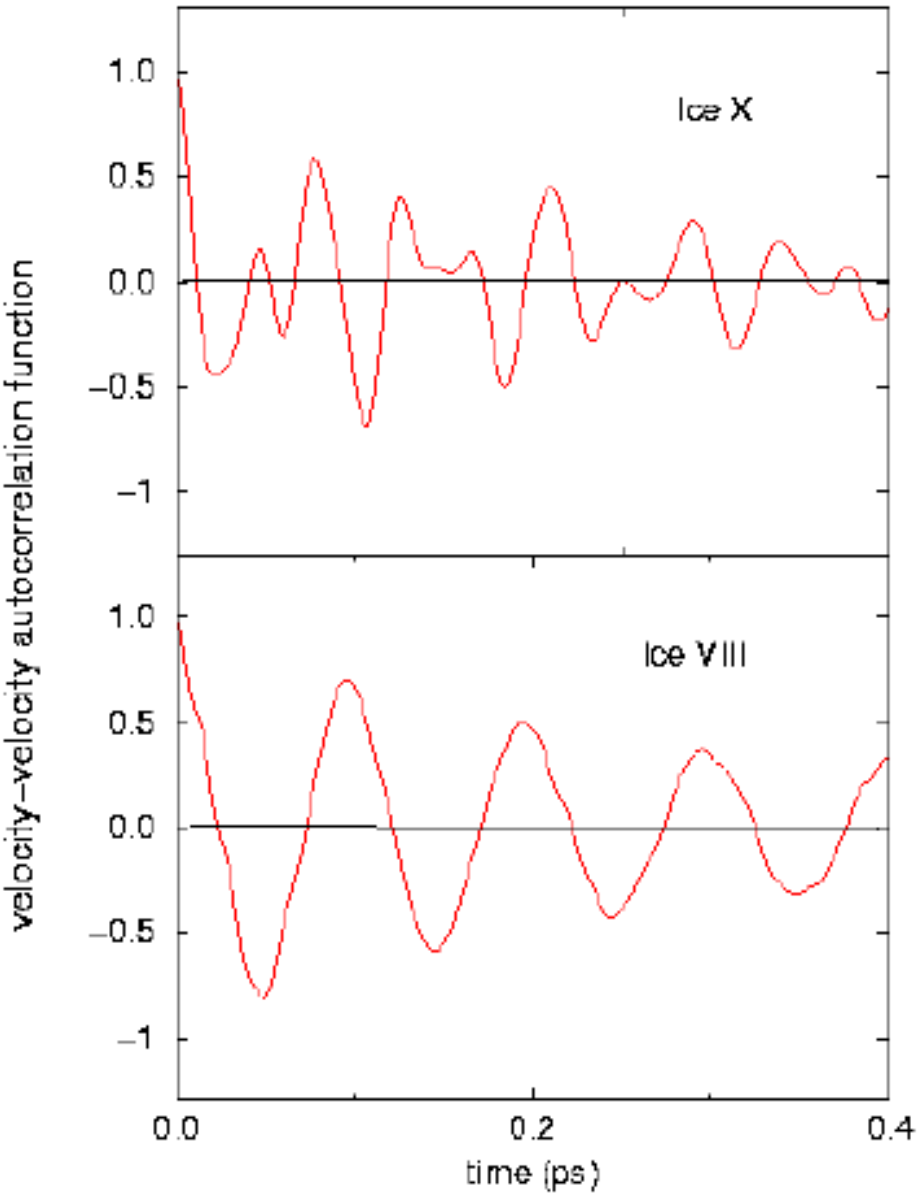

Figure 7.7.18: *Evolution with increasing pressure of the velocity-velocity autocorrelation function in time space for the translational bands in ice VIII and ice X.*

X. In ice VIII the stretching and bending molecular modes of water are given for the most part by the isotropic part of the intensity $\mathbf{I}_{ISO}$, as expected for molecular vibrations. The peaks at low frequencies, which are mostly translational bands, are instead related to the anisotropic part $\mathbf{I}_{VH}$ and their nature does not change through the transition, that implies only the transformation from the less symmetric translational modes of ice VIII to the high symmetric T_{2g} mode predicted for the classical cuprite-type structure of H_2O.

In this way the high pressure Raman spectrum is mostly only composed of the anisotropic part. Progress in experimental techniques at high pressure might allow to resolve $\mathbf{I}_{VV}$ and $\mathbf{I}_{VH}$, thus allowing a precise determination of the nonmolecular phase.

7.8 Conclusion

In conclusion, our *ab initio* simulation of the Raman spectra gives a further foundation to the idea of a nonmolecular structure in the high pressure phase diagram of ice. Furthermore it validates the experimental data, which otherwise can be controversial because of the technical difficulties involved in these measurements. Most probably this high pressure nonmolecular phase of ice is the cuprite structure, called ice X. The certitude about this phase will be obtained only if it will be possible to perform neutron scattering measurements, which are able to indentify the proton positions, which is at present rather challenging at these high pressure. However, all IR and Raman experiments and simulations seem to indicate that this is the case.

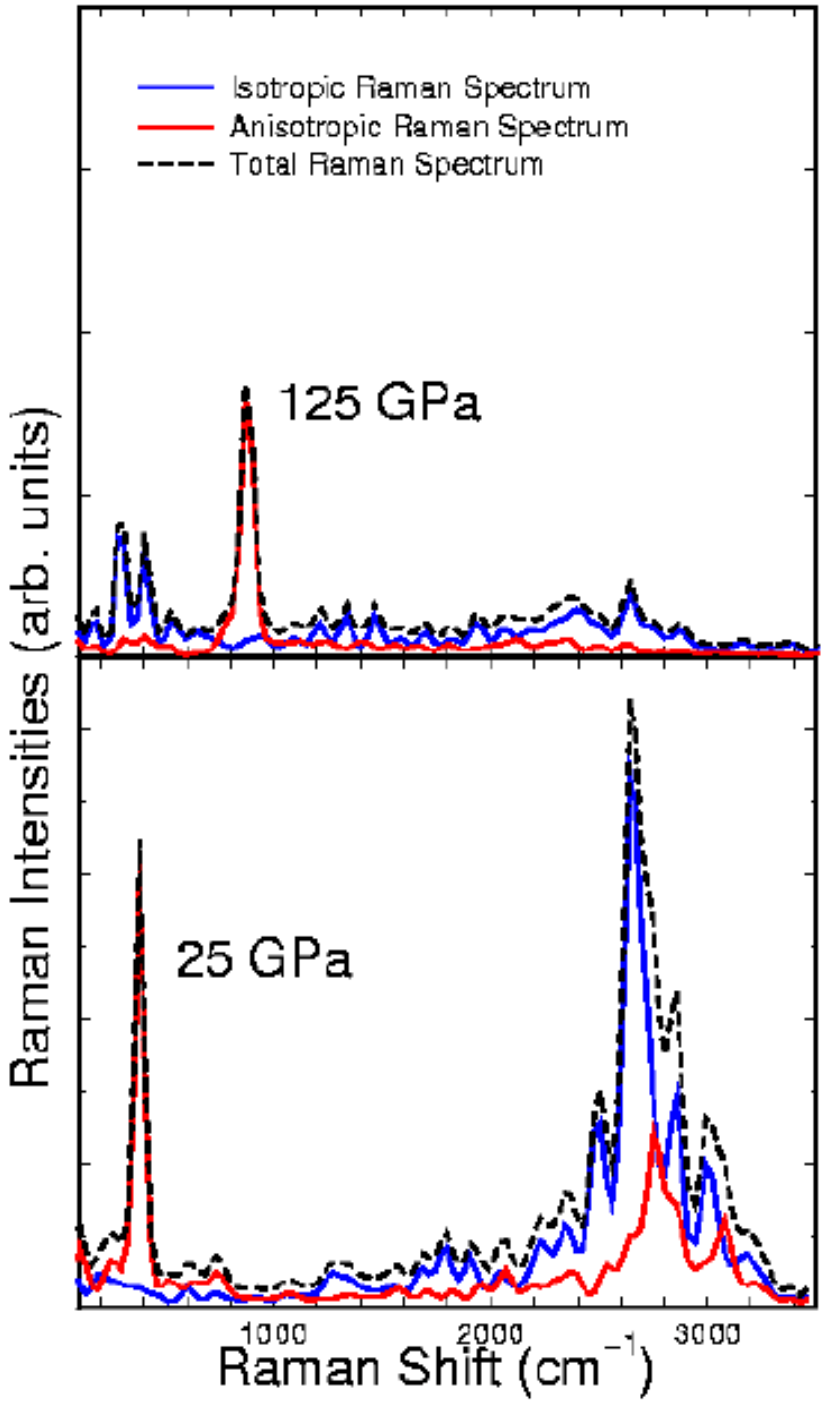

Figure 7.7.19: *Isotropic and anisotropic contribution to the Raman spectra in ice VIII (bottom) and in ice X (top). The anisotropic Raman spectrum depends on both molecular vibration and rotation, while isotropic Raman spectrum depends only on the vibrational motion.*
In ice VIII the stretching and bending molecular modes of water are given for the most part by the isotropic part of the intensity $\mathbf{I}_{ISO}$ *. The peaks at low frequencies are instead related to the anisotropic part* $\mathbf{I}_{VH}$ *and their nature does not change through the transition, that implied only the transformation from the less symmetric T modes to the high symmetric* T_{2g} *mode predicted for the classical cuprite-type structure of* H_2O*.*

Chapter 8

Conclusion

In this thesis we have presented a new method, which allows to calculate *ab initio* Raman spectra of anharmonic and disordered systems. In order to lift the restriction of *ab initio* Raman spectra calculations to harmonic systems, we have combined molecular dynamics with the generalization of variational perturbation theory to non-hamiltonian perturbations [106]. This generalization is not only finalized to the construction of a method to simulate Raman spectra for anharmonic and disordered systems, but is also a derivation of variational density functional perturbation theory more transparent than the previous approach of Gonze [6] in the restricted case of Hamiltonian perturbations. Such a new approach to the variational perturbation theory was tested on different kinds of perturbations (vibrational modes, NMR chemical shifts, etc) and then applied to the specific case of Raman, i.e. the coupling of an electric field with the polarization in a periodic system, described in our approach with a Berry phase using the modern theory of polarization. Finally, we tested our method to calculate Raman spectra of anharmonic and disordered systems on an interesting and discussed phase transition of Ice from phase VIII to phase X. This transition is of relevance in condensed matter, biology and planetary physics. The simulated spectra are in good agreement with the experiments. The

insight gained strengthens the interpretation of the experiments. In combination with the CPMD code, generalized variational perturbation theory will provide a useful and versatile tool to investigate the properties described above as well as other important quantities like chemical hardness, elastic constants, NMR chemical shifts, etc, in disordered and anharmonic systems.

Appendix A

Polarizability: non cubic cells case

As we have seen in Sec.6.4, the polarizability tensor $\alpha_{\mu\nu}$ can be expressed in terms of Berry phase:

$$\alpha_{\mu,\nu} = \frac{2\,|e|}{|\mathbf{G}_\nu|}\mathrm{Im}\left[\sum_{i,j}\left(\left\langle \psi_i^{(1)}\left|e^{i\mathbf{G}_\mu\cdot\mathbf{r}}\right|\psi_j^{(0)}\right\rangle \quad + \left\langle \psi_i^{(0)}\left|e^{i\mathbf{G}_\mu\cdot\mathbf{r}}\right|\psi_j^{(1)}\right\rangle \quad \right)\mathbf{Q}_{j,i}^{(\nu)-1}\right],$$

where the matrix $\mathbf{Q}^{(\mu)}$ is defined as $\mathbf{Q}_{i,j}^{(\mu)} = \left\langle \psi_i\left|e^{i\mathbf{G}_\mu\cdot\mathbf{r}}\right|\psi_j\right\rangle$, and $\mathbf{G}_\mu$ is the smallest vector in a periodically repeated cubic cell in the direction μ.

Now, in the case of non-cubic simulation cell, in principle should be possible to calculate the polarizability tensor in a very easy way, through simple geometry observations. We can, in fact, think to calculate the tensor in the system of coordinates defined by the smallest vector of the reciprocal cell. If we call this new matrix $\tilde{\alpha}$, then the canonical matrix α can be easily calculated by means of a change of system of coordinates. If U is the unitary matrix of the change of coordinates from the distorted system to the canonical one, then:

$$\alpha = U^{-1}\tilde{\alpha}U \tag{A.0.1}$$

However, this expression result to be numerically inaccurate. In order to understand the reason of this instability, we focus now the attention on the case of a single

electron. Then, we note that in this case our expression for the $\langle \mathbf{r} \rangle$ coincide with the first term of its expansion in cumulants. In fact:

$$\begin{aligned} -i\mathbf{G}\cdot\langle\mathbf{r}\rangle &= \log\exp(-i\mathbf{G}\cdot\langle\mathbf{r}\rangle) \\ &= \log\langle\exp(-i\mathbf{G}\cdot\mathbf{r})\rangle - \exp\left(\sum_{i=2}^{\infty}\sum_{\{m\}} u_i(\mathbf{r})\frac{\xi_1^{m_1}\xi_2^{m_2}\xi_3^{m_3}}{m_1!m_2!m_3!}\right) \\ &\approx \log\langle\exp(-i\mathbf{G}\cdot\mathbf{r})\rangle, \end{aligned} \tag{A.0.2}$$

where $\{m\}$ indicates $\sum_{k=1}^{3} m_k = i$, $\xi_i = -iG_i$ and $u(\mathbf{r})$ are the coefficients of the cumulants expansion. Simple algebra shows now that if we are using a cubic cell the term in the sum corrisponding to $i = 2$ is null, for other cell it is not. This means that for a cubic cell our approximated formula is more accurate.

For this reason, any time we want to use a non-cubic cell, is better use directly Eq.(6.4.14), where we take $\mathbf{G}$ to be a linear combination of reciprocal space vector which gives exactly the $\{x, y, z\}$ directions. This procedure is, for the reason exposed above, more accurated than the rotation of the tensor through a change of system of coordinates.

Acknowledgments

I would like to thank Prof. Dr. Parrinello for giving me the opportunity to do research in his group and for many interesting discussions.

I am grateful to Prof. Dr. Muramatzu for his interest in my work and for accepting to be co-referee of the thesis.

A particular thank goes to Daniel Sebastiani: he is not only a good coworker, but also a good friend; he helped me a lot in all these years, in particular at the start of my life in Stuttgart, when I was still unable to speak German.

I would like to thank Prof. Dr. Marco Bernasconi, Dr. Mauro Boero, Dr. Pierluigi Silvestrelli and Prof. Dr. Juerg Hutter for the useful conversations.

I am grateful to Dr. Stefan Goedecker for the help in the optimization of the code and for interesting conversations.

I would like to thank Dr. Peter Haynes, Brendan Gibson, Dr. Steven Kooi, Dr. David Benoit, Dr. Samrat Ghosh, and Mike for the careful reading of the English text; Dr. Ralf Vogelgesgang, Dr. Mathias Krack and Daniel Aktah for the help in the German text. Ralf helped me also in understanding the normal modes of ice.

Moreover, I am grateful to several members and former members of Max-Planck Institut for the quotidian life: Dr. Carla Molteni for being a good friend and help me in several situations, Dr. Michael Haiber for the help in all these years and the nice time in Stuttgart and München, Dr. Mike Harris for the nice time in Stuttgart during the first year of my Ph.D., Dr. Simone Meloni for being my sport training, chemistry teacher and for the good dinners, Dr. Francesco Filippone for the friendship, Dr. Valeria Meregalli for the support in the most difficult moments of life, Dr. Aldo Romero for the lessons of Salsa and Merengue, Dr. Stephan Bäurle for the nice evenings and the friendship, Dr. Samrat Ghosh for nice indian dinners

and exchange of ideas, Dr. Giovanni Costantini for the friendship in these my last months in Stuttgart and for the nice time spent together.
A special thank goes to Dr. Stefan Goedecker for the nice days in Stuttgart, Murnau, Torgon and Grenoble, for teaching me to ski and for the nice walks on the mountains.

I would like also to thank Prof. G. Bachelet for being a good friend and a good advisor and for encouraging me.

Finally, I am grateful to my parents for their encouragements and their support.

Lebenslauf

Anna Putrino, geboren am 27.03.1972 in Monza, Italien

09/1978 -06/1986: Besuch der Grundschule (Scuola elementare Dante Alighieri - Scuola Media Teresa Confalonieri) in Monza (Italien).

09/1986 -06/1991: Besuch des Gymnasiums (Liceo Scientifico XXXI Nomentano) in Rom (Italien).

11/07/1991: Abitur

10/1991: Studium der Physik, Universität "La Sapienza"- Rom (Italien) .

09/1996: Diplomarbeit bei Prof. G.B. Bachelet zum Thema: "Curvilinear Coordinates for full-core atoms".

17/07/1997: Diplom in Physik

08/1997-01/1998: Mitarbeiter bei INFM (Istituto Nazionale di Fisica della Materia) in Rom (Italien).

seit 02/1998: Vorbereitung der Dissertation am Max-Planck Institut für Festköperforschung- Stuttgart bei Prof. M. Parrinello.

[1] M.M. Sushchinskii, *Raman scattering of molecules and crystals* (Keter INC. New York, 1972).

[2] P. Jemmer, M. Wilson, P.A. Madden, and P.W. Fowler, J. Chem. Phys. **111**, 2038 (1999).

[3] R. Car and M. Parrinello, Phys. Rev. Lett. **55**, 2471 (1985); see also for technical details: G. Galli and M. Parrinello, *Proc. NATO ASI- Computer Simulation in Material Science* , edited by M. Meyer and V. Pontikis (Kluwer Acad.,1991); M.E. Tuckerman and M. Parrinello, J. Chem. Phys. **101**, 1302 (1994).

[4] S. Baroni, P. Giannozzi and A. Testa, Phys. Rev. Lett. **58**, 1861 (1987).

[5] R.M. Sternheimer,Phys. Rev. **96**, 951 (1954); R.M. Sternheimer,Phys. Rev. **84**, 244 (1951); R.M. Sternheimer and H.M. Foley, Phys. Rev. **92**, 1460 (1953).

[6] X. Gonze, Phys. Rev. A **52**, 1096 (1995); X. Gonze and J.P. Vigneron, Phys. Rev. B **39**, 13120 (1989).

[7] R. Resta, Ferroelectrics **136**, 51 (1992).

[8] R. Resta, Europhys. Lett. **22**, 133 (1993).

[9] R.D. King-Smith and D. Vanderbilt, Phys. Rev. B **47**, 1651 (1993).

[10] R. Resta, Rev. Mod. Phys. **66**, 899 (1994).

[11] R. Resta, in: *Quantum-Mechanical Ab-initio Calculation of the Properties of Crystalline Materials*, Lecture Notes in Chemistry, Vol **67**, edited by C. Pisani (Springer, Berlin, 1996), p.273.

[12] R.M. Martin and G. Ortíz, Solid State Commun. **102**, 121 (1997).

[13] R. Resta, Europhysics News **28**, 18 (1997).

[14] R. Resta, Phys. Rev. Lett. **80**, 1800 (1998).

[15] E. Yaschenko, L. Fu, L Resca, and R. Resta, Phys. Rev. B **58**, 1222 (1998).

[16] R. Resta, Int. J. Quant. Chem. **75**, 599 (1999)

[17] R. Resta and S. Sorella, Phys. Rev. Lett. **82**, 370 (1999).

[18] R. Resta, *Berry Phase in Electronic Wavefunctions*, Troisième Cycle Lecture Notes (Ecole Polytechnique Fédérale, Lausanne, Switzerland, 1996). Available online (194K) at the URL:
http://ale2ts.ts.infn.it:6163/~resta/publ/notes_trois.ps.gz.

[19] R. Resta, *Proc. of the VII Italian-Swiss Workshop - Advances in Computational meterial science- II*, edited by V. Fiorentini and F. Meloni, S. Margherita di Pula, (Cagliari) 19-23 September 1997.

[20] J.O. Hirschfelder, W. Byers Brown and S.T. Epstein, *Advances in Quantum Chemistry* Academic New York, Vol.1 (1964).

[21] L.D. Landau and E.M. Lifshitz, *Electrodynamics of Continuous Media* (Pergamon Press, Oxford, 1984).

[22] C. Kittel, *Introduction to Solid State Physics*, 7th. edition (Wiley, New York, 1996).

[23] N.W. Ashcroft and N.D. Mermin, *Solid State Physics* (Saunders, Philadelphia, 1976).

[24] M.V. Berry, Proc. Roy. Soc. Lond. A **392**, 45 (1984); *Geometric Phases in Physics*, Edited by A. Shapere and F. Wilczek (World Scientific, Singapore 1989).

[25] N. Marzari and D. Vanderbilt, Phys. Rev. B **56**, 12847 (1997).

[26] W. Kutzelnigg, Isr. J. Chem. **19**, 193 (1980).

[27] P.V. Hobbs, *Ice Physics* (Clarendon, Oxford, 1974); W.B. Hubbard, *Planetary Interiors* (Van Nostrand Reinhold, New York, 1984); C. Cavazzoni, G.L. Chiarotti, S. Scandolo, E. Tosatti, M. Bernasconi and M. Parrinello, Science **283**, 44 (1999).

[28] F. Alber and P. Carloni, Protein Science, (2000), in press; S. Piana, D. Sebastiani, P. Carloni, and M. Parrinello, submitted to JACS.

[29] J.M. Besson, M. Kobayashi, T. Nakai, S. Endo and Ph. Pruzan, Phys. Rev. B **55**, 11191 (1997).

[30] L.O. Ojamäe, K. Hermansson, R. Dovesi, C. Roetti and V.R. Saunders, J. Chem. Phys. **100**, 2128 (1994).

[31] W.F. Kuhs, J.L. Finney, C. Vettier and D.V. Bliss, J.Chem. Phys. **81**, 3612 (1984).

[32] Ph. Pruzan, J.C. Chevin and B. Canny, J.Chem. Phys. **99**, 9842 (1993).

[33] W.B. Holzapfel, J. Chem. Phys. **56**, 712 (1972); K.R. Hirsch and W.B. Holzapfel, Phys. Lett. A **101**, 142, (1984); K.R. Hirsch and W.B. Holzapfel, J. Chem. Phys. **84**, 2771 (1986).

[34] A. Polian and M. Grimsditch, Phys. Rev. Lett. **52**, 1312 (1984).

[35] Ph. Pruzan, J. Mol. Struct. **322**, 279 (1994).

[36] F.H. Stillinger and K.S. Schweitzer, J. Chem. Phys. **87**, 4281 (1983); F.H. Stillinger and K.S. Schweitzer, J. Chem. Phys. **80**, 1230 (1984).

[37] Ph. Pruzan,E. Wolanin, M. Gauthier, J. C. Chervin, and B. Canny; D. Häusermann and M. Hanfland, J. Phys. Chem. B **101**, 6230 (1997).

[38] R.J. Hemley et al., Nature (London) **330**, 737 (1988).

[39] R.J. Nelmes et al., Proceedings of the AIRAPT-16 Conference, Kyoto, 1997; R.J. Nelmes et al., Phys. Rev. Lett. **71**, 1192 (1993); J.M. Besson et al., Phys. Rev. B **49**, 12540 (1994).

[40] A.F. Goncharov, V.V. Struzhkin, M.S. Somayazulu, R.J. Hemley and H.K. Mao, Science **273**, 218 (1996).

[41] V.V. Struzhkin , A.F. Goncharov, R.J. Hemley and, H.K. Mao, Phys. Rev. Lett **78** , 4446 (1997).

[42] A.F. Goncharov, V.V. Struzhkin, H. Mao and R.J. Hemley, Phys. Rev. Lett. **83**, 1998 (1999).

[43] M.Bernasconi, P.L. Silvestrelli and M.Parrinello, Phys. Rev. Lett. **81**, 1235 (1998).

[44] M.Benoit, D. Marx and M. Parrinello, Nature (London) **392**, 258 (1998).

[45] Born and Huang, *Dynamical Theory of Crystal Lattices*, Oxford Press, London 1954

[46] C.Filippi, C.J. Umrigar, M. Taut, J.Chem.Phys. **100**, 1290 (1994)

[47] W.H. Press, S.A. Teukoldky, W.T. Vetterling e B.P. Flannery *Numerical Recipes* Second edition, Cambridge University Press (1992)

[48] K. E. Schmidt and M. H. Kalos, *Monte Carlo Methods in Statistical Physics II*, ed. K. Binder, Springer (1984); J. B. Anderson, *Understanding Chemical Reactivity*, S. R. Langhoff, Ed. Kluwer (1995).

[49] C. Filippi and C.J. Umrigar, Phys. Rev. B **61**, 16291 (2000).

[50] D. Ceperley and M. H. Kalos, *Monte-Carlo methods in Statistical Physics* (K. Binder, Ed) Springer, New York 1979

[51] B.L. Hammond, W.A. Lester,Jr. e P.J. Reynolds *Monte Carlo Methods in Ab Initio Quantum Chemestry*, World Scientific

[52] M. H. Kalos, D. Levesque and L. Verlet, Phys. Rev. A **9**, 2178 (1974)

[53] D. M. Ceperley and B. Alder, Phys. Rev. Lett. **45**,566 (1980)

[54] G. Suigiyama and S. E. Koonin, Ann. of Phys. **168**, 1 (1986)

[55] I. Shavitt *Modern Theoretical Chemistry*, edited by H. F. Schaefer, Plenum Press, New York 1977

[56] A. C. Wahl and G. Das *Modern Theoretical Chemistry*, edited by H. F. Schaefer, Plenum Press, New York 1977

[57] H. J. Werner *Ab Initio Methods in Quantum Chemistry*, (K.P. Lawley, ed) John Wiley, Chichester 1987.

[58] J. Czek, J. Chem. Phys. **45**, 4256 (1966); J. Czek, Adv. Chem. Phys. **14**, 35 (1969); J. Czek and J. Paldus, Int. J. Quantum Chem. **5**, 359 (1971).

[59] P. Hohenberg e W. Kohn, Phys. Rev. **136**, B864 (1964).

[60] W. Kohn e L. J. Sham, Phys. Rev. **140**, A1133 (1965).

[61] J. Perdew e A. Zunger, Phys. Rev. B **23**, 5048 (1981).

[62] R. O. Jones and O. Gunnarson, Rev. Mod. Phys. **61**, 689 (1989).

[63] M. Levy and J. P. Perdew, J. Chem. Phys **84**, 4519 (1986).

[64] C. Lee, D. Vanderbilt, K. Laasonen, R. Car and M. Parrinello, Phys. Rev. B **47**, 4863 (1993).

[65] A.D. Becke, Phys. Rev. A **38**, 3098 (1988).

[66] C. Lee, W. Yang, and R.G. Parr, Phys. Rev. B **37**, 785 (1988).

[67] Sprik, J. Hutter and M. Parrinello, J. Chem. Phys. **105**, 1142 (1996).

[68] J. C. Phillips e L. Kleinman, Phys. Rev. **116**, 5048 (1959).

[69] D. R. Hamann, M. Schlüter, C. Chiang, Phys. Rev. Lett. **43**, 1494 (1979).

[70] G.B. Bachelet, D.R. Hamann and M. Schluter Phys. Rev. B **26**,4199 (1982).

[71] G. B. Bachelet e M. Schlüter, Phys. Rev. B **25**, 2103 (1982)

[72] L. Kleinman and D.M. Bylander, Phys. Rev. Lett. **48**, 1425 (1982).

[73] D. Vanderbilt,Phys. Rev. B **41**, 7892 (1990).

[74] N. Trouiller and J.L. Martins, Phys. Rev. B **43**, 1993 (1991).

[75] S. Goedecker, M. Teter, and J. Hutter Phys. Rev. B **54**, 1703 (1996).

[76] *Molecular Dynamics Simulation of Statistical Mechanical Systems*, edited by G. Ciccotti and W. Hoover (Plenum Press, New York, 1986).

[77] M.P. Allen and D.J. Tildesley, *Computer Simulation of Liquids*, Oxford Science Publications (1987).

[78] L. Verlet, Phys. Rev. B **165**, 201 (1967).

[79] W.C. Swope, H.C. Andersen, P.H. Berens, and K.R. Wilson, J. Chem. Phys. **76**, 637 (1982).

[80] G.J. Martyna, M.E. Tuckerman, and M.L. Klein, J. Chem. Phys. **97**, 2635 (1992).

[81] A. Selloni, P. Carnevali, R. Car, and M. Parrinello, Phys. Rev. Lett. **59**, 823 (1987).

[82] E.S. Fois, A. Selloni, M. Parrinello, and R. Car, J. Phys. Chem. **92**, 3268 (1988); F. Ancilotto and F. Toigo, Phys. Rev. B **45**, 4015 (1992).

[83] D.J. Thouless, Phys. Rev. B **27**, 6803 (1983); Q. Niu and D.J. Thouless, J. Phys A **17**, 2453 (1984).

[84] J. Zak, Phys. Rev. Lett. **85**, 1138 (2000).

[85] A. Debernardi, M. Bernasconi, M Cardona, and M. Parrinello, Appl. Phys. Lett. **71**, 2692 (1997); P.L. Sivestrelli, M. Bernasconi and M. Parrinello, Chem. Phys. Lett. **277**, 478 (1997); A. Pasquarello and R. Car, Phys. Rev. Lett. **79**, 1766 (1997).

[86] N.C. Handy, D.J. Tozer, G.J. Laming, C.W. Murray and R.D. Amos, Isr. J. Chem. **33**, 331 (1993).

[87] C. Møller and M.S. Plesset, Phys. Rev. **46**, 618 (1934).

[88] J.A. Pople, J.S. Binkley and P. Seegen, Int. J. Quant. Chem. **XIV**, 545 (1978).

[89] P. Hohenberg and W. Kohn, Phys. Rev. B **136**, 864 (1964); W. Kohn and L.J. Sham, Phys. Rev. **140**, A1133 (1965).

[90] G. Galli and M. Parrinello, Phys. Rev. Lett. **69**, 3547 (1992).

[91] S. Goedecker, Rev. Mod. Phys. **71**, 1085 (1999); R.G. Parr and W. Yang, *Density-Functional Theory of Atoms and Molecules*, Oxford Science Publications (1989).

[92] The code CPMD, version 3.3, developped by J. Hutter, P. Ballone, M. Bernasconi, P. Focher, E. Fois, S. Goedecker, M. Parrinello and M. Turckerman, at MPI für Festköperforschung and IBM Zurich Research Laboratory, 1990-1996.

[93] Gaussian 94, Revision B.2, M. J. Frisch, G. W. Trucks, H. B. Schlegel, P. M. W. Gill, B. G. Johnson, M. A. Robb, J. R. Cheeseman, T. Keith, G. A. Petersson, J. A. Montgomery, K. Raghavachari, M. A. Al-Laham, V. G. Zakrzewski, J. V. Ortiz, J. B. Foresman, C. Y. Peng, P. Y. Ayala, W. Chen, M. W. Wong, J. L. Andres, E. S. Replogle, R. Gomperts, R. L. Martin, D. J. Fox, J. S. Binkley, D. J. Defrees, J. Baker, J. P. Stewart, M. Head-Gordon, C. Gonzalez, and J. A. Pople, Gaussian, Inc., Pittsburgh PA, 1995.

[94] B.G. Johnson, P.M.W. Gill and J.A. Pople, J. Chem. Phys. **98**, 5612 (1993).

[95] Sverdlov, Korner and Krainov *Vibrational Spectra of Poliatomic Molecules*, Wiley (1974)

[96] Herzberg *Molecular Spectra and Molecular Structure II. Infrared and Raman Spectra of Poliatomic Molecules* Van Nostrand (1945).

[97] D. Porezag and M.R. Pederson, Phys. Rev. B **54**, 7830 (1996).

[98] S.Baroni and R.Resta Phys. Rev. B **33**, 5969 (1986).

[99] A. Dal Corso, S. Baroni and R. Resta, Phys. Rev. B **49**, 5323 (1994).

[100] K. Aoki *et al.*, Phys. Rev. Lett. **76**, 784 (1996); Phys. Rev. **B 54**, 15673 (1996).

[101] M. Benoit, D. Marx and, M. Parrinello, Solid State Ionics **125**, 23 (1999).

[102] P.A. Frey, S.A. Whitt, and J.B. Tobin, Science **264**, 1927 (1994).

[103] B. Guillot, J. Chem. Phys. **95**, 1543 (1991).

[104] R.J. Hemley, P.M. Bell and, H.K. Mao, Science **237**, 605 (1987).

[105] P.T.T. Wong and E. Whalley, J.Chem. Phys. **64**, 2359 (1976).

[106] A. Putrino, D. Sebastiani, and M. Parrinello, J.Chem. Phys. **113**, 7102 (2000).

[107] R.S. Katiyar, J.F. Ryan, and J.F. Scott, Phys. Rev. B **4**, 2635 (1971).

[108] B.J. Berne and R. Pecora, *Dynamic Light Scattering* (John Wiley & Sons, INC. 1976).

[109] Ph. Pruzan, J.C. Chevin and B. Canny, J.Chem. Phys. **97**, 718 (1992).

[110] J. Borysow, M. Moraldi and L. Frommhold, Mol. Phys. **56**, 913 (1985).

[111] P.L. Silvestrelli, M. Bernasconi and M. Parrinello, Chem. Phys. Lett. **277**, 478 (1997)

[112] F.A. Cotton, *Chemical Applications of Group Theory* (John Wiley & Sons, INC., third edition 1990).